Department of Physics and Astronomy

University of Heidelberg

Diploma thesis

in Physics

submitted by

Andreas Hillert

born in *Breisach am Rhein, Germany*

July 2010

Modeling the Galactic diffuse gamma-ray emission

MAX-PLANCK-INSTITUT
FÜR KERNPHYSIK

This diploma thesis has been carried out by

Andreas Hillert

at the

Max Planck Institute for Nuclear Physics

under the supervision of

Prof. Werner Hofmann

Abstract

The diffuse gamma-ray emission in our Galaxy is produced by highly energetic electrons interacting mainly with radiation fields through inverse Compton scattering or in interactions with interstellar matter through Bremsstrahlung. Furthermore, protons also interact with the interstellar matter and produce gamma-rays through the production of pion particles and their subsequent decay. The energy range of gamma-ray emission covers the domain from a few MeV (1 MeV = 10^6 eV) up to energies > 100 TeV (1 TeV = 10^{12} eV).

In this work a model to predict the diffuse gamma-ray emission is presented. The general idea of this model is to simulate a population of galactic sources, which accelerate protons and electrons, distributed according to the populations of supernova remnants and pulsars at radio wavelengths. Through the previously mentioned interaction processes, the diffuse gamma-ray emission spectrum can be predicted for different regions of the Galaxy. The goal of this thesis is to produce the spectrum of diffuse gamma-ray emission for the two different regions of the Galaxy at l=344° longitude, b=0° latitude and at l=344° longitude, b=4° latitude.

Kurzfassung

Die diffuse Gammastrahlung in unserer Galaxie wird hauptsächlich verursacht durch Wechselwirkung von hochenergetischen Elektronen mit Strahlungsfeldern über inverse Compton-Streuung, sowie durch Bremsstrahlung bei der Wechselwirkung mit der interstellaren Materie. Weiterhin wechselwirken Protonen mit der interstellaren Materie und erzeugen Gamma-Strahlen mittels Produktion von Pionen über deren darauffolgenden Zerfall. Der Energiebereich der Gammastrahlung umfasst den Bereich von einigen MeV (1 MeV = 10^6 eV) bis zu Energien > 100 TeV (1 TeV = 10^{12} eV).

In dieser Arbeit wird ein Modell zur Vorhersage von diffuser Gammastrahlung präsentiert. Die generelle Idee dieses Modells ist die Simulation von Populationen von Quellen, welche Protonen und Elektronen beschleunigen, die entsprechend der Verteilung von Supernova-Überresten und Pulsaren im Radiobereich verteilt sind. Durch die vorgenannten Wechselwirkungsmechanismen kann das Spektrum der diffusen Gammastrahlung für verschiedene Bereiche in der Galaxie vorhergesagt werden. Das Ziel dieser Arbeit ist die Anfertigung eines Spektrum der diffusen Gammastrahlung für zwei verschiedene Regionen in der Galaxie bei l=344° galaktische Länge und b=0° galaktische Breite, sowie bei l=344° galaktische Länge und b=4° galaktische Breite.

Contents

Chapter 1

Introduction

While looking up on a clear night we can see sparkling stars and planets amidst a black sky. If we were able to see the same sky not in optical but in γ-ray wavelengths we could still see some bright points but the overall sky would not be dark anymore. Instead, it would glow faintly. This is the so called diffuse high-energy γ-ray background. By looking at different energies which correspond to different wavelengths we can find out what causes this "background glow". The energy range of this γ-ray emission covers the domain from a few MeV (10^6 eV) up to energies > 100 TeV (1 TeV $= 10^{12}$ eV).

This diffuse γ-ray backround consists of the truly diffuse Galactic emission from the Interstellar Medium, which is the topic of this thesis, the extragalactic background as well as the contribution from unresolved and faint Galactic point sources. This diffuse background or "background glow" of the γ-ray sky at GeV energies is shown in Figure 1.1. The bright yellow and red band extending through the center of the image, which corresponds to the Galactic plane, is due to cosmic rays interacting with the interstellar gas. This gas (mainly atomic and molecular hydrogen) is concentrated along the plane.
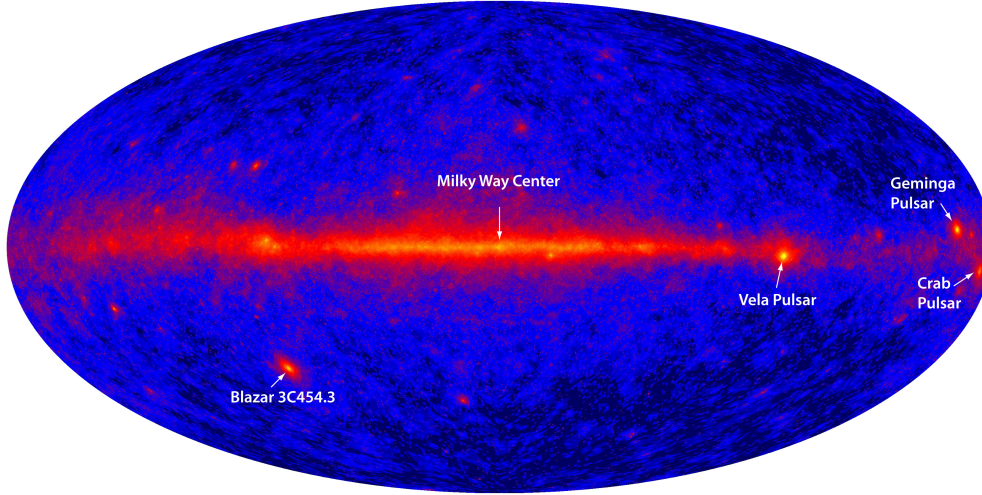
1. INTRODUCTION

Figure 1.1: All-sky map in γ-ray emission from FERMI (GLAST) taken from `http://www.nasa.gov/mission_pages/GLAST/news/glast_findings_media.html`. It shows bright emission in the Galactic plane (center), bright pulsars and super-massive black holes

The Galactic diffuse γ-ray emission is produced in energetic collisions of nucleons with gas through the production of neutral pions and their subsequent decay. Additionally, electrons produce γ-rays via Inverse Compton scattering on radiation fields and by bremsstrahlung in electrical fields of atoms/molecules. Since these processes are dominant in different parts of the γ-ray spectrum, this emission can provide information about the large scale spectra of the nucleonic and leptonic components of cosmic rays. The cosmic rays are deflected many times while traveling through the interstellar medium, whereas the γ-rays travel in straight lines from their production sites. Because of the origin of this diffuse γ-ray emission, it is potentially able to reveal much about the sources and the propagation of cosmic rays. Furthermore, having a good understanding of the Galactic diffuse γ-ray emission is necessary - at least at GeV energies - to detect emission from faint sources.

Very high energy (VHE) γ-ray astronomy is a relatively young discipline. In the last few years, with the development of new observational techniques, such as ground-based Cherenkov telescopes like H.E.S.S., the number of known VHE γ-ray sources has greatly increased. The High Energy Stereoscopic System (H.E.S.S) is a system of

Imaging Atmospheric Cherenkov Telescopes (IACTs). It is comprised of four IACTs and is located in the Khomas Highland in Namibia. Cherenkov telescopes detect the Cherenkov light emitted by the charged particles in extensive air showers (EAS), which move with a speed greater than the speed of light in the air. These EAS are produced when VHE particles interact with the atmosphere.

So far upper limits on the diffuse γ-ray emission at TeV energies have been put by the Milagro (Abdo et al. 2008 (1)), the CASA-MIA (Borione et al. 1998 (25)) or the HEGRA (Aharonian et al. 2002 (8)) experiment. However, H.E.S.S. could provide very significantly improved measurements due to the higher sensitivity and angular resolution with respect to the previous experiments. The population of H.E.S.S. sources shows that all sources are located within a few degrees latitude from the Galactic plane (Aharonian et al. 2005 (11)). The diffuse γ-ray emission at low latitudes (b $\leq$ 2°) at TeV energies is contaminated by emission from sources, whereas at higher latitudes (b $\geq$ 4°) the contamination is significantly lower. However, the diffuse γ-ray emission at these latitudes is also lower and there might not be much left.

One of the future goals of H.E.S.S. is to measure the diffuse γ-ray emission at TeV energies. For that a specific region has to be chosen to look for this diffuse emission. An interesting region could be identified from model predictions. This reason is the purpose of this work, which is to estimate the diffuse γ-ray emission from regions of the Galaxy. The method used in this work is to model the Galactic diffuse γ-ray emission by assuming a distribution of sources randomly happening in the Galaxy, supernova remnants (SNRs) for protons and pulsars for electrons, and then calculate the spectrum of cosmic rays for different injection mechanisms of the sources. The so called γ-ray emissivity, which is the number of γ-rays per volume per second and energy can be calculated for points in space and then integrated along the line of sight to yield the flux of γ-rays. The final goal of this thesis is to calculate the γ-ray emission spectrum for two regions of the Galaxy.

1. INTRODUCTION

The most important quantity in this entire thesis is the γ-ray emissivity q, that is a short motivation of this quantity and how it is connected with the different chapter of my thesis is given.

In general the emissivity is the number of particles produced per second, per volume and per energy in a scattering process. The reaction rate per volume and per energy (emissivity) in a scattering process is defined by:

$$q = \dot{n} = \qquad n_b \qquad\qquad \times \qquad \sigma \qquad\qquad \times \qquad \phi_a$$

$$\downarrow \qquad\qquad\qquad \downarrow \qquad\qquad\qquad \downarrow$$

Target density	Cross-section	Particle flux
$\downarrow$	$\downarrow$	$\downarrow$
Chapter 3	Chapter 4	Chapter 2+5

where ϕ_a is the incoming particle flux, n_b ist the number density of target particles and σ is the cross section of the corresponding processes. A short overview of how this work is organized is given in the following:

- Chapter 2 is dedicated to the Interstellar Medium in which the cosmic rays interact either with gas or radiation fields.

- In chapter 3 the cosmic rays, their origin and how they propagate through the Galaxy is described.

- Then chapter 4 will give a short overview of the theory behind the production mechanisms of γ-rays.

- In chapter 5 the cosmic ray sources and their injection mechanisms is presented.

- Chapter 6 explains the model used to calculate the local cosmic ray spectrum at the position of the earth.

- In chapter 7 the final results for the calculated cosmic ray and diffuse γ-ray emission spectra for different regions of the Galaxy will be shown.

- Finally chapter 8 will give a conclusion and an outlook.

Chapter 2

Cosmic Rays

The measured atmospheric electricity, which means the ionization of the air, was long believed to be caused by radioactive elements in the ground or the radioactive gases produced by these radioactive elements, until in 1912 the Austrian astrophysicist, Victor Hess, carried out a series of balloon flights up to an altitude of 5300 meters. During these famous balloon flights Hess measured an increasing ionization rate with increasing altitude and concluded that the measured radiation, later named "cosmic rays" (CRs) by Millikan, was penetrating the atmosphere from above (Hess 1912). For his discovery Hess received the Nobel Price in 1936.

Nowadays we know that about 90% of the cosmic ray nuclei are hydrogen (protons), about 9% are helium (alpha particles) and the heavier nuclei make up only about 1%. The amount of electrons is about 1% of the CR protons at GeV energies. Most cosmic rays are relativistic, having kinetic energies comparable to or greater than their rest masses. Almost 100 years after the discovery of CRs three fundamental questions are still unanswered: What is their origin; where and how are CRs accelerated to those high energies?

CRs are the highest energy particles known to exist, of much higher energies than they are achievable by the Large Hadron Collider (LHC) at CERN or any other accelerator on Earth. CRs are not only a scientific challenge, also they have direct effects on the life of humans. They constitute a small but significant fraction of the annual radiation exposure of human beings on earth and some researchers have suggested that they might play a role in climate changes (Svensmark 2007 (57)).

2.1 The observed cosmic ray spectrum

2.1.1 CR proton energy spectrum

The all-particle energy spectrum (flux of all hadronic particles summed over all species as a function of total energy per nucleus), shown in Figure 2.1, is a featureless power-law $\frac{dN}{dE} \propto E^{-\Gamma}$ with spectral index Γ of 2.7 up to the so called *knee* at about 10^{15} eV, indicating non-thermal acceleration processes. Above the knee energy the spectrum of CRs softens to a power-law with spectral index of 3.1. The spectrum flattens again at the *ankle* at about 4×10^{18} eV.
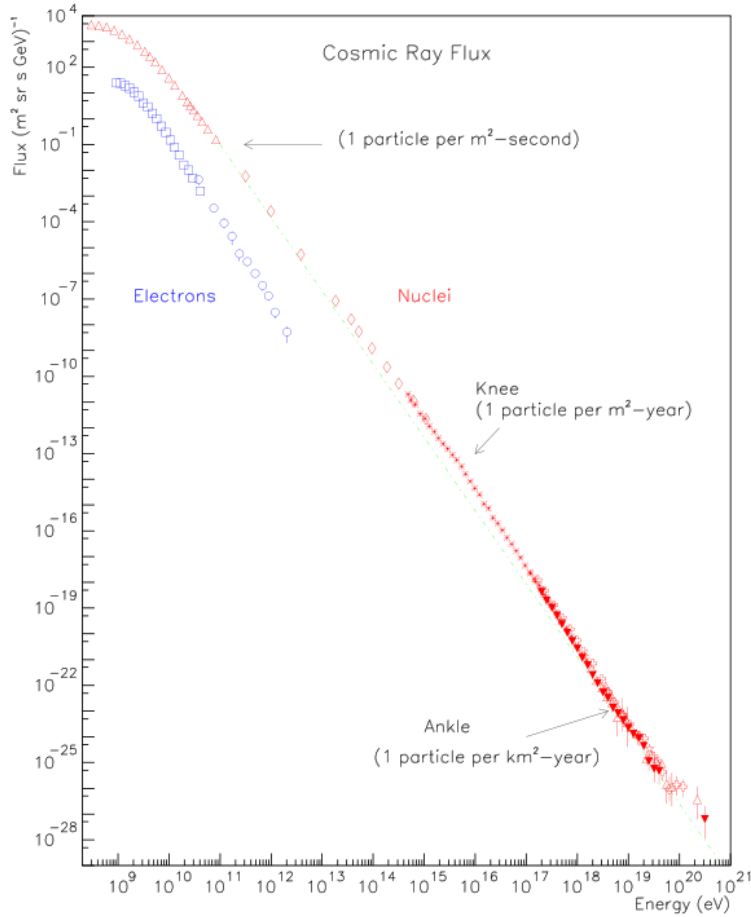

Figure 2.1: The cosmic ray energy spectrum

The gyroradius for diffusion of particles with energies above the ankle in the typical interstellar Galactic magnetic field (B=3μG) is comparable to the size of the Galaxy.

Thus, if these ultra-high energy (UHE) particles were of galactic origin one would expect large anisotropies in their arrival directions, which are not observed. The particles with energies above the ankle are therefore believed to be produced outside the Galaxy. In the following discussion, as well as the whole thesis only CRs which originate in the Galaxy will be considered.

The CR spectrum extends in energies from the MeV range to 10^{20} eV. The CR flux decreases from one thousand particles per square meter per second at GeV energies to one particle per square kilometre per century above 100 EeV (1EeV $= 10^{18}$eV). The observed CR energy density is about 1 eV/cm^3, of which more than 90% is carried by particles with energies less than 50 GeV.

2.1.2 CR electron energy spectrum

Many experiments on balloons and in space have extensively measured the spectra of CR hydrogen, helium, heavier nuclei, antiprotons, electrons and positrons. Various measurements of the cosmic ray electron spectrum are shown in Figure 2.2. It is an illustration of the cosmic ray electron flux scaled by the energy cubed, so that features can be seen in the otherwise very steep spectrum. Between roughly 10 GeV and 1 TeV it follows a power-law with an spectral index of $\Gamma = 3.3$. The bump in the spectrum be-
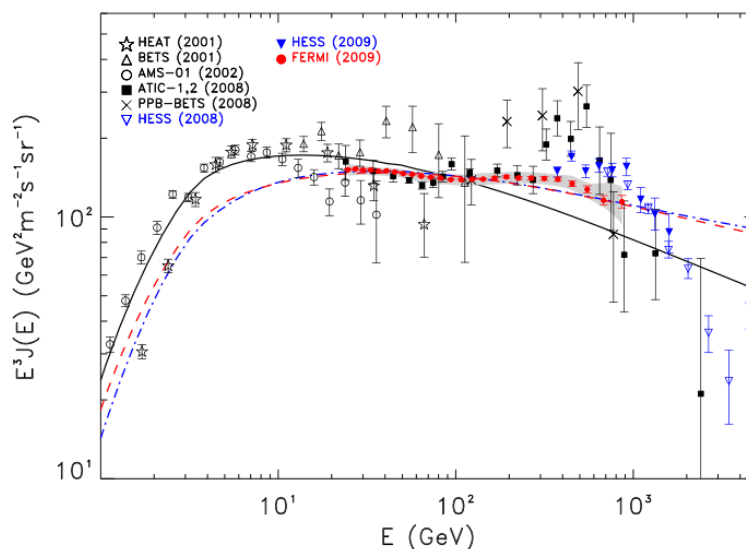

Figure 2.2: The cosmic ray electron energy spectrum. Figure from Moiseev et al. (2009) (45)

tween about 300 and 800 GeV was observed by the ATIC experiment and was recently interpreted as a signature of Kaluza-Klein dark matter particles annihilation (Chang et al. (2008)(39)). However newer measurements conducted by H.E.S.S. (Aharonian et al. 2009(15)) and FERMI (Abdo et al. 2009 (3)) shows no indication of this feature anymore.

2.2   The origin of Galactic cosmic rays

Diffusive shock acceleration (DSA) in the shells of supernova remnants (SNRs) is commonly believed to explain the Galactic CR spectrum. One of the main argument in favor of SNRs as the sources of CRs is that they provide the necessary amount of energy to account for the energy density of CRs (Ginzburg & Syrovatskii 1964 (36)). Assuming the average CR energy density in the Galaxy to be equal to the observed CR energy density at Earth of about $\rho_{CR} = 10^{-12}$ erg/cm$^3 \approx 1$ eV/cm^3, the power required to maintain this energy density is

$$\frac{\rho_{\mathrm{CR}} V_{\mathrm{disk}}}{\tau_{\mathrm{escape}}} = \frac{10^{-12} 10^{67}}{10^{14}} \sim 10^{41} \text{ erg/s} \tag{2.1}$$

where τ_{escape} ($\propto 10^7$ years) is the CR confinement time deduced from spallation (see section 2.3) and V_{disk} the volume of the Galactic disk. Assuming one supernova event every 30 years, the power required to maintain the CR energy density is about ten percent of the total kinetic power released by SNR events, the latter being 10^{51}erg/(30 yr) $\approx 10^{42}$ erg/s. This is in good agreement with the typical acceleration efficiency of relativistic particles in SNR shocks of 10%, as predicted in the theoretical work of e.g. (Drury & Voelk 1994 (32)). Assuming amplification of the magnetic field by the accelerating CRs, DSA in SNRs can explain the part of the observed CR spectrum up to the knee energy, at about 1 PeV=10^{15} eV, which is considered to be of Galactic origin (Blandford & Eichler 1987 (23)). However, if CRs up to 10^{18} eV have a Galactic origin, additional mechanisms such as special injection sources or re-acceleration are needed to push the maximum achievable acceleration energy up to EeV energies.

   The H.E.S.S. (Hofmann et al. 1999 (37); Aharonian et al. 2006 (12)) and the MAGIC telescope (Albert et al. 2008 (16)) have observed TeV (TeV=10^{12} eV) gamma rays from five shell-type SNRs, namely Cas A, RXJ1713.7-3946, RX J0852-4622, RCW

86 and SN 1006. Some SNRs were spatially resolved at TeV energies (Aharonian et al. 2004,2005 (9; 10); Aharonian et al. 2007 (13); Acero et al. 2010 (4)).

The detection of a number of SNRs in TeV gamma-rays, though supporting the SNR hypothesis for the origin of CR protons and nuclei, still does not constitute the final proof for it, mainly because competing leptonic processes, such as inverse Compton scattering of electrons on radiation fields. e.g. the cosmic microwave background, might also explain at least parts of the observed very high energy (VHE) gamma-ray emission.

2.3 Cosmic ray propagation in the Galaxy

Regardless of the nature of their sources, within which cosmic-rays are accelerated, the particles accelerated by individual sources in the Galaxy mix together, lose memory of their origin and contribute to the bulk of Galactic CRs known as the CR *sea*, or CR background.

Primary nuclei are the nuclei which are accelerated in the original sources. Secondary nuclei are those essentially absent in the sources, which can be produced by spallation of primary nuclei of larger mass number. To the extent that spallation cross sections are not energy dependent, the spectral index at production for a secondary nucleus is the observed spectral index of its parent. Thus for a secondary nucleus the spectrum at production is

$$\frac{dN}{dE_{\text{secondary}}} \propto \tau_{\text{escape}} \frac{dN}{dE_{\text{observed}}}, \tag{2.2}$$

where τ_{escape} is the CR confinement time in the Galaxy and the observed spectrum, dN/dE_{observed}, has an spectral index of 2.7. The comparison of the spectrum of secondary nuclei to that of the parent primary nuclei (for instance Boron/Carbon or sub-Fe/Fe data) tells us that cosmic protons and nuclei diffuse in the magnetic fields for times in the order of $\tau_{\text{escape}} \sim 10^7 (\frac{E}{10\text{GeV}})^{-\delta_1}$ years before escaping the Galaxy. Here E is the particle energy and the dimensionless parameter $\delta_1 \simeq 0.6$. The confinement time decreases with increasing energy. The measurements of CR antiprotons, which are produced primarily by CR protons are consistent with the propagation parameters determined from the ratios of secondary to primary nuclei (Adriani et al. 2009 (5); Strong, Moskalenko and Ptuskin 2007 (56)). The energy dependence of the CR propagation in the Galactic disk is often parameterized by a power law of the form

$D(E) = D_{10} \left(\frac{E}{E_\star}\right)^\delta$, with a diffusion coefficient D_{10} at a specific energy $E_\star$ and δ can vary between 0.3 and 0.7 (Berezinskii et al. (1990) (19))

By neglecting energy gains and losses as well as convection, the equilibrium solution of the CR transport equation including propagation and acceleration implies that the observed CR spectrum is given by

$$\tau_{\text{escape}} \, Q_{\text{source}}(E) \propto \frac{dN}{dE_{\text{observed}}} \rightarrow Q_{\text{source}}(E) \propto E^{\delta_1} \frac{dN}{dE_{\text{observed}}} \tag{2.3}$$

where $Q_{\text{source}}(E)$ is the source spectrum. Thus, the source spectrum's spectral index must be close to 2.1 for $\delta_1 = 0.6$. This is in agreement with theoretical work on diffusive shock acceleration in the shells of SNRs, which predicts an acceleration spectrum close to a power-law E^{-2}. However, by allowing that the CRs might be re-accelerated in the ISM, the source spectrum may very well be steeper, close to an spectral index of 2.4 (Berezinskii et al. 1990 (19)).

.

Chapter 3

The Interstellar Medium

3.1   Introduction

In this chapter the few components of the interstellar medium (ISM) are explained. First I am going to discuss how the interstellar gas is detected and then why radiation fields are important and how they are described. The measured gas density is important for the calculations conducted in this work, since in interactions of cosmic rays with the ISM the number density of the target gas plays an important factor in the emissivity of produced γ-rays, as mentioned in the introduction.

The ISM contains gas, dust particles, magnetic fields, radiation fields and cosmic rays. Interstellar space typically contains about one gas atom per cubic centimeter. The energy density of the different components of the ISM are the following, the radiation fields e.g. the cosmic microwave background (CMB) has an energy density of 0.25 eV/cm^3, for the magnetic field assuming a magnetic field strength of 5 μG it is approximately 0.6 eV/cm^3 and for the cosmic rays it is about 1 eV/cm^3. These different components are strongly coupled to one another and are therefore described as a single dynamical entity called the interstellar medium. The ISM, which strongly influences the Galactic evolution, has been extensively studied at all wavelengths. In particular radio emission from atomic hydrogen traces the distribution of the most common atomic gas, while submillimetre emission from CO and other molecules can be used as a tracer of molecular hydrogen given an abundance ratio X. The distribution of ISM material and the influence of magnetic fields on it (which is partly determined by ionisation due to

cosmic ray bombardment) constitute the initial conditions for star formation and are therefore important for studies of this phenomenon as well as for galaxy evolution.

3.2 Detection of interstellar gas

Interstellar atomic gas can be detected by emission or absorption lines in the spectrum. Absorption lines can only be observed if there is a bright star behind the observed object. Because of the large dust extinction, no observations of molecules in the densest molecular clouds (MCs) can be made in optical and ultraviolet spectral regions. This means that only radio observations are possible for these MCs, where molecules are especially abundant.

Radio astronomy covers a frequency range from a few megahertz up to frequencies of about 300 GHz. Much of the knowledge about the structure of the Milky Way comes from radio observations of the 21 cm line of neutral hydrogen and, more recently, from the 2.6 mm line of the carbon monoxide molecule. A radio telescope is used to collect radiation in an aperture or antenna, from which it is transformed to an electric signal by a receiver. Those radio telescopes measure a specific intensity I_ν at frequency ν, of a beam of radiation.[1] This intensity is the energy flux in the beam per unit solid angle and per unit frequency.

Beginning from the radiation transport equation (see also Binney & Merrifield 1998(22)):

$$\frac{dI_\nu}{d\tau_\nu} + I_\nu = S_\nu \tag{3.1}$$

where S_ν is the source function and τ_ν is the optical depth. The integration of eq. (3.1) with a constant source function S_ν, that is described assuming that the gas is in thermodynamical equlibrium by the Planck spectra $B_\nu = \frac{2h\nu^3}{c^2} \frac{1}{e^{\frac{h\nu}{kT}} - 1}$, yields:

$$I_\nu(\tau_\nu) = I_\nu(0) e^{-\tau_\nu} + B_\nu \left(1 - e^{-\tau_\nu}\right) \tag{3.2}$$

At radio frequencies, normally the Rayleigh-Jeans criterium can be used, $\frac{h\nu}{kT} \ll 1$, and Eq. (3.2) becomes:

$$I_\nu(\tau_\nu) = I_\nu(0) e^{-\tau_\nu} + \frac{2kT\nu^2}{c^2} \left(1 - e^{-\tau_\nu}\right) \tag{3.3}$$

---

[1] $I_\nu [W Hz^{-1} m^{-2} sterad^{-1}]$

If I_ν is now expressed using the brightness temperature defined by $T_B = \frac{c^2}{(2k\nu^2)} \cdot I_\nu$, equation (3.3) becomes:

$$T_B\left(\tau_\nu\right) = T_B\left(0\right)e^{-\tau_\nu} + T\left(1 - e^{-\tau_\nu}\right) \tag{3.4}$$

In the optically thin limit which corresponds to small τ_ν and for the case of negligible $T_B(0)$, eq. (3.4) can be approximated as:

$$T_B\left(\tau_\nu\right) \approx \tau_\nu T \tag{3.5}$$

Under the assumption of constant S_ν, the optical depth τ_ν is proportional to the column density of material along the line of sight. Consequently if the medium is optically thin and $T_B(0)$ is negligible, T_B is also proportional to the column density (see also Binney & Merrifield 1998(22)). If the medium is optically thick however, T_B measures its temperature rather than its column density.

3.2.1 Observation of atomic hydrogen (H_1)

The H_1 is one part of the gas component of the ISM. It is distributed quite uniformly in the spiral arms of the galaxies and can be directly observed looking at the 21 cm emission line of the hyperfine transition. The ground state of the atomic hydrogen is split into two hyperfine levels defined by F= 0, where the spins of proton and electron are antiparallel and F= 1, where both spins are parallel. Photons emitted in the transition have a frequency of $\nu = 1.4204$ GHz, so that the energy of a photon becomes roughly $h\nu \approx 5.9 \times 10^{-6}$ eV. Since the temperature of the ISM cannot fall below that of the cosmic background radiation, which corresponds to kT= 2.3×10^{-4} eV, it follows that the Rayleigh-Jeans criterium is sufficiently fulfilled, because $\frac{5.9 \cdot 10^{-6}}{2.3 \cdot 10^{-4}} = 2.57 \cdot 10^{-2} \ll 1$.

The value of the total neutral hydrogen column density N_H is described by (Binney & Merrifield 1998(22))

$$N_H = 1.82 \cdot 10^{22} \int_{-\infty}^{\infty} dv\, T\tau(v) \text{ atoms } m^{-2} \tag{3.6}$$

where $\tau(v)$ is the optical depth that depends on the radial velocity v of the atoms in the observed gas. For an optically thin material $T\tau(v)$ can be replaced in eq. (3.6) by the brightness temperature T_B:

$$N_H(l,b) = 1.82 \cdot 10^{22} \int_{-\infty}^{\infty} dv\, T_B(l,b,v) \text{ atoms } m^{-2} \tag{3.7}$$

3. THE INTERSTELLAR MEDIUM

The relationship between the radial velocity of the gas and the distance from us is shown in Fig. (3.1): There are two distance solutions for each radial velocity in the inner Galaxy. In order to resolve this near-far distance ambiguity, the method by (Nakanishi & Sofue 2003 (46); Nakanishi & Sofue 2006(47)) can be adopted.
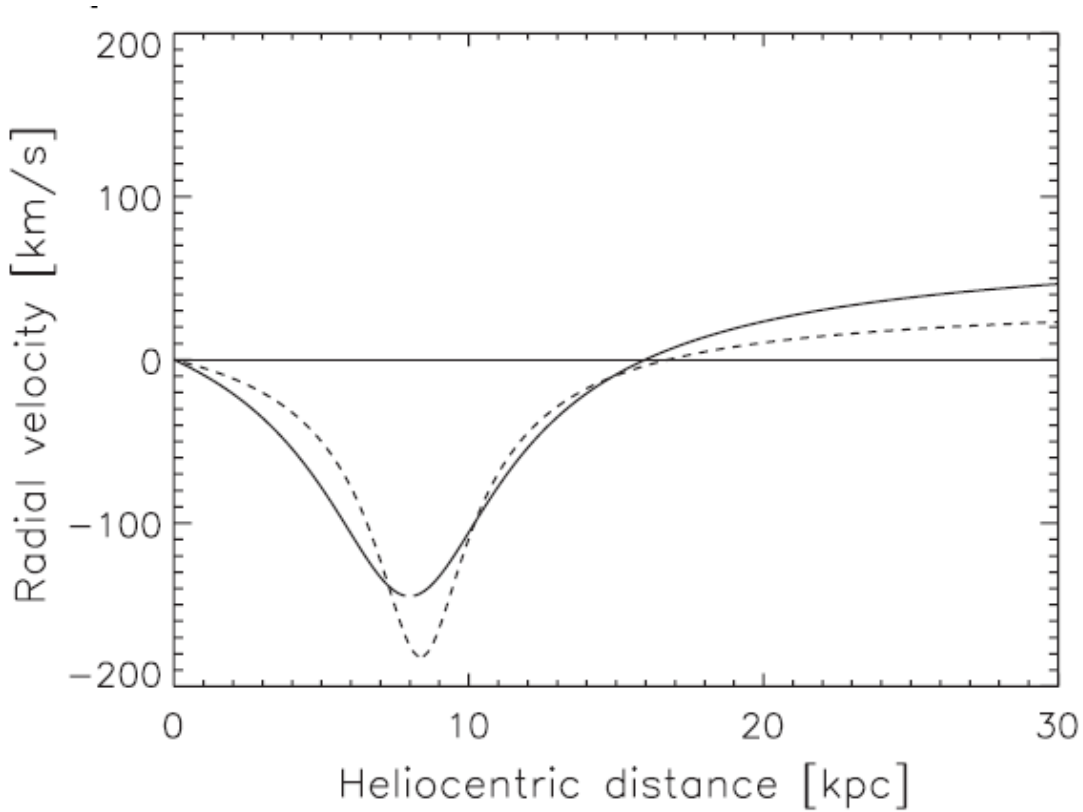

Figure 3.1: This plot shows the radial velocity v vs heliocentric distance estimated from flat rotation of the galactic disk. The solid line is at l=340° (longitude) and b=0° (latitude) and the dashed line is at l=350° (longitude) and b=0° (latitude). Taken from Casanova et al. 2010 (28)

The following Fig. (3.2) shows the H_1 column density distribution over the whole galaxy in an aitoff projection. For that the FITS data file of the Leiden/Argentine/Bonn H1 Survey [1] has been used (see Kalberla et al. (2005)(40)).

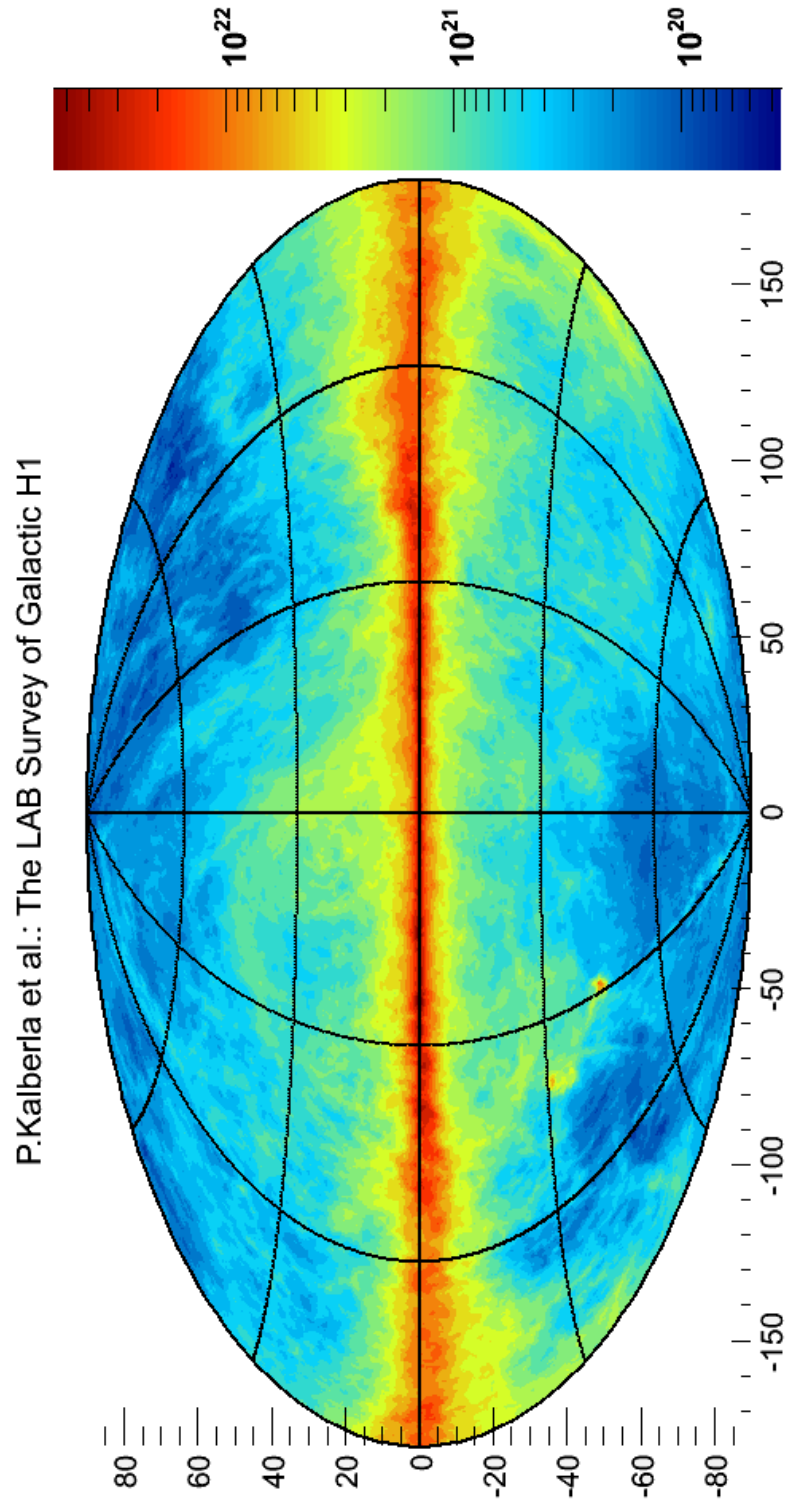[1] http://www.astro.uni-bonn.de/~webaiub/english/tools_labsurvey.php

Figure 3.2: H_1 column density distribution in units of 1 cm^{-2} over the whole galaxy. x-axis shows longitude between -180° < l < 180° and -90° < b < 90°. FITS file from P. Kalberla et al. 2005(40)
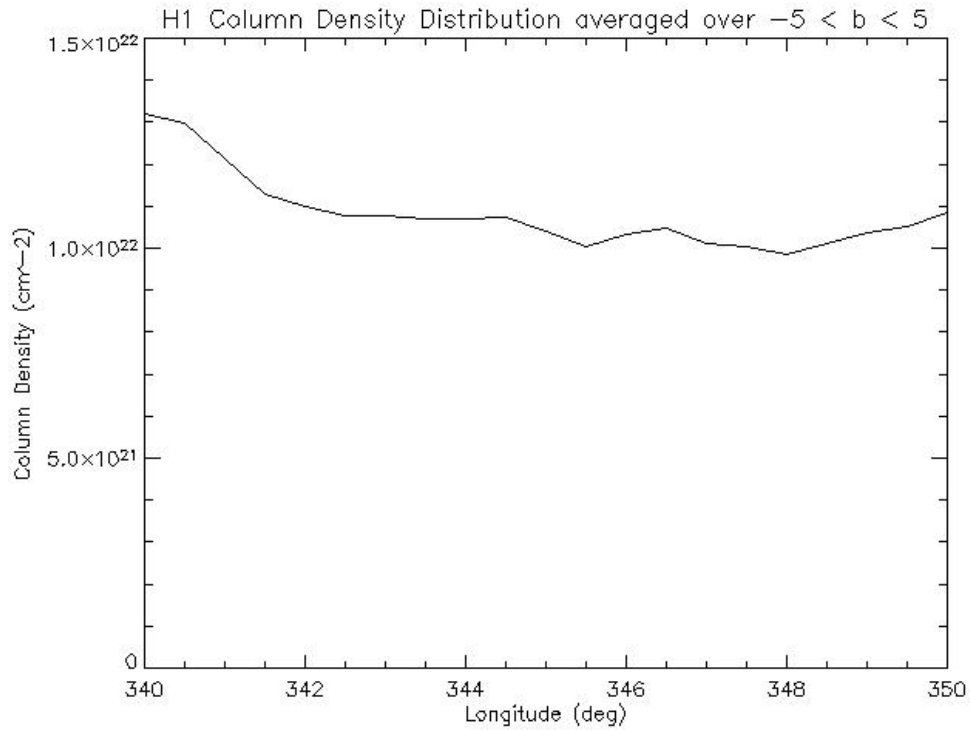
Figure 3.3: H_1 column density distribution in longitude in units of 1 cm^{-2} over region -5° < b < 5° in latitude. FITS file from P. Kalberla et al. 2005(40)
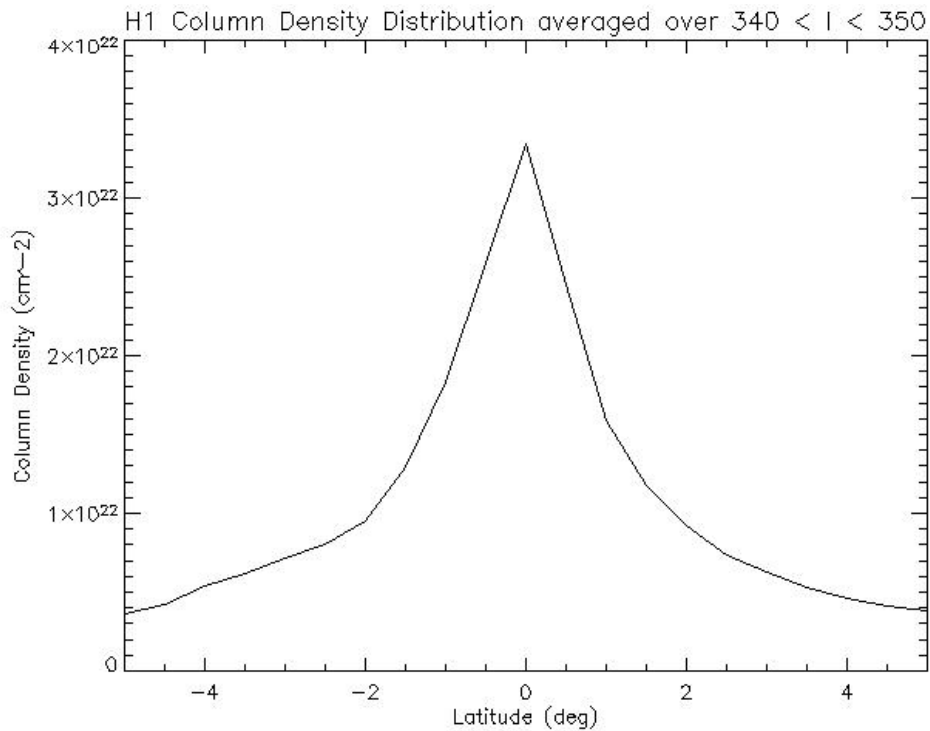

Figure 3.4: H_1 column density distribution in latitude in units of 1 cm^{-2} over region 340° < l < 350° in longitude. FITS file from P. Kalberla et al. 2005(40)

3.2.2   Observation of molecular hydrogen (H_2)

The detection of molecular hydrogen has been one of the most important achievements of UV astronomy. It is not distributed uniformly like atomic hydrogen but rather concentrated in dense clouds. Interstellar dust is needed to shield the molecules from the stellar UV radiation, which would otherwise dissociate them. Molecular hydrogen is thus found where dust is abundant, like in molecular clouds for example. Since H_2 is a homonuclear molecule it has no net electric dipole moment in the ground state. Thus, it is almost impossible to observe H_2 directly in the cold, generally obscured interstellar regions where those molecules form and survive, like the dense cores of molecular clouds. Fortunately, the next most abundant molecule after the H_2 is carbon monoxide (CO) and is a good tracer for the molecular hydrogen. That is because both form on the same timescale within MCs, therefore their number densities are connected. The spectra of CO has readily observed mm-band lines, which are formed by a change of angular momentum by $\hbar$ while retaining the same electronic and vibrational quantum numbers. So the energies of these rotational transitions fall in the mm wavebands. For CO the most important lines are at wavelengths of 2.6 mm and 1.3 mm. Since the ISM is often optically thick in the 2.6 mm line the above derivation of the column density for H_1 does not hold for the case of H_2. The solution is to report the result in terms of the measured antenna temperature T_A, which is the temperature required of a black-body that fills the telescope beam in order to generate the same signal as the source being measured. Define:

$$I_{\text{CO}} = \int dv \, T_A(\text{2.6 mm line of } {}^{12}\text{CO}) \tag{3.8}$$

as the CO brightness temperature of the 2.6 mm line with units in [K km/s]. Studies of molecular clouds in the Milky Way yield a conversion factor from CO brightness temperature to H_2 column density of (see Dame et al. (2001)(31))

$$\text{X} \equiv \frac{N(\text{H}_2)}{I_{\text{CO}}} \simeq 1.8 \times 10^{20} \text{ cm}^{-2} \text{ K}^{-1} \text{ km}^{-1} \text{ s} \tag{3.9}$$

In the following the CO distribution from NANTEN FITS files will be shown. The NANTEN Observatory[1] is a international collaboration and is located in the Atacama desert of Chile. It is equipped with a 4 m submillimeter telescope and is used to survey the southern sky in molecular and atomic spectral lines. Both Fig. (3.5) and Fig. (3.5)

---

[1] http://www.astro.uni-koeln.de/nanten2/node/10

are between 343° and 351° in longitude but this is just an excerpt of the available data which has a range of $340° < l < 351°$ and $-5° < b < 5°$.

The first plot features the galactic plane between longitude values of 343° and 351° and latitude values between $-2°$ and $2°$. The color scale represents the column density of H_2 in units of cm^{-2}.
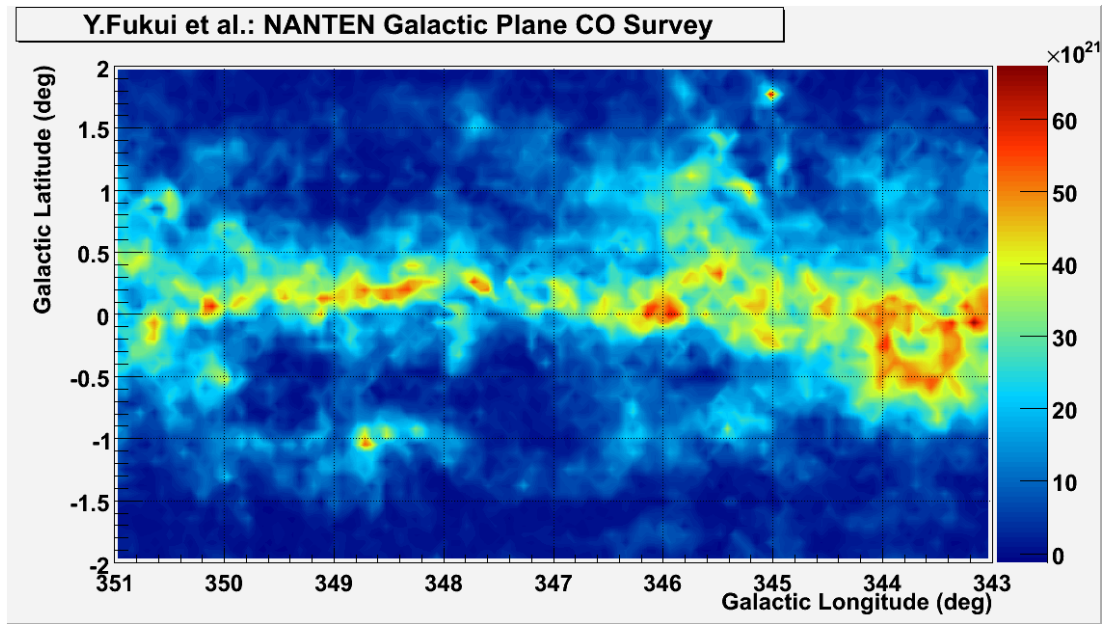

Figure 3.5: CO distribution from NANTEN FITS files, by courtesy of Y. Fukui

The second plot is in the same longitude region but this time shows the velocity against longitude. It can be seen that most of the H_2 is located in the vicinity of our solar system, see Fig. (3.1).
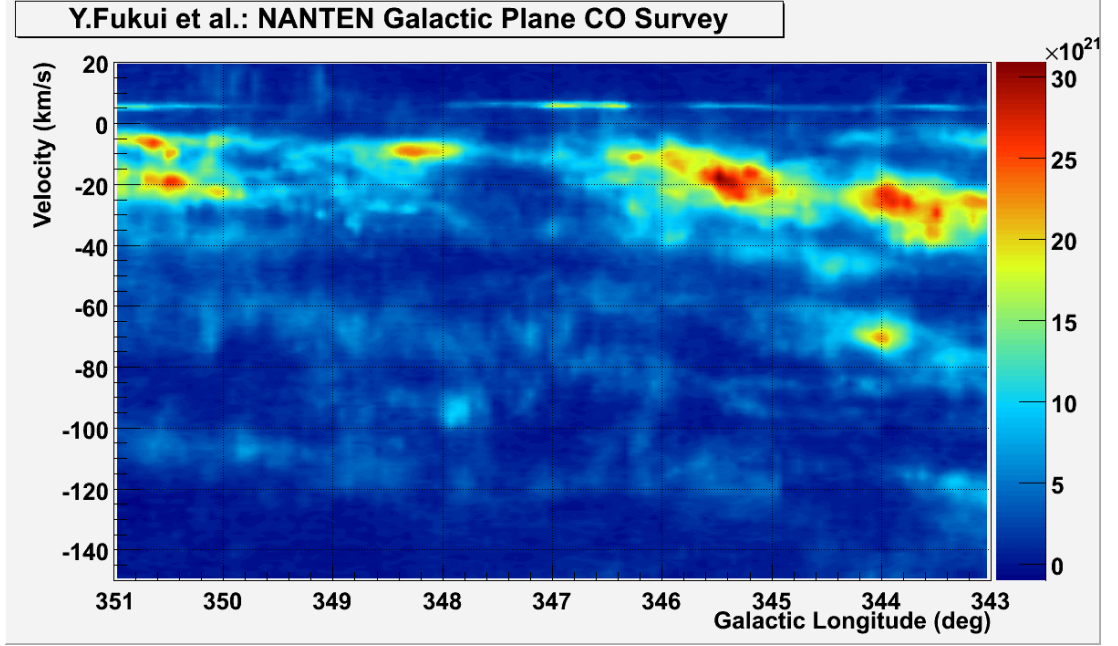

Figure 3.6: CO distribution from NANTEN FITS files, by courtesy of Y. Fukui

The averaged column density with respect to l (longitude) and b (latitude) has been plotted using:

$$\bar{N}_{H_2}(b) = \frac{\int_{\text{lmin}}^{\text{lmax}} N_{H_2}(l,b)dl}{l_{\max} - l_{\min}} \qquad (3.10)$$

This is shown in Fig. (3.7) and with

$$\bar{N}_{H_2}(l) = \frac{\int_{\text{bmin}}^{\text{bmax}} N_{H_2}(l,b)db}{b_{\max} - b_{\min}} \qquad (3.11)$$
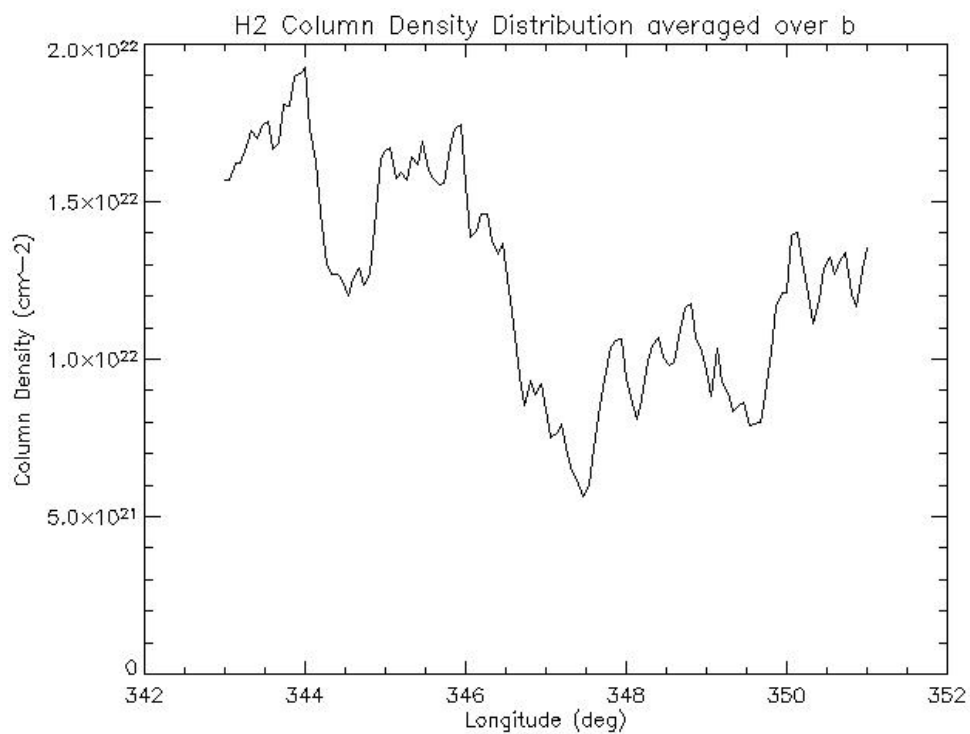
the Fig. (3.8) can be shown.

Figure 3.7: CO distribution in longitude averaged over region -2° < b < 2° in latitude from NANTEN FITS files, by courtesy of Y. Fukui

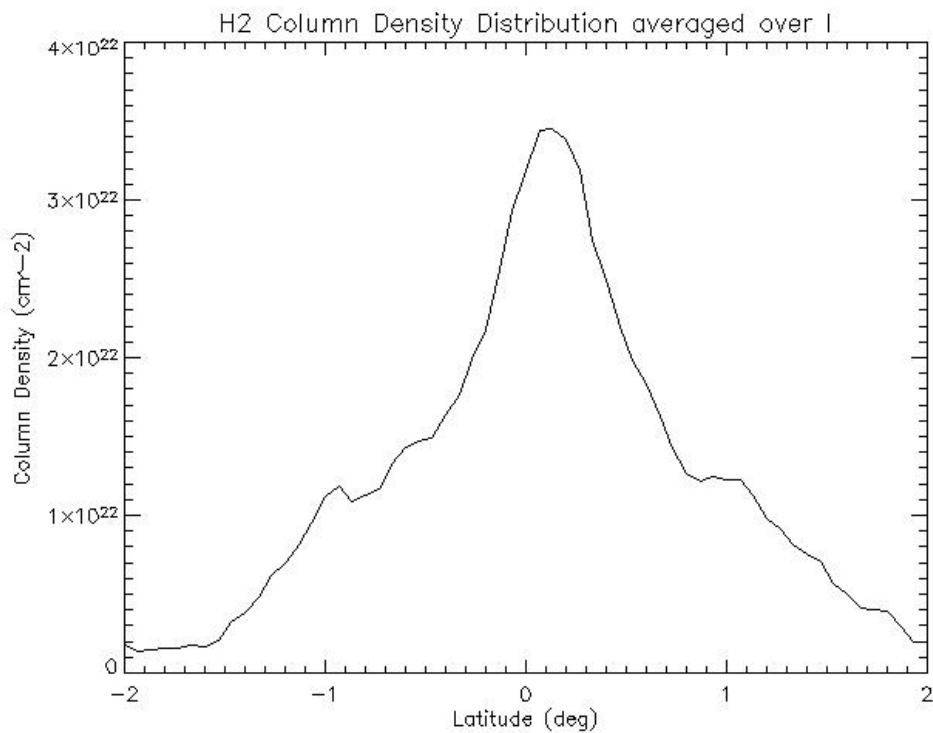**Figure 3.8:** CO distribution in latitude averaged over region 343° < l < 351° in longitude from NANTEN FITS files, by courtesy of Y. Fukui

3.3 Interstellar radiation fields

This section is dedicated to the various radiation fields that fill up galaxies, off which electrons can produce γ-rays through Inverse Compton scattering (see section 4.2.2). Firstly, there are the radiation fields produced by stars in the optical regime. Additionally, there are radiation fields produced by interstellar dust through absorption of ultraviolet and optical photons and re-emitting at infrared wavelengths. At last there is the omnipresent Cosmic Microwave Background.

The interstellar radiation field at a position $\mathbf{r}$ can be represented by the sum of diluted blackbody distributions also referred to as graybody distributions plus the cosmic microwave background. The number density of photons per unit volume and energy interval for graybody distributions is

$$n_G(\epsilon, \mathbf{r}) = \frac{15\omega(\mathbf{r})}{\pi^4 (k_B T)^4} \frac{\epsilon^2}{\exp\left[\epsilon/(k_B T)\right] - 1} \tag{3.12}$$

It is characterized by the photon energy density $\omega(\mathbf{r})$ at position $\mathbf{r}$ and the temperature T. The greybody distribution has the same energy dependence as the Planck blackbody distribution but smaller photon number densities by a factor of $\omega(\mathbf{r})/\omega_B$. ω_B is the energy density of the blackbody distribution which is given by the Stefan-Boltzmann law

$$\omega_B = \frac{\pi^2 (k_B T)^4}{15(\hbar c)^3} \tag{3.13}$$

The various electromagnetic radiation fields in the vicinity of the solar system are given by table 3.1 (taken from Schlickeiser (2002) (51))

i	T_i/K	W_i/eV cm^{-3}	Comment
1	20000	0.09	spectral type B
2	5000	0.3	spectral type G-K
3	20	0.4	infrared
4	2.7	0.25	CMB

Table 3.1: Electromagnetic graybody radiation fields in the local interstellar medium

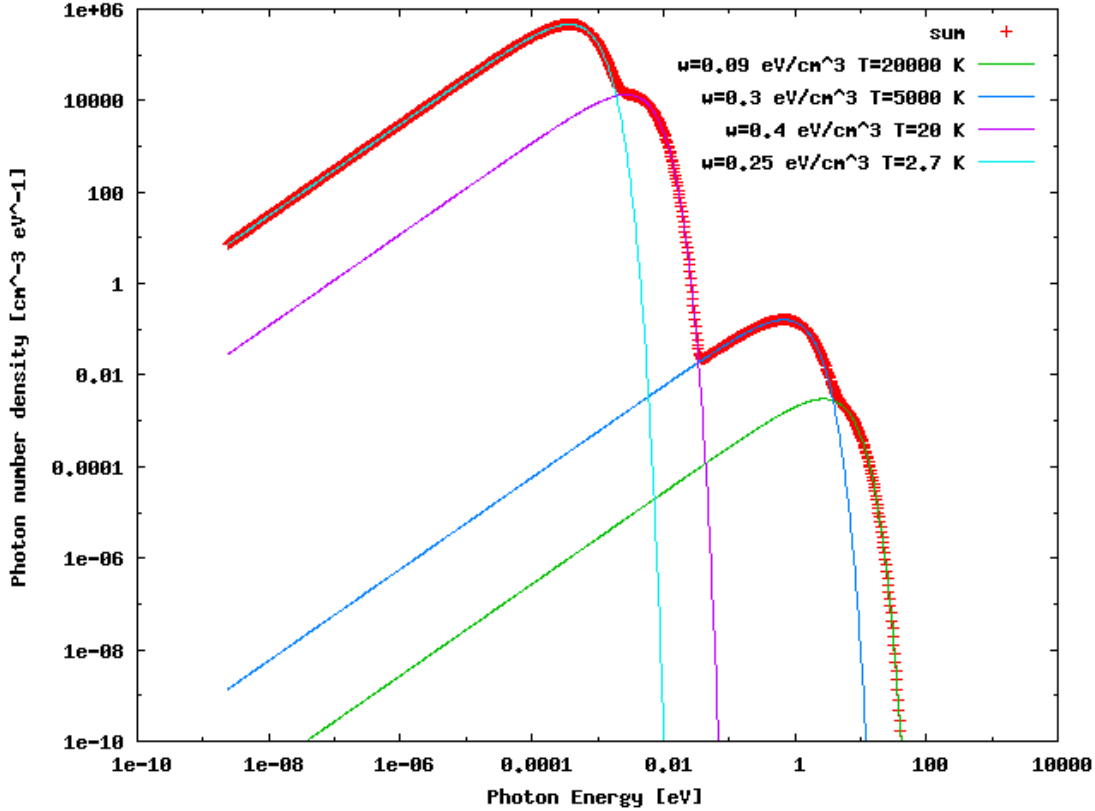In the following figure the various greybody distributions are plotted

Figure 3.9: Interstellar radiation fields: CMB (light blue) with $\omega = 0.25$, T = 2.7 K; infrared (purple) with $\omega = 0.4$, T = 20 K; spectral type G-K (dark blue) with $\omega = 0.3$, T = 5000 K; spectral type B (green) with $\omega = 0.09$, T = 20000 K

One can see from figure 3.9 that the various radiation fields have their maxima at different photon energies. Furthermore, the number density increases strongly from the optical to the CMB radiation field, since the energy densities have about the same order of magnitude but the temperature is quite different. For the IC scattering one has to integrate over the target photon field in the energy range of $[\epsilon_{min} , \epsilon_{max}]$, which in case of the 4 different radiation fields is chosen to be $[10^{-8} , 100]$ eV. However, integrating the CMB, the energy range of integration is assumed to be $[10^{-8} , 10^{-2}]$ eV.

Chapter 4

Production mechanisms for γ-rays

4.1 Cosmic rays interacting with the ISM

While escaping their injection sources and diffusing in the Galaxy, CR protons and nuclei collide with the atoms and molecules of the ISM gas and produce gamma rays through decay of neutral pions. CR electrons emit gamma-rays through inverse Compton scattering off the radiation fields and through bremsstrahlung processes. Whereas CRs diffuse in the Galactic magnetic fields and lose the memory of their site of injection, the gamma rays, being neutral, travel in straight lines from the site where they were emitted to the detector. The gamma-ray emission has long been recognised as a unique probe of the parent CR distribution because the resultant gamma-ray emissivity is a function only of the matter and radiation density and of the CR spectrum (Strong et al. 2004 (55); Bertsch et al. 1993 (20)). The spatial and spectral distribution of the Galactic gamma-ray spectrum therefore provide crucial information concerning the unknown CR flux in the different regions of the Galaxy.

The satellite Fermi, launched about 2 years ago, is providing new gamma-ray data in the MeV-GeV energy range. Recent observations show that the spectra of the Galactic diffuse emission, at least at intermediate latitudes $10\,^{\circ} < b < 20\,^{\circ}$, can be explained by cosmic-ray propagation models based on the locally measured cosmic-ray electron and nuclei spectra (Abdo et al. 2009 (2)). Interestingly, based on data collected by the EGRET detector (the most important satellite mission before Fermi) the diffuse

gamma-ray emission from the inner Galaxy at energies greater than about 1 GeV exceeds, by some 60%, the intensity predicted by model calculations performed, for instance, in Strong et al. (2004) (55), which assume that the CR flux throughout the Galaxy is equal to that measured in the vicinity of the Earth.

At TeV energies the spectral features of the gamma-ray emission detected by High Energy Stereoscopic System (H.E.S.S.) from the Galactic centre (GC) region and from the SNR W28 (Aharonian et al. 2008 (14)), and the diffuse emission from the Galactic disk measured by Milagro (Abdo et al. 2008 (1); Casanova & Dingus 2008 (27)), suggest that the CR flux might significantly vary in the different locations of the Galaxy.

In the following chapter a summery of the different production mechanisms through which CRs can produce γ-rays will be given. Futhermore, the corresponding cross-sections, which are another factor in the future calculation of the γ-ray emissivity, will be shown.

4.2 Leptonic production mechanisms

Electrons can lose energy through several interaction processes, three of which are the most important ones at high energies. The other interaction processes, namely triplet pair production, ionization and excitation of atoms and molecules as well as Coulomb interactions with ionized plasmas can be neglected.

- nonthermal bremsstrahlung produced in the ISM

- Inverse Compton scattering off radiation fields

- synchrotron radiation in cosmic magnetic fields

The next two subsections are dedicated to the first two processes, namely Bremsstrahlung and Inverse Compton because those are included in my calculations. Synchrotron radiation is neglected because it falls in the X-ray band rather then in the γ-band.

4.2.1 Bremsstrahlung

Bremsstrahlung or free-free emission arises as a result of charged particles deflected in the electric field of an atom or molecule. This deflection causes the charged particle to decelerate by emission of radiation. The differential cross-section for this interaction is taken from Blumenthal and Gould (1970)(24):

$$d\sigma = \alpha r_0^2 (dk/k)(E_i^2)^{-1} \cdot \left[(E_i^2 + E_f^2)\phi_1 - \frac{2}{3}E_i E_f \phi_2 \right] \tag{4.1}$$

where E_i and E_f are the initial and final (meaning after the scattering process) electron energy respectively. The functions $\phi_1(E_i, E_f)$ and $\phi_2(E_i, E_f)$ are energy dependent scattering functions depending on the structure of the atom. With the quantity $k = E_i - E_f = E_\gamma$, $r_0^2 = \frac{3}{8\pi} \cdot \sigma_T$ and $E = E_i$ one can rewrite eq (4.1) to yield (see also Bethe Heitler (1934)(21)):

$$\frac{d\sigma}{dE_\gamma} = \frac{3}{8\pi} \frac{\alpha \cdot \sigma_T}{E_\gamma} \left[\left[1 + \left(1 - \frac{E\gamma}{E} \right)^2 \right] \phi_1 - \frac{2}{3} \left(1 - \frac{E\gamma}{E} \right) \phi_2 \right] \text{cm}^2 \text{ eV}^{-1} \tag{4.2}$$

where $\alpha \approx 1/137$ is the fine structure constant and σ_T the Thomson cross section. In the case where the scattering system is an unshielded charge Ze, it follows that $\phi_1 = \phi_2 = Z^2 \phi_u$ with

$$\phi_u = 4 \left[\ln \left[\frac{2E}{mc^2} \left(\frac{E - E_\gamma}{E_\gamma} \right) \right] - \frac{1}{2} \right] \tag{4.3}$$
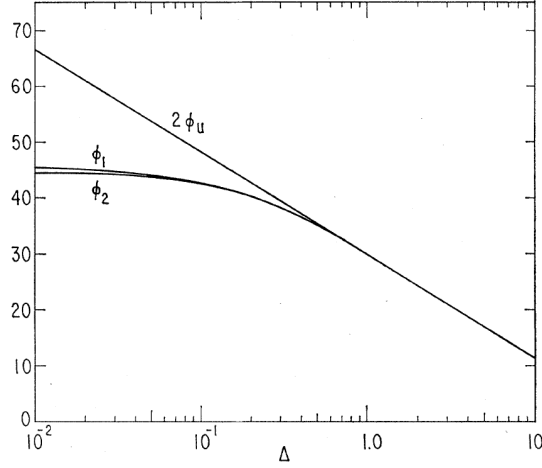
Figure 4.1: Energy dependent scattering functions ϕ_1 and ϕ_2 of atomic hydrogen as well as the unshielded function $2\phi_u$. Taken from Blumenthal and Gould 1970 (24)

Defining a dimensionless parameter that describes the fraction of the screening

$$\Delta = \frac{E_\gamma mc^2}{4\alpha E(E - E_\gamma)} \tag{4.4}$$

the Fig. (4.1) above can be shown. The curves represent the transition from complete screening ($\Delta \ll 1$, which corresponds to incident electrons with a high energy) to weak screening ($\Delta \gg 1$ which corresponds to low but still relativistic electron energies). Thus Fig. 4.1 compares the cross-section of an electron incident on a hydrogen atom, with the cross-section of an electron incident on an unshielded free proton and an unshielded free electron. Due to some approximations in the derivations of the scattering functions ϕ_i, the unshielded expression ϕ_u should be used instead of the computed ϕ_i for values $\Delta > 2$. The following table 4.1 displays the computed values for the scattering functions ϕ_i after Blumenthal and Gould (1970) (24):

The energy loss rate is different depending on the screening, but in all cases it is essentially linearly proportional to the relativistic electron Lorentz factor γ and therefore to the energy:

$$-\frac{dE_e}{dt} \propto E_e \cdot n \tag{4.5}$$

where n is the target number density of the gas. Assuming a typical number density of 1 cm^{-3} in the ISM, the time scale of energy loses is $\tau_{\text{brems}} \propto \frac{E}{dE/dt} \propto 10^8$ yr.

Table 4.1: Scattering functions ϕ_i for atomic hydrogen and helium

Δ	H		He	
	ϕ_1	ϕ_2	ϕ_1	ϕ_2
0	45.79	44.46	134.60	131.40
0.01	45.43	44.38	133.85	130.51
0.02	45.09	44.24	133.11	130.33
0.05	44.11	43.65	130.86	129.26
0.1	42.64	42.49	127.17	126.76
0.2	40.16	40.19	120.35	120.80
0.5	34.97	34.93	104.60	105.21
1	29.97	29.78	89.94	89.46
2	24.73	24.34	74.19	73.03
5	18.09	17.28	54.26	51.84
10	13.65	12.41	40.94	37.24

If the electron spectrum has the form of a power-law like $\frac{dN_e}{dE_e} \propto E_e^{-\Gamma}$ then the resulting γ-ray spectrum has the same form $\frac{dN_\gamma}{dE\gamma} \propto E_\gamma^{-\Gamma}$.

4.2.2 Inverse Compton (IC)

The Inverse Compton effect can be regarded as the opposite mechanism of ordinary Compton scattering. In the latter, the focus lies on the electron that is accelerated by an incoming photon, where as in the inverse Compton effect the focus lies on the photon which is blue-shifted by an incoming electron. So in this interaction the target photon receives a part of the kinetic energy of the incoming relativistic electron and is scattered to higher frequencies. There are two energy regimes in which the Inverse Compton cross-section can be approximated by convenient expressions. The first regime corresponds to the Thomson limit which is given if the initial energy of the photon in the electron rest frame ϵ' is much less then the electrons rest energy $m_0 c^2$ ($\epsilon' \ll m_0 c^2$), or using the dimensionless parameter if $\Gamma_e = 4\epsilon\gamma/m_0 c^2 \ll 1$.[1] In this case the cross-section becomes independent of the incoming photon energy. The second regime corresponds to the Klein-Nishina limit which is given by the opposite case, where $\epsilon' \gg m_0 c^2$ or $\Gamma_e \gg 1$.

---

[1]The quantities with a ′ denote that they are taken in the rest frame of the electron.

4. PRODUCTION MECHANISMS FOR γ-RAYS

4.2.2.1 Thomson limit

In the Thomson limit ($\Gamma_e \ll 1$) the energy loss rate of electrons can be described by

$$\frac{dE_e}{dt} = -\frac{4}{3}\sigma_T c \gamma^2 U_{\mathrm{rad}} \tag{4.6}$$

where U_{rad} is the energy density of the radiation field and γ is the Lorentz-factor of the electrons given by $\gamma = \frac{E_e}{mc^2}$. As it can be seen, the energy loss of the electrons is proportional to γ^2. The maximum energy $\epsilon_{1,\mathrm{max}}$ a scattered photon can obtain is derived by Blumenthal & Gould (1970) to be

$$\epsilon_{1,\mathrm{max}} \propto \gamma^2 \epsilon \tag{4.7}$$

However the typical energy of the upscattered photon is still small compared to the initial electron energy, which means that in the Thomson limit the electron loses its energy in small steps. The cross section in this case can be expressed as:

$$\sigma_T = \frac{8\pi}{3}\left(\frac{\alpha\hbar}{m_e c}\right)^2 \tag{4.8}$$

4.2.2.2 Klein-Nishina limit

In the Klein-Nishina limit the electron recoil becomes significant because a large fraction of the electron energy can be transferred to per scattering event. The full Klein-Nishina differential cross section can be expressed as:

$$\frac{d\sigma}{dE_1} = \frac{3\sigma_T}{4\epsilon\gamma^2}G(q,\Gamma_e) \; \mathrm{cm}^2 \; \mathrm{eV}^{-1} \tag{4.9}$$

with

$$G(q,\Gamma_e) = \left[2q\ln q + (1+2q)(1-q) + \frac{1}{2}\frac{(\Gamma_e q)^2}{1+\Gamma_e q}(1-q)\right] \tag{4.10}$$

where the quantity q is defined as $q = E_1/\Gamma_e(1-E_1)$ with $E_1 = E_\gamma/(\gamma mc^2)$ being the scattered photon energy expressed in units of the initial electron energy. The functions $G(q,\Gamma_e)$ is the scattered photon distribution function and is plotted in Fig. (4.2). It can be seen from Fig. 4.2 that in the Klein-Nishina limit ($\Gamma_e \gg 1$) the peak of the distribution is at the high-energy end which means that in this limit the electron dominantly looses large portions of its energy in one Compton scattering. In the Thomson limit ($\Gamma_e \ll 1$) however, the distribution function favors the low energy part, which means that the electron only loses small portion of is energy.
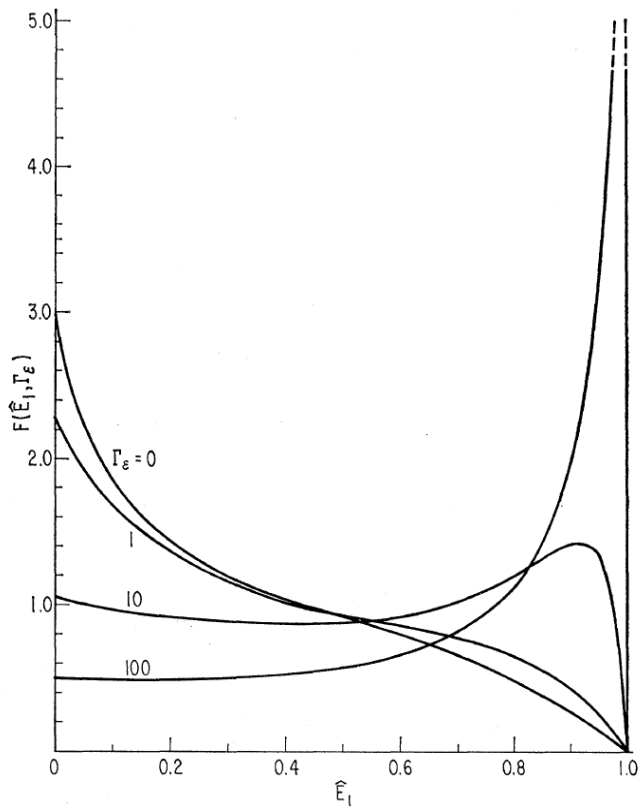
Figure 4.2: Scattered photon distribution function in the general case where $\hat{E}$ is the ratio of the scattered photon energy to its maximum value (Blumenthal and Gould 1970).

If the electron spectrum has the form of a power-law like $\frac{dN_e}{dE_e} \propto E_e^{-\Gamma}$ then the resulting γ-ray spectrum depending on the regime is:

Thomson regime:

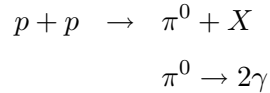$$\frac{dN_\gamma}{dE\gamma} \propto E_\gamma^{-(\Gamma+1)/2} \tag{4.11}$$

Klein-Nishina regime:

$$\frac{dN_\gamma}{dE\gamma} \propto E_\gamma^{-(\Gamma+1)} \tag{4.12}$$

4.3   Hadronic production mechanism

Relativistic protons and nuclei produce γ-rays during inelastic collisions with ambient gas (nucleons). In these collisions π^0 mesons are produced which decay into two γ photons:

$$p + p \quad \rightarrow \quad \pi^0 + X$$
$$\pi^0 \rightarrow 2\gamma$$

The p-p interaction is one of the two dominant γ-ray production mechanisms in the GeV to TeV energy range, the other being the already discussed inverse Compton upscattering of low energetic photons by high energetic electrons. Calculations show that in the galactic plane at energies above several hundreds MeV the π^0-decay γ-rays dominate over bremsstrahlung and IC γ-rays (see Aharonian & Atoyan 2000 (7). It is therefore believed that the diffuse galactic γ-radiation, together with the interstellar hydrogen column density, as obtained by radio data, contains important informations on the distribution of the cosmic rays' nuclear component. The emissivity is the so called source function of secondary particles and has the units of number of secondary particles produced per cubic centimeter per second per unit energy interval at position $\vec{r}$. It is given by the relation:

$$q_k(E_k, \vec{r}) = \int_{E_{\min}}^{E_{\max}} \frac{d\sigma_{i \rightarrow k}(E_k, E_i)}{dE_k} \left(\frac{c\rho(\vec{r})}{m} \right) \left(\frac{4\pi}{c} \phi(E_i, \vec{r}) \right) dE_i \qquad (4.13)$$

Where E_i is the energy of the incoming particles (e.g. primary cosmic rays) and E_k is the energy of the produced secondary particles (e.g. gamma rays). The primary flux of cosmic rays is defined by $\phi(E_i, \vec{r}) = \frac{dN_i}{dE_i dA dt d\Omega}$.

The emissivity $q_\gamma(E_\gamma)$ of γ-rays due to decay of π^0-mesons is defined by

$$q_\gamma(E_\gamma, \vec{r}) = 2 \int_{E_{\min}}^{\infty} \frac{q_\pi(E_\pi, \vec{r})}{\sqrt{E_\pi^2 - m_\pi^2 c^4}} dE_\pi \qquad (4.14)$$

with $E_{\min} = E_\gamma + m_\pi^2 c^4/(4E_\gamma)$ and $q_\pi(E_\pi, \vec{r})$ being the emissivity of secondary produced π^0 from inelastic proton-proton interactions.

To get the flux of γ-rays, the source function, which is averaged over the surface of sphere with radius r, needs to be integrated over the volume.

$$\frac{dN_\gamma}{dAdE_\gamma dt} = \int \frac{q_\gamma(E_\gamma, \vec{r})}{4\pi r^2} d^3r \tag{4.15}$$

$$\Rightarrow \phi_\gamma(E_\gamma) = \frac{dN_\gamma}{dAdE_\gamma dtd\Omega} = \int_0^{r_{\max}} \frac{q_\gamma(E_\gamma, \vec{r})}{4\pi} dr \tag{4.16}$$

Under the assumption of homogenously distributed cosmic rays $\phi(E, \vec{r}) = \phi(E)$ in the galactic disk one finds that the γ-ray flux in a given direction is proportional to the gas column density. This follows from

$$\phi_\gamma(E_\gamma) = \frac{1}{4\pi} \int_0^{r_{\max}} q_\gamma(E_\gamma) dr \tag{4.17}$$

$$= \underbrace{\int_0^{r_{\max}} dr \frac{\rho(\vec{r})}{m}}_{\text{column density}} \int_{E_{\min}}^{E_{\max}} \frac{d\sigma(E_\gamma, E)}{dE_\gamma} \phi(E) dE \tag{4.18}$$

Thus, it is expected that the spatial distribution of γ-rays mirrors the spatial distribution of the gas column density.

4.3.1 p-p interaction model

This subsection is dedicated to the parametric model for proton-proton interactions used for my calculations developed by Kamae et al. (2006)(42) and Karlsson and Kamae (2008)(43). This model is implemented in the cparamlib[1] c library and can be used to calculate inclusive cross sections for all stable secondaries (gamma rays, electrons, positrons, etc.).

Although many calculations have assumed an energy independent p-p inelastic cross section of about 24 mbarn for $T_p \gg 10$ GeV, recent observations show however a logarithmic increase with the incident proton energy. Furthermore, diffractive interaction has been neglected, which is an important component of the p-p interaction (Kamae et al. 2005(41)). This is a class of interaction, where the projectile proton and/or the target proton transition to excited states. The following figures illustrate the cross section for the two different approaches. Figure 4.3 is taken from Kamae et al. 2005(41) where they describe the two models they used. Model A takes non-diffractive and diffractive

---

[1]http://www.slac.stanford.edu/~niklas/cparamlib/

processes into account, whereas model B only incorporates the non-diffractive process. However, model A does not model p-p interaction accurately near the pion production threshold. Thus, in order to improve the prediction of gamma rays produced near the pion production threshold, two baryon resonance-excitation components have been added to model A, as described by Kamae et al. (2006)(42). To parameterize the inclusive cross section, they first extracted the secondary particle spectra for events generated for monoenergetic protons and then fitted these spectra with a parameterized function. They did this separately for the non-diffractive, diffractive and resonance-excitation process. For the non-diffractive process for example the cross section is parameterized by the following function:

$$\frac{\Delta\sigma_{\mathrm{ND}}(\mathrm{E_{sec}})}{\Delta\log(\mathrm{E_{sec}})} = F_{\mathrm{ND}}(x)F_{\mathrm{ND,kl}}(x) \tag{4.19}$$

where $\mathrm{E_{sec}}$ is the energy of the secondary particle and the quantity $\mathrm{x} = \log(\mathrm{E_{sec}})$. Furthermore, F_{ND} is the formula representing the non-diffractive cross section and $F_{\mathrm{ND,kl}}$ approximately enforces the energy-momentum conservation. They are described by:

$$
\begin{aligned}
F_{\mathrm{ND}}(x) =\ & a_0 \exp(-a_1(x - a_3 + a_2(x - a_3)^2)^2) + \\
& a_4 \exp(-a_5(x - a_8 + a_6(x - a_8)^2 + a_7(x - a_8)^3)^2) \tag{4.20}
\end{aligned}
$$

and

$$F_{\mathrm{ND,kl}}(x) = \frac{1}{(\exp\left(W_{\mathrm{ND,l}}(L_{\min} - x)\right) + 1)} \times \frac{1}{(\exp\left(W_{\mathrm{ND,h}}(x - L_{\max})\right) + 1)} \tag{4.21}$$

where $L_{\min}$ and $L_{\max}$ are the assumed lower and upper kinematic limits respectively, while $W_{\mathrm{ND,l}}$ and $W_{\mathrm{ND,h}}$ are the widths of the kinematic cut-offs.
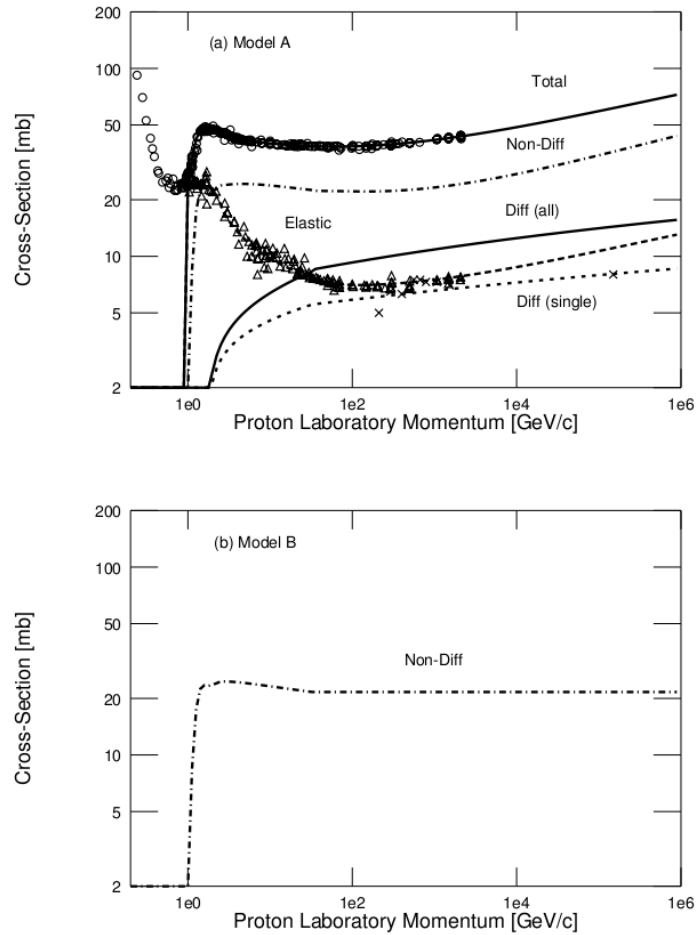
Figure 4.3: Top figure shows the p-p cross-section model A: Curves are for the total (upper solid), non-diffractive inelastic (dot-dashed), elastic (dashed), all diffractive (lower solid), and single diffractive (dotted) processes. The lower figure shows Model B where only non-diffractive inelastic processes are considered. Data points from Hagiwara et al. (2002) are for the total (circles), elastic (triangles), and single diffraction (crosses). Taken from Kamae et al. 2005(41)

The simulated and parameterized gamma ray inclusive cross sections are shown in the Fig. (4.4) below.
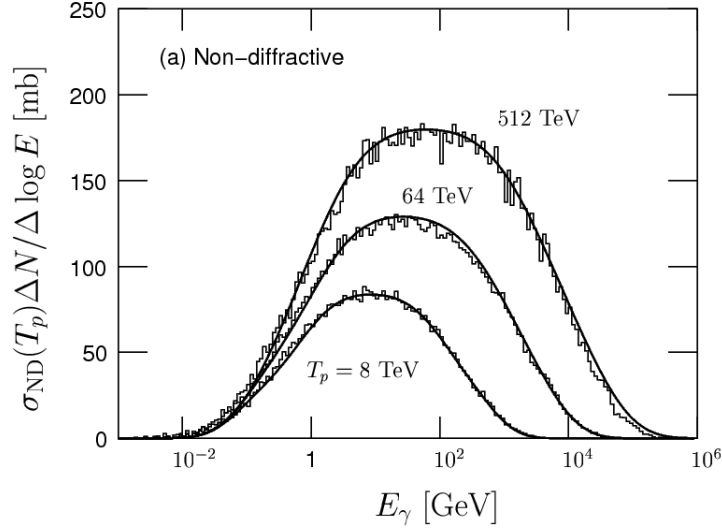
Figure 4.4: The figure taken from Kamae et al. (2006)(42) shows the simulated cross sections using Monte-Carlo event generation for monoenergetic protons, based on Model A (histograms). And the parameterized (solid line) cross sections for non-diffractive and diffractive processes for 3 different proton kinetic energies.

Using these expressions, the total gamma ray spectrum is then a sum over the non-diffractive, diffractive and resonance-excitation contributions. For a continuous energy distribution of the protons one has to integrate over the total gamma ray spectra of monoenergetic protons with the appropriate spectral weight. The emissivity of π^0 particles assuming a δ-functional approximation for the cross-section $\sigma(E_\pi, E_p)$ is

$$
\begin{aligned}
q_\pi(E_\pi) &= 4\pi\, n \int \delta(E_\pi - f_\pi E_{\text{kin}})\sigma_{\text{pp}}(E_p)J_p(E_p)\mathrm{d}E_p \\
&= \frac{4\pi\, n}{f_\pi}\sigma_{\text{pp}}\left(m_{\text{p}}c^2 + \frac{E_\pi}{f_\pi}\right) J_p\left(m_{\text{p}}c^2 + \frac{E_\pi}{f_\pi}\right)
\end{aligned}
\tag{4.22}
$$

with f_π being the mean fraction of the kinetic energy $E_{\text{kin}} = E_{\text{p}} - m_{\text{p}}c^2$ of the proton transferred to the secondary π^0 particle per collision and n being the gas number density in units of cm^{-3}. The quantity $J_{\text{p}}(E_{\text{p}})$ is the primary proton flux spectrum. At sufficiently high energies, all mass scales can be neglected compared to the energy.

In this limit and assuming a power law spectrum for the protons it follows (see Aharonian & Atoyan 1996(6)):

$$q(E_\gamma) = 4\pi\sigma_{tot} \cdot J_p(E_\gamma) \cdot \frac{2Z^{(\alpha)}}{\alpha}\eta_A \tag{4.23}$$

where the quantities $Z^{(\alpha)}$ are the spectrum weighting moments, α is the spectral index of the power law for the protons $J_\mathrm{p}(E_\gamma) = K_p E^{-\alpha}$ and η_A accounts for nuclei in the CR proton flux. The following plot shows the gamma ray spectra produced by protons with a power law spectrum for two different spectral indices:
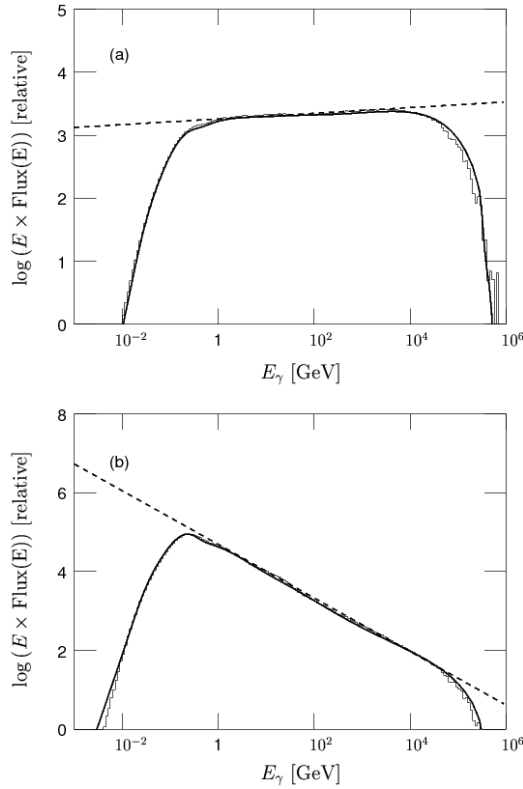
Figure 4.5: Gamma ray spectra produced by protons with a power law spectrum and a cutoff at $\mathrm{T}_P = 512$ TeV as well as two spectral indices: (a) index $= 2$ and (b) index $= 2.7$. The dashed line corresponds to an index of (a) 1.95 and (b) 2.68. Taken from Kamae et al. (2006)(42)

Chapter 5

Sources of galactic CR protons and electrons

In this chapter the last quantity for calculation of the γ-ray emissivity is described, namely the particle flux of CR for different methods of injection from sources into the ISM.

5.1 Proton and electron flux for different injection mechanisms

Relativistic particles, which are believed to be accelerated in shocks within supernova remnants (SNRs), can escape them and enter the ISM. The energy spectrum of these CR particles at a given time and distance from their sources depend on:

- the time history of acceleration of the source

- the injection spectrum

- the energy loss rate

- the character of propagation

The standard diffusion approximation, which neglects convection and assumes a spherically symmetric propagation of cosmic rays is given by:

$$\frac{\partial f}{\partial t} = \frac{D}{R^2}\frac{\partial}{\partial R}R^2\frac{\partial f}{\partial R} + \frac{\partial}{\partial \gamma}(Pf) + Q \tag{5.1}$$

where $\gamma = \frac{E}{m_e c^2}$ and $f(R, t, \gamma)$ is the energy distribution function of particles at a given time t and distance R from the source. The energy dependent diffusion coefficient is described by $D = D(\gamma)$, where a homogeneous medium is assumed and the diffusion does therefore not depend on R. Furthermore, $P(\gamma) = -\frac{d\gamma}{dt}$ is the continuous energy loss rate. A general solution can be found for a δ-function-type initial distribution of particles both in space and time like $Q(E, R, t) = N_0 f_{\text{inj}}(E)\delta(R)\delta(t)$ for an arbitrary injection spectrum $Q(\gamma)$ (see Atoyan et al. 1995)(18):

$$f(R, t, \gamma) = \frac{Q(\gamma_t)P(\gamma_t)}{\pi^{3/2}P(\gamma)R_{\text{diff}}^3}\exp(-\frac{R^2}{R_{\text{diff}}^2}) \tag{5.2}$$

with $\gamma_t \equiv g^{-1}(T - t)$, where $g^{-1}(T)$ is the inverse function of $g(\gamma)$ defined by:

$$T = \int_\gamma^{\gamma_\star} \frac{d\gamma_1}{P(\gamma_1)} = g(\gamma) \tag{5.3}$$

which corresponds to the time required for a particle to cool down from some energy $\gamma_\star$ to the energy γ. The quantity R_{diff} is the effective diffusion radius up to which the relativistic particles with energy γ propagate during the time t after their injection from the source. The differential flux is then defined by:

$$J(E, R, t) = \frac{c}{4\pi}f(E, R, t) \text{ in units of } [(\text{GeV cm}^2 \text{ s sr})^{-1}] \tag{5.4}$$

5.1.1 Proton flux from impulsive sources (Burst-like injection)

A source can be called an impulsive source, when the acceleration timescale of the bulk of relativistic protons is significantly smaller than the age of the accelerator. Therefore, SNRs can be considered impulsive sources only if the age of the SNR is larger then 10^4 - 10^5 yr, since the typical duration of particle acceleration in the so-called Sedov phase is 10^3 - 10^4 yr. The energy losses of protons diffusing through the gas component of the interstellar medium are due to ionization and nuclear interactions, but at energies above 1 GeV the nuclear energy losses dominate the ionization losses. Assuming a power-law as injection spectrum of an impulsive source in the form of $Q(E, t) = N_0 E^{-\Gamma}\delta(t)$ and a power-law diffusion coefficient like $D(E) \propto E^\delta$, the general solution (5.2) reduces to (see Aharonian & Atoyan 1996(6)):

$$f(E, R, t) \approx \frac{N_0 E^{-\Gamma}}{\pi^{3/2}R_{\text{diff}}^3}\exp\left(-\frac{(\Gamma - 1)t}{\tau_{\text{pp}}} - \frac{R^2}{R_{\text{diff}}^2}\right) \tag{5.5}$$

where

$$R_{\text{diff}} \equiv R_{\text{diff}}(E, t) = 2\sqrt{D(E)t\frac{\exp(t\delta/\tau_{\text{pp}}) - 1}{t\delta/\tau_{pp}}} \tag{5.6}$$

is the diffusion radius and describes the radius of the sphere up to which particles of energy E propagate during the time t after injection into the ISM. Furthermore τ_{pp} is the lifetime of a proton due to nuclear energy losses and is roughly given by: $\tau_{pp} \approx 6 \cdot 10^7 (\text{n/cm}^{-3})^{-1}\text{yr}$. As one can see this lifetime can significantly exceed the typical timescales of activity of accelerators for number densities $n \leq 1\,\text{cm}^{-3}$. While the energy-independent diffusion does not change the form of the primary spectrum, energy-dependent diffusion does. The modification of the primary particle spectrum is mainly defined by the parameter $g(E, R, t) = \xi^3 \exp(-\xi^2)$, where $\xi \equiv \xi(E, R, t) = R/R_{\text{diff}}$. The maximum flux of protons at a given distance from the source is reached at times $t_{\max}(E) = r^2/(6D(E))$ after their injection. At $t \ll t_{\max}(E)$ the protons did not have enough time to reach the observer yet, while at $t \gg t_{\max}(E)$ the flux decreases due to spherical expansion as $R_{\text{diff}}^{-3} \propto t^{-3/2}$. This is the reason that at sufficiently high energies, when the maximum flux has already passed the observer, the spectrum of injection changes proportional to $E^{-(3/2)\delta}$, since $\xi(E, R, t) \propto R_{\text{diff}}^{-3} \propto D(E)^{-3/2}$. In short the index of the power-law spectrum of particles changes with regard to the injection spectrum at sufficiently high energies to (Atoyan et al. 1995 (18)):

$$\Gamma' = \Gamma + \frac{3}{2}\delta \tag{5.7}$$

5. SOURCES OF GALACTIC CR PROTONS AND ELECTRONS

5.1.2 Proton flux spectrum for a SNR

Although protons released from SNRs can be described by a burst-like injection mechanism, there is a model from Ptuskin & Zirakashvili (2005)(50), that describes particle injection from SNRs more realistically. The idea is that PeV protons can only be accelerated during a relatively short period of the SNR evolution, namely at the beginning of the Sedov phase, when the shock velocity is high enough to allow a sufficiently high acceleration rate. When the SNR enters the Sedov phase, the shock gradually slows down and correspondingly the maximum energy of the particles that can be confined within the SNR decreases. This determines the escape of the most energetic particles from the SNR. When the remnant enters the Sedov phase, the low-energy cutoff in the spectrum of the protons gradually moves to lower energies, while the highest energy particles leave the remnant (see Fig. 5.1).

Assuming that the maximum momentum of accelerated particles inside the SNR scales like a power-law in time as $p_{\mathrm{max}}(t) \propto t^{-\beta}$ the distribution function of escaping CR at the time t and distance R of the SNR, for energies $E \geq c \cdot p_{\mathrm{max}}(t)$ is given by (Gabici, Aharonian & Casanova 2009(35)):

$$f(E, R, t) = \frac{\eta E_{\mathrm{SN}}}{\pi^{3/2}\log(\mathrm{E_{max}/E_{min}})} \cdot \frac{e^{-\left(\frac{R}{R_{\mathrm{diff}}}\right)^2}}{R_{\mathrm{diff}}^3}E^{-2} \tag{5.8}$$

with an initial CR injection power-law index of 2. The energy E_{SN} is the total supernova explosion energy, η the fraction of this energy that goes into accelerating the CR particles and E_{max} and E_{min} are the maximum and minimum energy a CR particle can reach during the Sedov phase. The diffusion distance is defined by:

$$R_{\mathrm{diff}}(E) = \sqrt{4D(E)(t - \chi(E))} \tag{5.9}$$

where

$$\chi(E) = t_{\mathrm{Sedov}}\left(\frac{E}{E_{\mathrm{max}}}\right)^{-1/\beta} \tag{5.10}$$

As said above, particles with different energies escape into the ISM at different times, which is represented by $\chi(E)$. The particles with the maximum energy are therefore released first at the early times of the Sedov phase. Note however, that this solution does not contain any energy losses and therefore is only valid in places with low gas

densities. The following Fig. (5.1) shows this CR spectrum of injected particles at a distance of 50 pc from a SNR. It can be seen that for larger times the cut-off on the lower energy side moves to lower energies, which means that the lower energetic particles are injected in the ISM at later times. The cut-off at high energies is assumed to be at around 5 PeV.
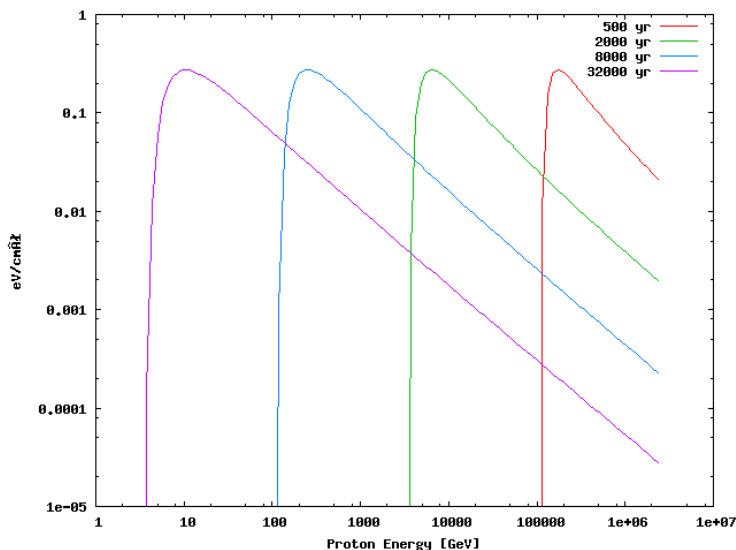

Figure 5.1: This plot shows the spectrum of CRs at a distance of 50 pc from a SNR. The different curves are for different times after the supernova explosion. $D_{10} = 10^{28}$ cm^2/s, $E_\star$ = 10 GeV, $E_{SN} = 10^{51}$ erg, $\delta = 0.5$, $\eta = 0.3$, $\beta = 2.794$ and $t_{Sedov} = 200$ yr.

5.1.3 Proton flux from continuous sources

In the case of a continuous accelerator assuming injection with a constant rate during the time $0 \le t' \le t$ and substituting $N_0 \to Q_0 dt'$ in Eq. (5.5) as well as integrating over dt' one gets:

$$f(E, R, t) = \frac{Q_0 E^{-\Gamma}}{4\pi D(E)R} \text{erfc}\left(\frac{R}{R_{\text{diff}}(E, t)}\right) \tag{5.11}$$

For a power-law diffusion coefficient, the spectral index of continuously accelerated particles is given by:

$$\Gamma' = \Gamma + \delta \tag{5.12}$$

which is smaller by $\delta/2$ than in the case of an impulsive source.

5.1.4 Electron flux from impulsive sources (Burst-like injection)

Since electrons are severly hindered in their range by energy losses the contribution from sources are dominated by particles produced in the vicinity of the observer. The following Fig. (5.2) shows the mean interaction length, which is the mean free path between two subsequent interactions and the energy-loss distance $E/(dE/dx)$. It can
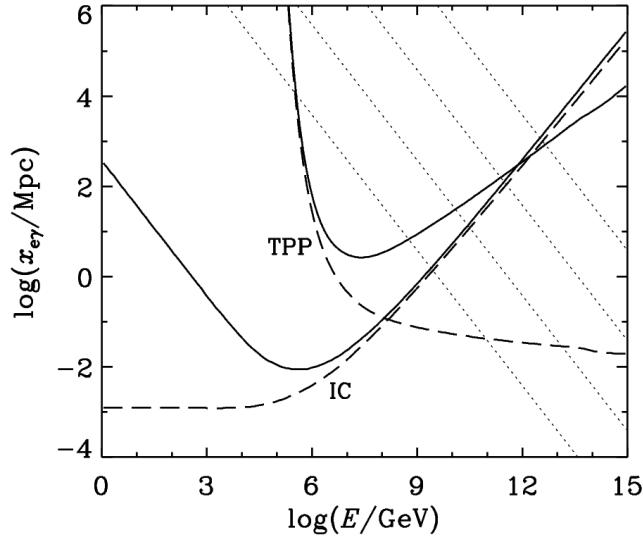
Figure 5.2: This plot shows the mean interaction length (dashed line) and energy-loss distance (solid line), for inverse-Compton scattering (IC) on the microwave background and electron-photon triplet pair production (TPP). The energy-loss distance for synchrotron radiation is also shown (dotted lines) for intergalactic magnetic fields of 10^{-9} (bottom), 10^{-10}, 10^{-11}, and 10^{-12} gauss (top). Taken from Protheroe (1996)(49)

be seen that at energies up to ~ 1 PeV the energy-loss distance of electrons reduces as E^{-1}, which corresponds to the Thomson limit in which the energy loss rate is $-dE/dt \propto E^2$. Additionally, the mean interaction length has a constant value of about 1 kpc, since in the Thomson regime the cross-section is constant. At energies above approximately 1 PeV the mean interaction length and the energy-loss distance increase since the cross-section of IC scattering decreases in the Klein-Nishina regime.

The energy loss rate of relativistic electrons can be described by:

$$P(\gamma) = p_0 + p_1\gamma + p_2\gamma^2 \ [\text{s}^{-1}] \tag{5.13}$$

It accounts for ionization and bremsstrahlung losses of electrons in the interstellar gas

with the quantities p_0 and p_1 respectively. It also accounts for synchrotron and inverse Compton losses with $p_2 \simeq 5.2 \cdot 10^{-20} \omega_0$ s^{-1}.

The quantity $\omega_0 = \omega_B + \omega_{\mathrm{CMB}} + \omega_{\mathrm{opt}}$ is the energy density of the associated radiation fields, namely CMB ($\omega_{\mathrm{CMB}} = 0.25$ eV/cm^3) and optical-IR ($\omega_{\mathrm{opt}} \simeq 0.5$ eV/cm^3) as well as the magnetic field ($\omega_B = 0.6$ eV/cm^3 for B $= 5\mu$G). Above several GeV the Compton and synchrotron losses dominate over the bremsstrahlung and ionization losses. Also for timescales t $\leq 10^7$ yr only those two mechanisms are important. So in this energy regime it is justified to write $P(\gamma) \approx p_2 \gamma^2$ (Atoyan et al. 1995 (18)). The general solution (5.2) for electrons diffusing in the ISM reduces to:

$$f(R, t, E) = \frac{N_0 E^{-\Gamma}}{\pi^{3/2} R^3} (1 - btE)^{\Gamma - 2} \left(\frac{R}{R_{\mathrm{diff}}}\right)^3 e^{-(R/R_{\mathrm{diff}})} \tag{5.14}$$

where $E < E_{\mathrm{cut}}$ with $E_{\mathrm{cut}} = m_e/(p_2 t)$ otherwise $f = 0$ and $b = p_2/m_e$. The diffusion radius is defined as:

$$R_{\mathrm{diff}}(E, t) = 2\sqrt{D(E)t\frac{1 - (1 - E/E_{\mathrm{cut}})^{1-\delta}}{(1 - \delta)E/E_{\mathrm{cut}}}} \tag{5.15}$$

Here a power-law was assumed as $Q(E) = N_0 E^{-\Gamma}$ and a diffusion coefficient like

$$D(E) = D_{10}(E/E_\star)^\delta \tag{5.16}$$

where D_{10} is the value of the diffusion coefficient at the energy $E_\star$. If $E \ll E_{\mathrm{cut}}$ the diffusion radius becomes $R_{\mathrm{diff}} \simeq 2\sqrt{D(E)t}$ and eq. (5.14) reduces to an expression for the electron energy spectrum without energy losses. The energy spectra of electrons at different times t after their injection into the ISM from a source at a distance of 100 pc is shown in Fig. (5.3). From this it can be seen that at higher energies the spectra are essentially flat (since it was multiplied with the electron energy cube), which is due to the fact that for burst-like injection the initial injection spectral index changes from a $\Gamma = 2.2$ to a $\Gamma' = 2.2 + 3/2 \cdot 0.6 = 3.1$ (see eq. (5.7)). Also the cut-off of these spectra moves to lower energies for larger times because the maximal flux of electrons has already passed by the observer. For the lower energetic part of the spectrum it can be seen that electrons with lower energies did not have time to reach the observer yet for larger times of injection.
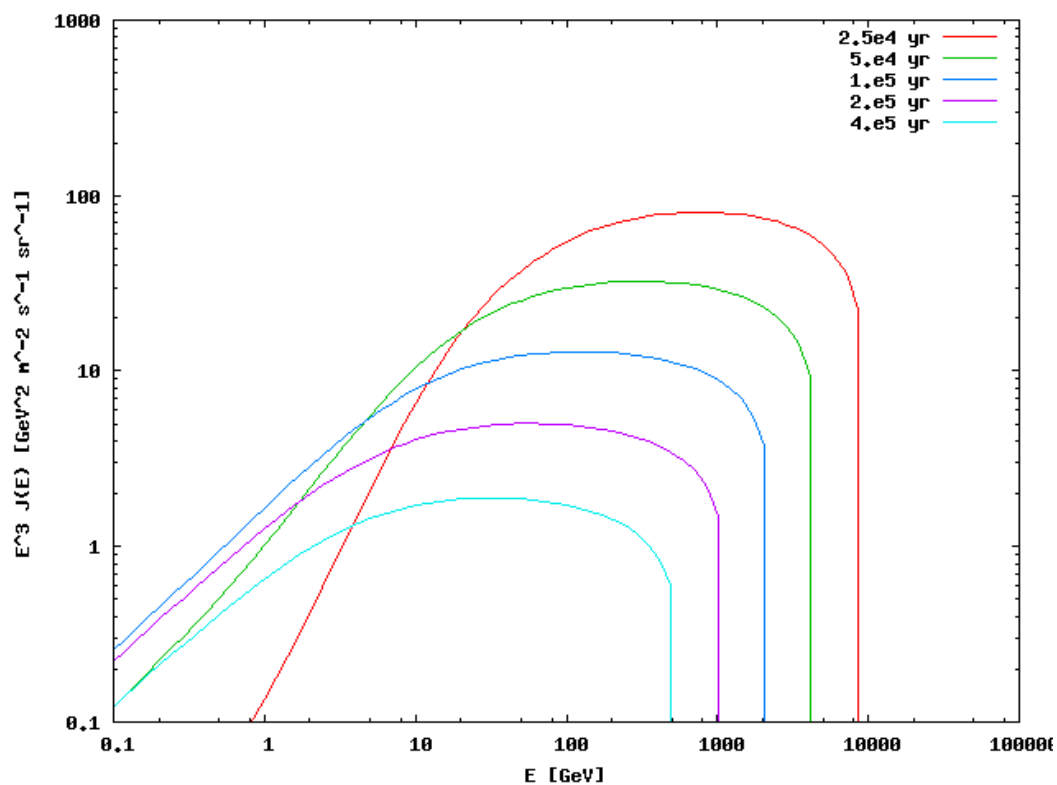
Figure 5.3: Electron spectrum assuming burst-like injection with a energy output of 10^{48} erg, a spectral index of $\Gamma = 2.2$, $D_{10} = 10^{28}$ cm^2/s and $E_\star = 3$ GeV. The different solid lines correspond to the different times t after the electrons have been injected into the ISM. The diffusion power-law index is $\delta = 0.6$

5.1.5   Electron flux from continuous sources

Assuming injection with a constant rate during the time $0 \leq t' \leq t$ and substituting $N_0 \rightarrow Q_0 dt'$ in Eq. (5.14) and integrating over dt' one gets:

$$f(R, t, E) = \frac{Q_0 E^{-\Gamma}}{4\pi D(E)R} \text{erfc} \left(\frac{R}{2\sqrt{D(E)t_E}} \right) \tag{5.17}$$

where $t_E = \min \left(t, \frac{m_e c^2}{p_2 E} \right)$. The energy spectra of electrons at different times t after their injection into the ISM and at a distance of 100 pc from a continuous source is shown in Fig. (5.4). The cut-off at high energies disappears due to the fact that new electrons are continuously injected. At low energies one can see the same behaviour as in the case of burst-like injection, which means that the low energetic particles need a longer time to reach the observer, than their high-energetic counterparts.
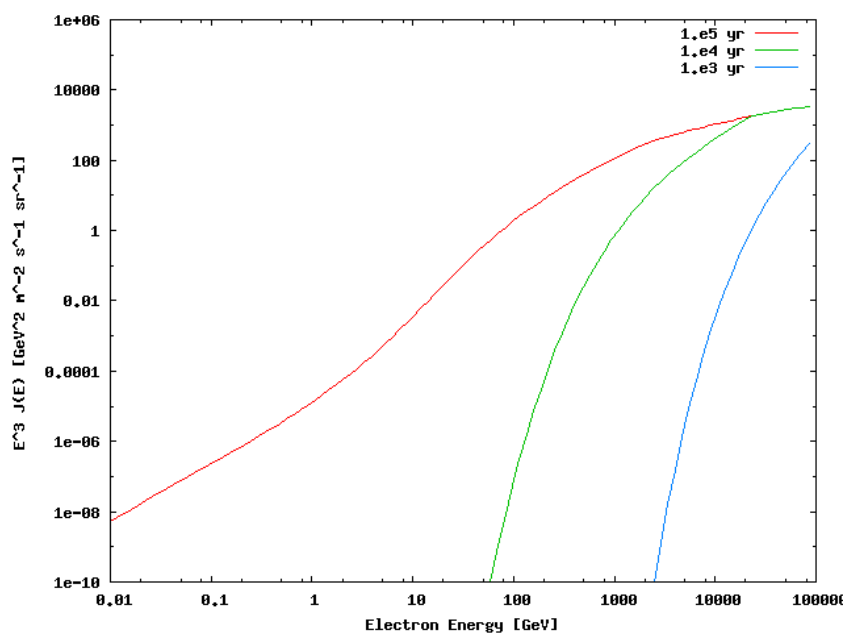
Figure 5.4: Electron spectrum assuming continuous injection with a luminosity of 10^{37} erg/s, a spectral index of $\Gamma = 2$, $D_{10} = 10^{28}$ cm^2/s and $E_\star = 3$ GeV. The different solid lines correspond to the different times t after the electrons have been injected into the ISM. The diffusion power-law index is $\delta = 0.6$

5.2 γ-ray emission from CR proton and electron sources

As a reminder, the source function (emissivity) of secondary particles in this case photons, produced per cubic centimeter per second per unit energy interval at position $\vec{r}$ is given by the relation (see eq. (4.13)):

$$q_k(E_k, \vec{r}) = \int_{E_{\min}}^{E_{\max}} \frac{d\sigma_{i \to k}(E_k, E_i)}{dE_k} \left(\frac{c\rho(\vec{r})}{m} \right) \left(\frac{4\pi}{c} \phi(E_i, \vec{r}) \right) dE_i$$

For inverse Compton scattering of electrons on radiation fields, the source function is an integral not only over the incoming electron energy but also over the energy range of the photon field,

$$q_\gamma(E_\gamma) = \int_{E_{\mathrm{thr}}}^{E_{\max}} dE_e \int_{\epsilon_{\min}}^{\epsilon_{\max}} d\epsilon \frac{d\sigma(E_\gamma, E_e)}{dE_\gamma} \, \rho(\epsilon) \, 4\pi\phi(E_e) \tag{5.18}$$

where the cross section for this process is defined by (4.9) and E_{thr} is the minimum electron energy an electron must have to scatter a photon of energy ϵ up to one with energy E_γ. It is defined by (see Schlickeiser 2002(51))

$$E_{\mathrm{thr}} = \frac{1}{2} E_\gamma \left[1 + \left(1 + \frac{m^2 c^4}{\epsilon E_\gamma} \right)^{1/2} \right] \tag{5.19}$$

For Bremsstrahlung produced by electrons deflected in electric fields, the source function is defined as

$$q_\gamma(E_\gamma) = \sum_i \int_{E_{\mathrm{thr}}}^{E_{\max}} dE_e \frac{d\sigma_i(E_\gamma, E_e)}{dE_\gamma} \, n_i(\vec{r}) \, 4\pi\phi(E_e) \tag{5.20}$$

where the index i denotes the species of the present gas, which in this case is atomic and molecular hydrogen with $n_i(\vec{r})$ being the number density of these two. The threshold energy for this process is defined by $E_{\mathrm{thr}} = \max(E_\gamma, E_1)$, with E_1 being the low energy cut-off in the relativistic electron distribution. The cross section for this process is given by (4.2).

The next few pages will discuss the γ-ray emission for different scenarios, where eq. (5.18) and eq. (4.16) have been numerically integrated using a simple routine.

The first scenario is a calculation of the IC flux of an expanding cloud of electrons which are continuously injected by a single source into the ISM, e.g. a single pulsar. Those electrons scatter on the CMB radiation field and produce γ-rays due to IC-scattering. For this scenario the following integration was performed:

$$\frac{dN_\gamma}{dE_\gamma dt} = \int dV \int d\epsilon \int dE_e \frac{d\sigma}{dE_\gamma} \cdot \rho_{\mathrm{CMB}}(\epsilon) \cdot 4\pi f(R, t, E_e) \qquad (5.21)$$

Where f(R,t,E_e) is defined by (5.17). The used parameters are described in the caption of Fig. (5.5).
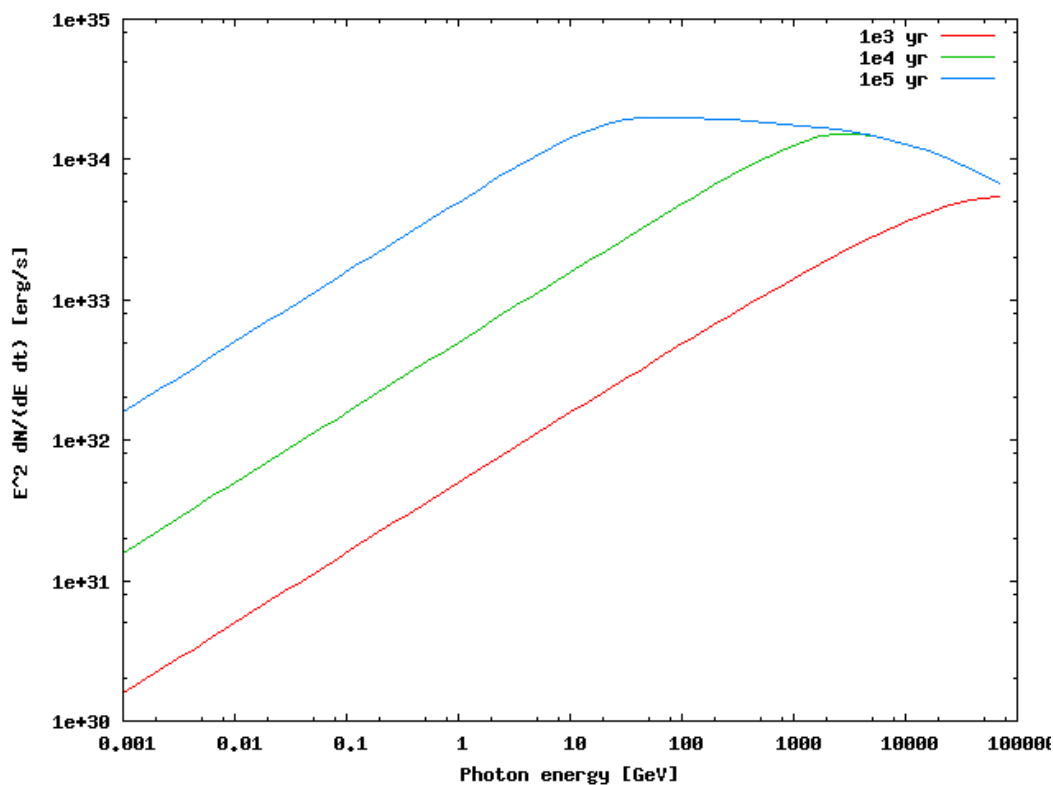
Figure 5.5: γ-ray flux of an expanding cloud of relativistic electrons at 3 different epochs. The assumed parameters are: energy output rate of 10^{37} erg/s, spectral index of $\Gamma = 2$, $D_{10} = 10^{28}$ cm^2/s and $\delta = 0.6$

5. SOURCES OF GALACTIC CR PROTONS AND ELECTRONS

The spectral index in the thomson regime is determined by (see also eq. (4.11)):

$$q(E_\gamma) \propto E_\gamma^{-(\Gamma+1)/2}$$

Note that by integrating the fluxes over all angles from the source, the spectrum depends only on the initial spectrum of electrons, thus diffusion does not matter. For the assumed spectral index of 2 this yields a proportionality of $E_\gamma^{-1.5}$ which is in good agreement with the presented calculation.

The second scenario is basically the same as the first but instead of a continuous injecting source an impulsive source was used. This means an integration of the same formula (5.21) but with $f(R, t, E_e)$ being described by (5.14). In Fig. (5.6) it can be
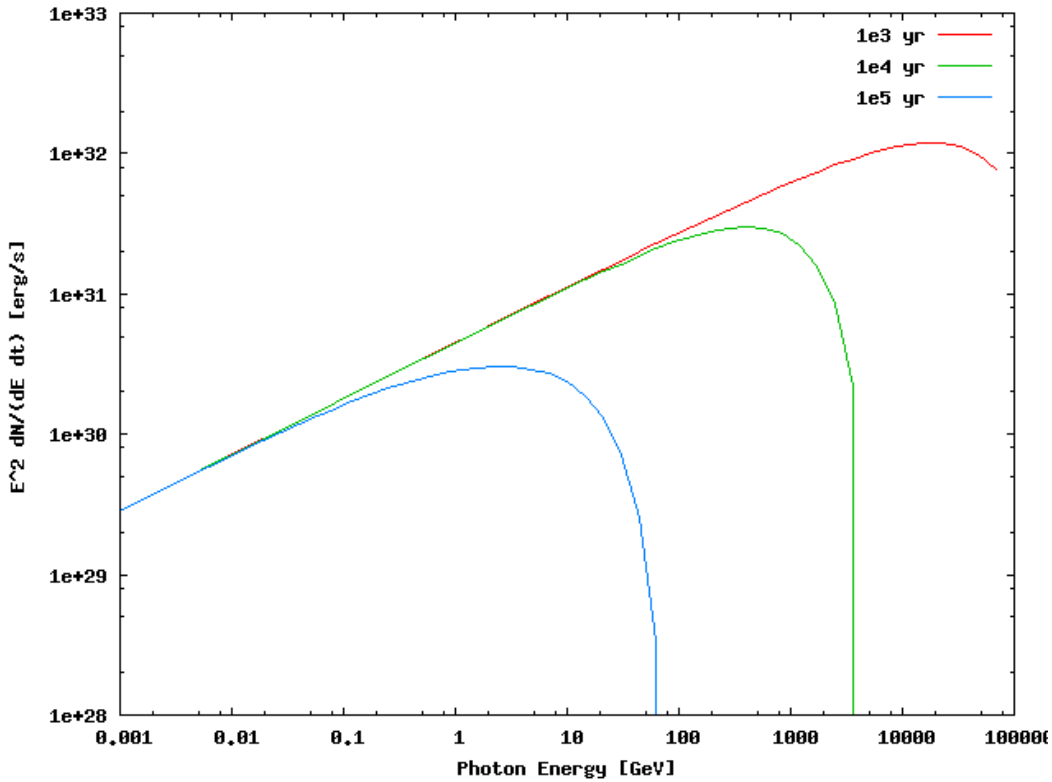
Figure 5.6: γ-ray flux of an expanding cloud of relativistic electrons at 3 different epochs. The assumed parameters are: energy output of 10^{48} erg, spectral index of $\Gamma = 2.2$, $D_{10} = 10^{28}$ cm^2/s and $\delta = 0.6$

seen, that the cut-off at high energies in the electron spectrum leads to a cut-off at high energies in the γ-ray spectrum as well. For the assumed spectral index of 2.2 this

yields the predicted proportionality of $E_\gamma^{-1.6}$.

The following scenario illustrates that the character of diffusion of electrons has a strong impact on the angular distribution of γ-rays. For that, the IC γ-ray fluxes that are expected within different detection angles from a source, are calculated in the following way:

$$\frac{dN_\gamma}{dE_\gamma dt dA} = \int d\Omega \int dl \int d\epsilon \int dE_e \frac{d\sigma}{dE_\gamma} \cdot \rho_{CMB}(\epsilon) \cdot f(l, t, E_e) \qquad (5.22)$$

This can be rewritten as:

$$\frac{dN_\gamma}{dE_\gamma dt dA} = \int d\Omega \int dl \; q_\gamma(E_\gamma, l) \qquad (5.23)$$

The integration over the solid angle can be expressed in terms of the projected radius $d\Omega = 2\pi b \, db/D_A^2$, where D_A is the angular distance to the source. With $l = \sqrt{r^2 - b^2}$ and $dl/dr = r/\sqrt{r^2 - b^2}$ assuming spherical symmetry one obtains:

$$\frac{dN_\gamma}{dE_\gamma dt dA} = \frac{2\pi}{D_A^2} \int_0^{b_{\max}} db \, b \int_b^\infty dr \; \frac{r}{\sqrt{r^2 - b^2}} \cdot q_\gamma(E_\gamma, r) \qquad (5.24)$$

The geometrics are illustrated in Fig. (5.7).
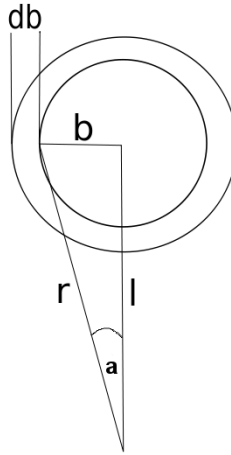
Figure 5.7: This plot roughly shows the geometry of the integration over the distance l and the solid angle Ω.

The Fig. (5.8) shows the IC γ-ray fluxes expected within different detection angles as obtained by eq. (5.24). It should be mentioned that below 1 GeV the contribution
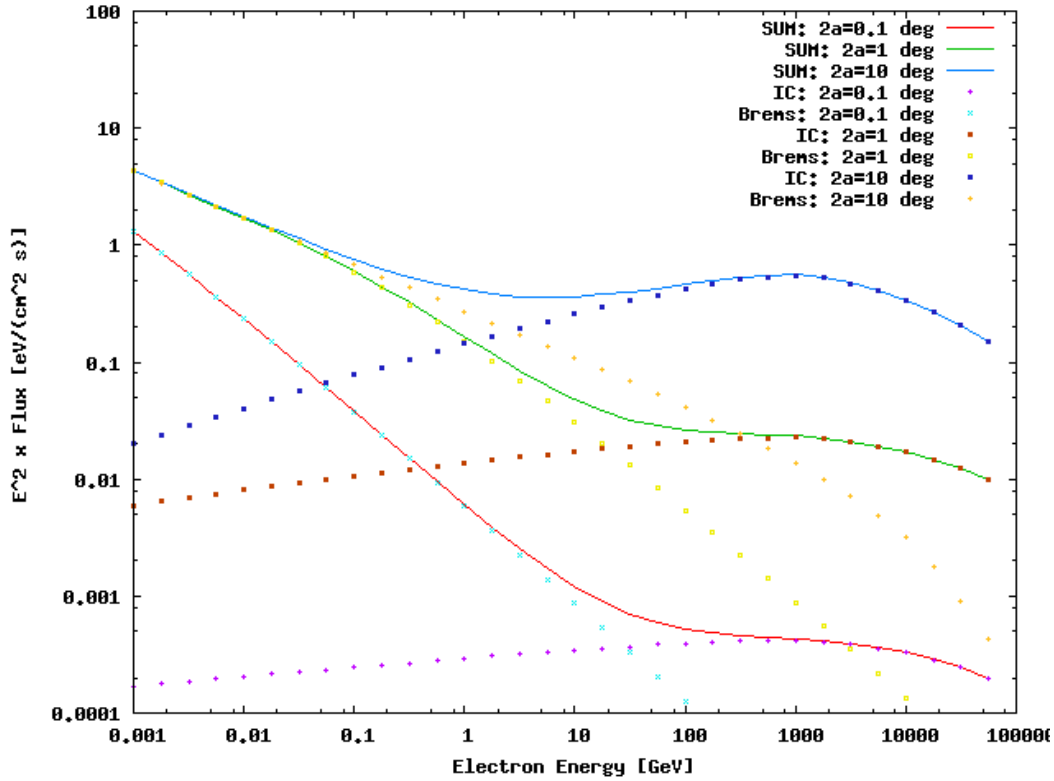
Figure 5.8: IC γ-ray fluxes expected within different detection angles from a source located at a distance of 0.5 kpc. The assumed parameters are: energy output rate of $3.5 \cdot 10^{36}$ erg/s, spectral index of $\Gamma = 2.4$, $D(E) = D_{10}(E/10\text{GeV})^{-\delta}$ with $D_{10} = 10^{27}$ cm^2/s and $\delta = 0.5$. Contributions from Bremsstrahlung and Inverse Compton are shown separately in dots.

from bremsstrahlung dominates the contribution from inverse Compton. For the 3 different detection angles of $2a = 0.1°$, $1°$ and $10°$ one can see that the fluxes at higher energies strongly differ. This demonstrates that diffusion has a strong impact on the angular distribution of radiation and thus on the visibility of γ-ray fluxes.

The last scenario is the interaction of protons injected into the ISM using the SNR model (see seq. 5.1.2), with a molecular cloud at a distance of 50 and 100 pc respectively. The proton spectrum for 50 pc has already been shown in Fig. (5.1). Since the γ-ray emissivity is defined in (4.23) as the emissivity in units of number of photons per second

per hydrogen atom per unit of energy, it follows from eq. (4.16) (see also Aharonian et al. 1996 (6))

$$J_\gamma = \frac{dN_\gamma}{dA dE_\gamma dt d\Omega} = \frac{1}{4\pi d^2} \cdot \int_{V_0} q_\gamma(E_\gamma) \cdot n(\vec{r}) d^3 r \qquad (5.25)$$

where $n(\vec{r})$ is the gas number density inside the molecular cloud, V_0 is the volume of the cloud and d is the distance of the cloud to the earth. Assuming that the γ-ray emissivity is the same throughout the cloud the above equation reduces to

$$J_\gamma = \frac{M_{\mathrm{MC}}}{m_p} \frac{q_\gamma(E_\gamma)}{4\pi d^2} \qquad (5.26)$$

with M_{MC} being the total mass of the molecular cloud and m_p the mass of the proton. The following Fig. (5.9) and Fig. (5.10) illustrate the γ-ray spectrum of a molecular cloud with a mass of 10^5 solar masses at a distance of 50 and 100 pc away from a SNR source.
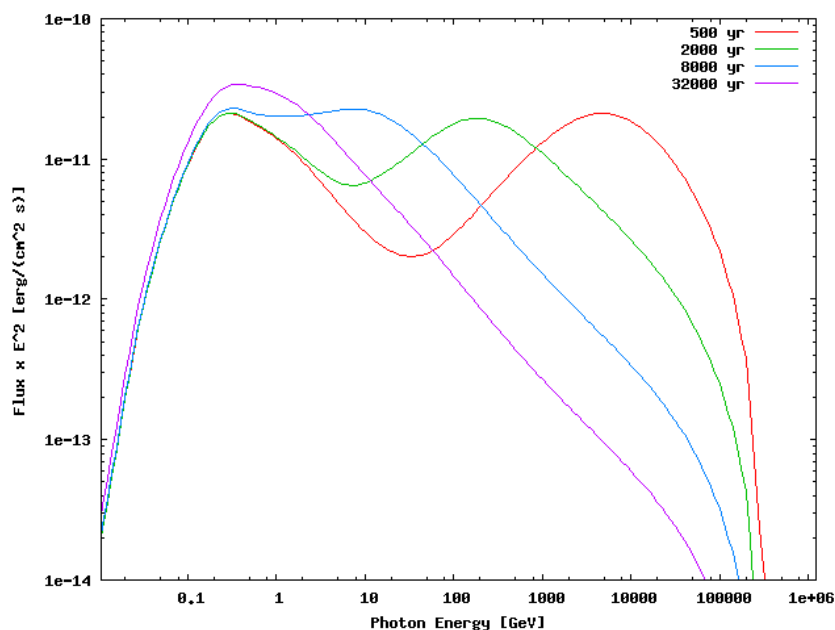
Figure 5.9: γ-ray spectrum of a molecular cloud with a mass of 10^5 solar masses located at a distance of 50 pc away from a SNR source. Different lines indicate different times after the supernova explosion. The following parameters are used: $M_{\mathrm{MC}}{=}10^5$ solar masses, $D_{10}{=}10^{28}$ cm^2/s, $E_\star = 10$ GeV, $E_{\mathrm{SN}} = 10^{51}$ erg, $\delta = 0.5$, $\eta = 0.3$, $\beta = 2.794$ and $t_{\mathrm{Sedov}} = 200$ yr.

The first peak in both spectra is always between about 0.1 and 1 GeV, which is the result of pion decay produced in hadronic interactions of background CRs in the dense gas of the molecular cloud. Comparing the GeV emission from the molecular cloud at a distance of 50 pc from the SNR with the one at 100 pc, one can see that the presence of the SNR affects the emission only at late times after the explosion and only if the distance is smaller or about 50 pc. The second peak at higher energies is due to hadronic interactions of CRs coming from the nearby SNR. This peak is moving in time to lower energies because CRs with higher energies are released first and with lower and lower energies CRs progressively reach the cloud at later times (see also Gabici et al. 2009(35)).
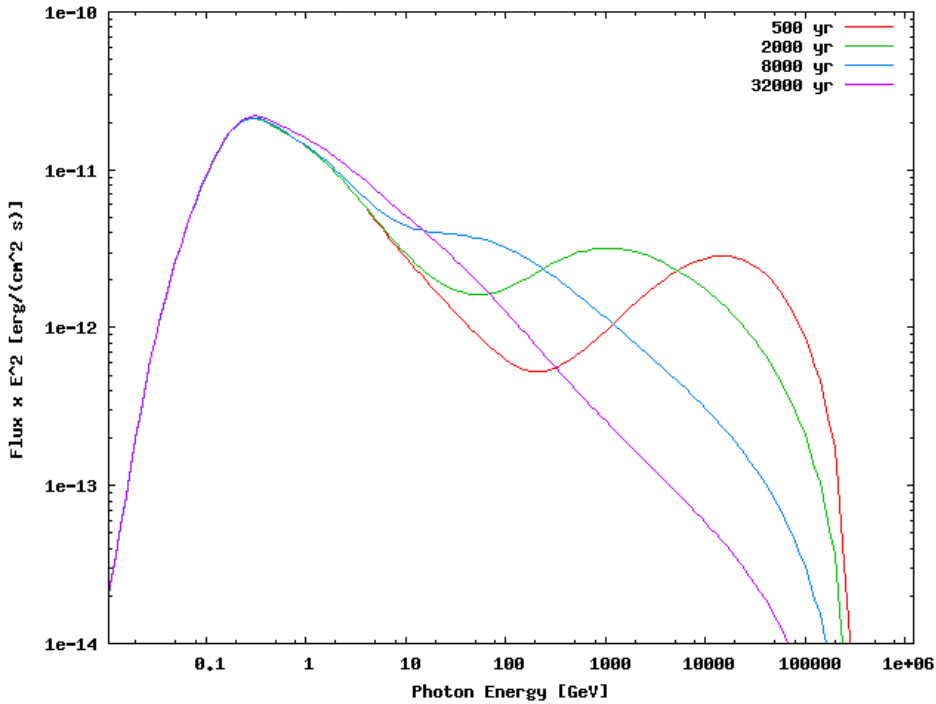
Figure 5.10: γ-ray spectrum of a molecular cloud with a mass of 10^5 solar masses located at a distance of 100 pc away from a SNR source. Different lines indicate different times after the supernova explosion. The following parameters are used: $M_{MC}=10^5$ solar masses, $D_{10}=10^{28}$ cm^2/s, $E_\star = 10$ GeV, $E_{SN} = 10^{51}$ erg, $\delta = 0.5$, $\eta = 0.3$, $\beta = 2.794$ and $t_{Sedov} = 200$ yr.

Chapter 6

Model of the diffuse γ-ray emission

6.1 Introduction

6.1.1 The GALPROP model

The most comprehensive numerical model for the diffuse γ-ray emission so far, which includes particle production and propagation in the Galaxy, is GALPROP[1] (see Strong et al. (2000)(53)). GALPROP is designed to perform cosmic-ray propagation calculations for nuclei, antiprotons, electrons and positrons, and computes diffuse γ-rays and synchrotron emission. In GALPROP the CR propagation equation is solved numerically on a spatial grid, either in 2D with cylindrical symmetry in the Galaxy or in full 3D. The numerical solution proceeds in time until a steady-state is reached. Normalisation of protons, helium and electrons to experimental data is provided (all other isotopes are determined by the source composition and propagation). γ-ray emission and synchrotron radiation are computed using interstellar gas data (for pion-decay and bremsstrahlung) and the interstellar radiation fields (ISRF) model (for inverse Compton). The spectra of all species on the chosen grid and the γ-ray and synchrotron sky-maps are then outputted in a standard astronomical format for comparison with the data. The following Fig. (6.1) shows the spectrum of Galactic diffuse γ-ray emission calculated with the GALPROP model.

---

[1]GALPROP is available from: `http://galprop.stanford.edu/`
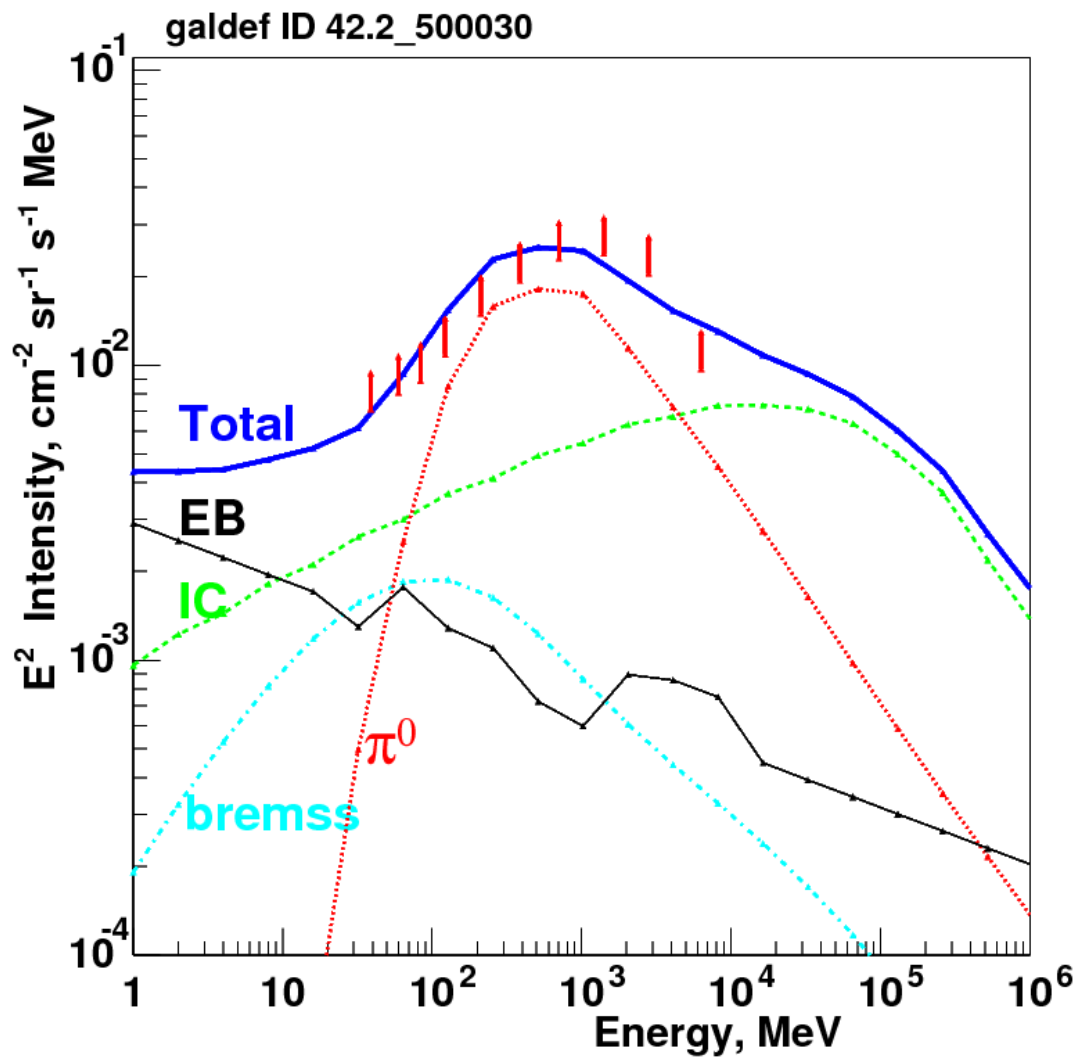
Figure 6.1: Spectrum of the Galactic diffuse γ-ray emission from the Galactic plane excluding the inner Galaxy ($30° < l < 330°$,$|b| < 5°$). The components shown are Inverse Compton (IC), bremsstrahlung (bremss), π^0-decay (π^0), the extragalactic diffuse emission (EB) and the EGRET data in bars. Taken from (Strong et al. 2003 (54))

6.1.2   The adopted model

The key feature that differentiates this approach from previous ones like GALPROP, is the stochastic distribution of SN explosions and pulsars in space and time. Furthermore, the injection history of all SNRs and pulsars is considered. This model aims to take these different factors into account.

The general idea of this model for the diffuse γ-ray emission is the following. A random distribution of sources (SNRs & pulsars) with cylindrical coordinates, following a specific distribution function in radial distance R from the Galactic center and distance z above the plane is assumed. These distributions are taken from radio observations. The distribution is random in the sense that the exact location and time of explosion (in case of a SNR) or birth (in case of a pulsar) is random, but the overall distribution still follows the corresponding distributions. For the SNRs and pulsars different types of injection mechanisms of CR particles, as described in chapter 5 can be used. Furthermore, it will be assumed that SNRs inject protons and pulsars electrons into the ISM. Once injected protons and electrons propagate in the ISM and interact with the ambient gas and radiation fields. The contribution from all SNRs and pulsars gives a proton and electron energy density/flux at specified points in space, depending on the age and location of the sources. Through inverse Compton and Bremsstrahlung the electrons produce γ-rays and their emissivity for every point in space can be calculated by assuming homogenous radiation fields in space. Also protons produce γ-rays in inelastic collisions with the gas. Only H_1 and H_2 gas is considered here, for which 3D data from the NANTEN and LAB survey described in chapter 2 is available. The resulting γ-ray spectrum is the sum of the contributions from electrons and protons interacting with the ISM.

Since the SNRs and pulsars are randomly distributed, different realisations of the Galaxy can be obtained. This means that the proton and electron flux at a specific point in space might vary depending on the specific realisation of CR sources distributed in the Galaxy. Furthermore, this might affect the resulting γ-ray spectrum as well.

In the following section the distribution of SNRs and pulsars will be described in detail and after that the results for the locally (meaning at the position of the Earth) calculated CR flux spectra will be shown.

The final results for the γ-ray spectrum will be shown in chapter 7.

6.2 The distribution of SNRs & pulsars in the Galaxy

6.2.1 SNR distribution

The true distribution of SNRs in the Galaxy is not well known, due to a lack of proper distance measurements to the remnants. Distances to the SNR can be derived from positional coincidences with H_1, H_2 and molecular clouds as well as pulsars or from measuring optical velocities and proper motions. If there is no direct distance measurement, estimates can be made by using the radio surface brightness-to-diameter relationship (Σ-D), since this mean surface brightness at a specific radio frequency Σ_ν is a distance independent parameter, which to a first approximation only depends on intrinsic properties of the SNR (Case & Bhattacharya 1998 (29)).

For the distribution of SNRs in the Galaxy the following functional forms in cylindrical coordinates is used, adapted from Case & Bhattacharya 1998 (29)

Radial distribution:

$$f(r) = \left(\frac{br}{ar_s}\right)^a \exp\left(\frac{ar_s - br}{r_s}\right) \tag{6.1}$$

z distribution:

$$f(z) = \frac{1}{\cosh(zh_g)} \tag{6.2}$$

where r is the radial distance from the Galactic center and z is the height above the plane. The following parameters are used, a = 1.69, b = 3.33, r_s = 8.5 kpc and h_g = 30 kpc^{-1} (see Pohl et al. 2005(48)). The position of the SNRs in Galactic azimuth ϕ is uniformly distributed as is the point in time when the SNRs began injecting (continuous sources) or injected (impulsive sources) cosmic rays into the ISM. The rate of supernova explosions is assumed to be 2-3 per 100 years (Ferriere 2001 (34)).

To get a random distribution of radial distances r from the Galactic center or height z above the Galactic plane of the Galaxy according to the above formulas I used the inverse transform sampling and the acceptance-rejection method.

The inverse transform sampling works as follows:

If X is a continuous random variable, with F_X being a cumulative distribution function defined as

$$F_X = \int_{-\infty}^{x} f(t)dt \tag{6.3}$$

where f(t) is a probability density function. If $Y = F_X(X)$, then Y is randomly distributed on [0,1].

If the inverse of F_X exists, it follows that $X = F_X^{-1}(Y)$ is distributed according to the cumulative distribution function F_X. Since eq. (6.2) is symmetric with respect to the y-axis it follows:

$$F_X(z) = \int_0^z dz' f(z') = \int_0^z dz' \frac{1}{\cosh(z'h_g)} = \frac{4 \cdot \arctan(e^{h_g \cdot z}) - \pi}{2h_g} \tag{6.4}$$

This needs to be normalized on the interval $[0,\infty)$, which results in:

$$\int_0^\infty dz' \frac{1}{\cosh(z'h_g)} = \frac{\pi}{2h_g} = \frac{\pi}{60} \tag{6.5}$$

By setting:

$$\frac{F_X(z)}{\pi/60} = u \tag{6.6}$$

where u = Y and is therefore uniformly distributed on [0,1].

Solving eq. (6.6) for z, the final result can be obtained:

$$z = \ln\left(\tan\left(\frac{h_g \pi u}{120} + \frac{\pi}{4}\right)\right) / h_g \tag{6.7}$$

This result provides z coordinates for SNRs that are distributed according to (6.2).

For the radial distribution I used the acceptance-rejection method which does the following:

- Calculate a random r_{rnd} in the desired range $[r_{min}, r_{max}]$,
  e.g. $r = r_{min} + (r_{max} - r_{min}) \cdot u$

- Evaluate the distribution function eq. (6.1) at this r_{rnd}

- Calculate a random f like $f_{rnd} = f_{max} \cdot u$

- If f_{rnd} is less than the evaluated distribution function at r_{rnd} take it

- Otherwise calculate a new r_{rnd} and continue

Where u is the already defined randomly distributed variable on [0,1] and f_{max} is the maximum of the distribution function described in eq. (6.1). The minimum and maximum radial distance is taken to be $r_{min} = 0$ kpc and $r_{max} = 30$ kpc, which

is reasonable since the distribution function is $\propto \exp(-r/r_s)$ and r_s is only 8.5 kpc. The following figures illustrate the SNR distribution uniformly distributed in the time, assuming a supernova rate of $3/(100 \text{ yr})$:
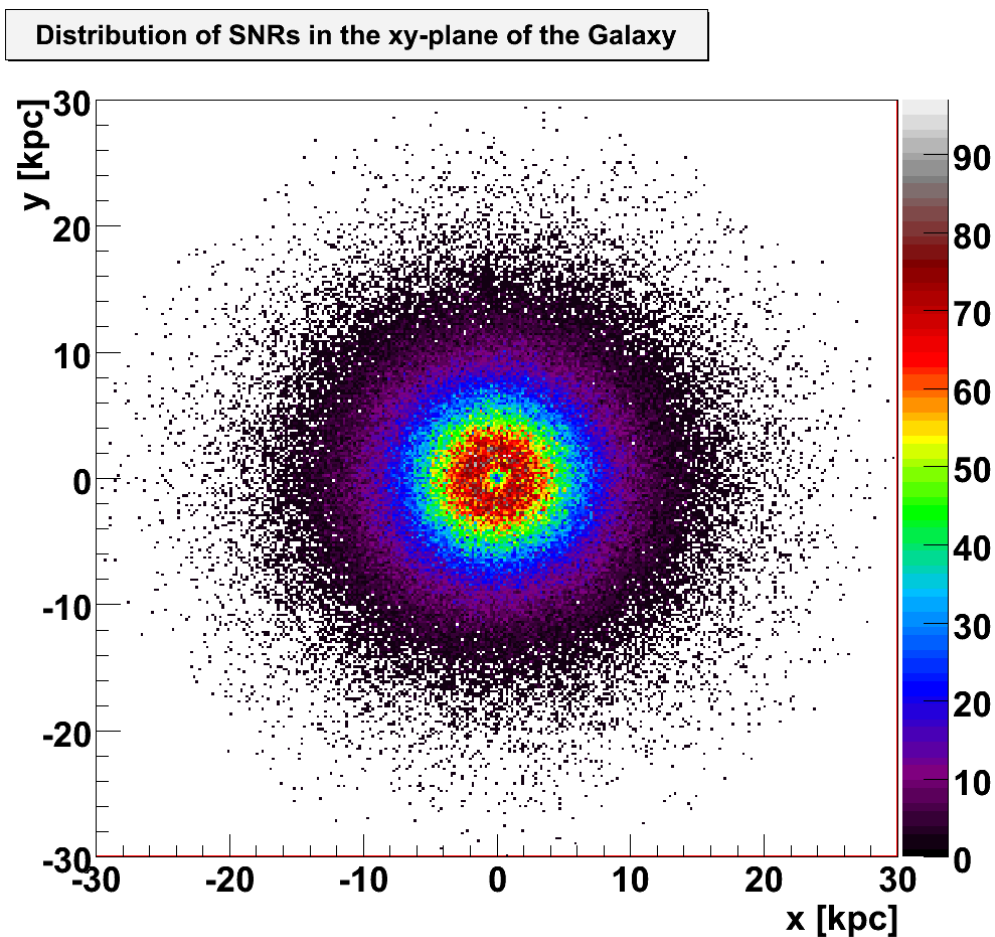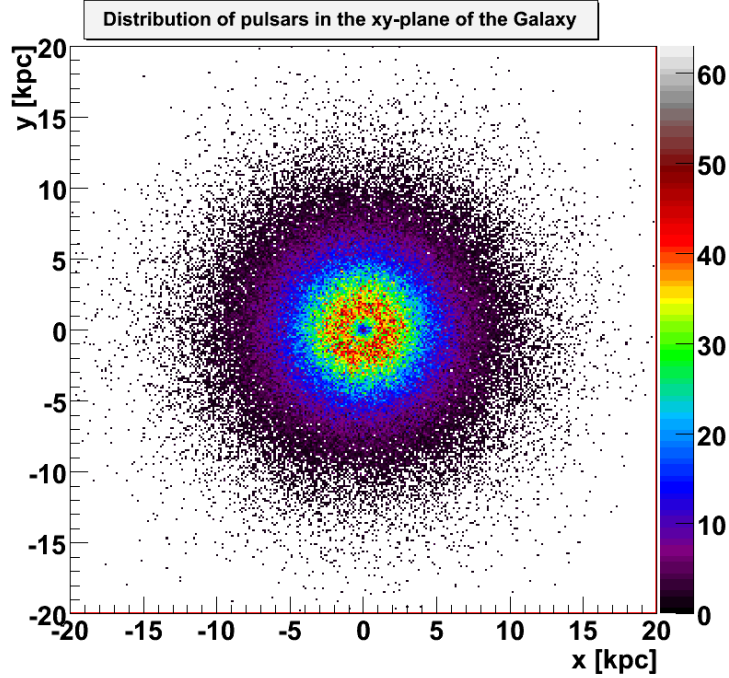

Figure 6.2: Number of SNRs distributed in the xy-plane of the Galactic disk for a time interval of 10^7 yr ($3 \cdot 10^5$ SNRs).
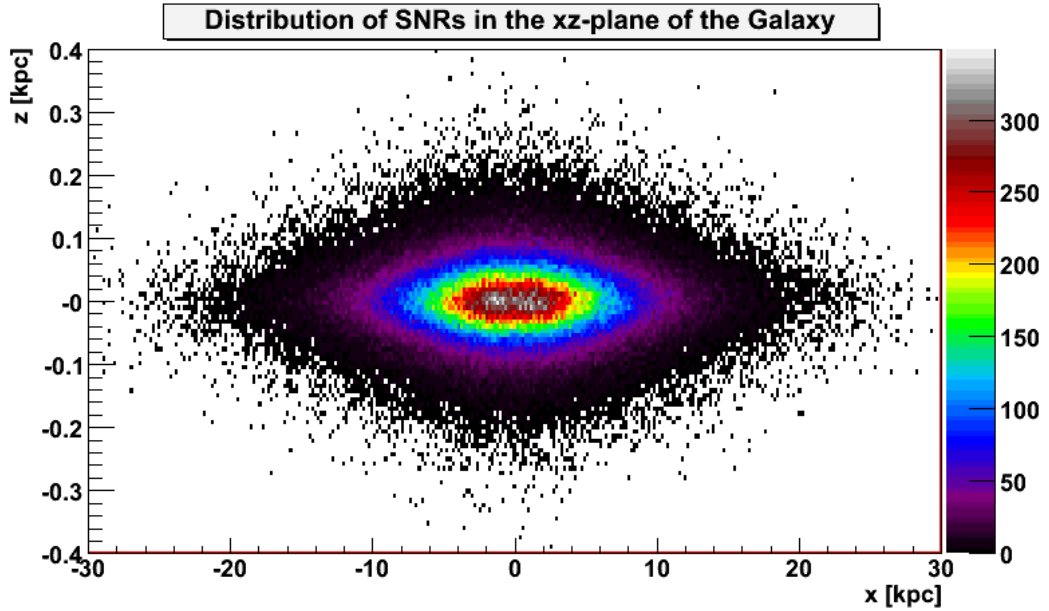
Figure 6.3: Number of SNRs distributed in the xz-plane of the Galactic disk for a time interval of 10^7 yr ($3 \cdot 10^5$ SNRs).
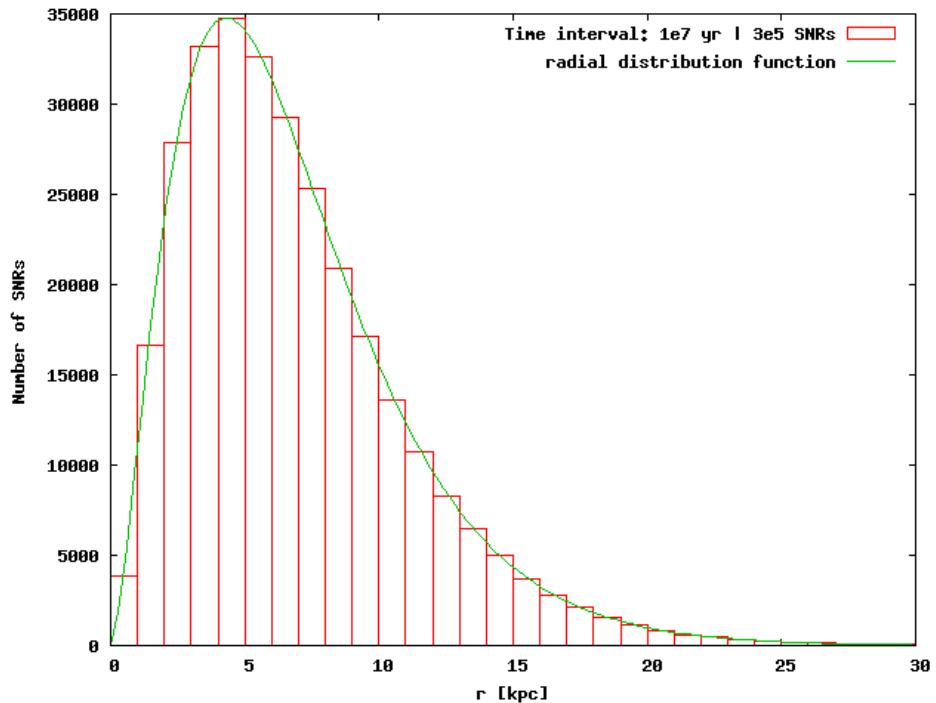
Figure 6.4: Number of SNRs as a function of the radial distance from the Galactic center for a time interval of 10^7 yr ($3 \cdot 10^5$ SNRs). The superimposed green line represents the radial distribution function given in eq. (6.1).

59
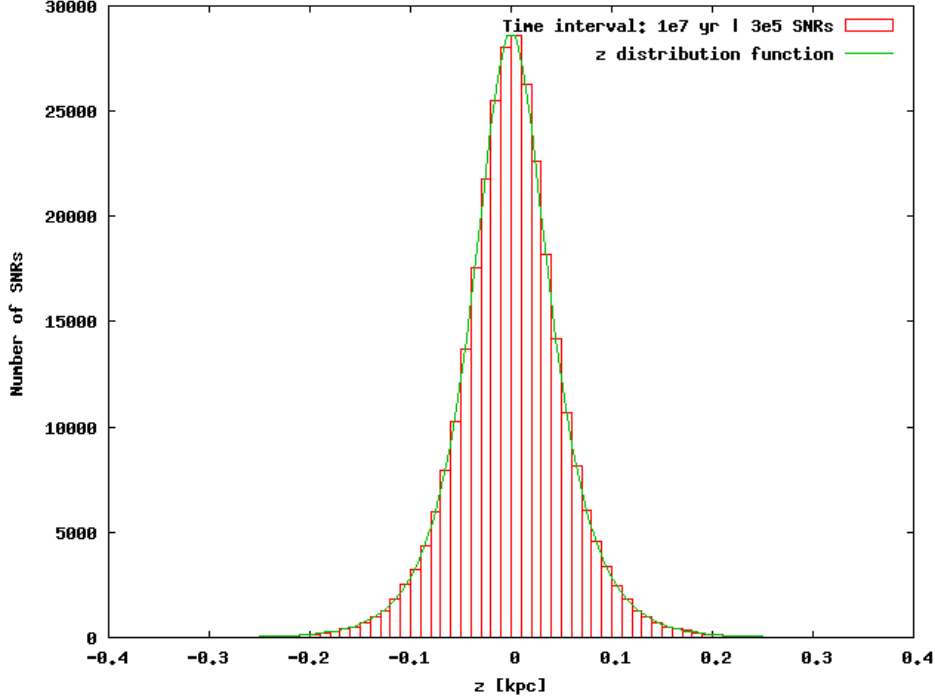
Figure 6.5: Number of SNRs as a function of the height z above the plane of the Galactic disk for a time interval of 10^7 yr $(3 \cdot 10^5$ SNRs). The superimposed green line represents the z distribution function given in eq. (6.2).

6.2.2 Pulsar distribution

Since higher energetic electrons can not leave the shell of the SNRs because of radiation losses due to very high magnetic field strengths, it is assumed that pulsars inject electrons into the ISM. For the radial distribution the following form is used(taken from Lorimer et al. (2006) (44))

$$f(r) = a \left(\frac{r}{r_0} \right)^b e^{\left[-c \left(\frac{r-r_0}{r_0} \right) \right]} \tag{6.8}$$

with the parameters a = 41 kpc^{-2}, b = 1.9, c = 5.0 and r_0 = 8.5 kpc. For the z distribution I used again eq. (6.2) as for the SNRs, whereas the ϕ and t are again uniformly distributed. The birth-rate of pulsars is assumed to be 1/(50 yr) (Caliandro et al. (2010) (26))

Figure 6.6: Number of pulsars distributed in the xy-plane of the galactic disk for a time interval of 10^7 yr $(2 \cdot 10^5$ pulsars).
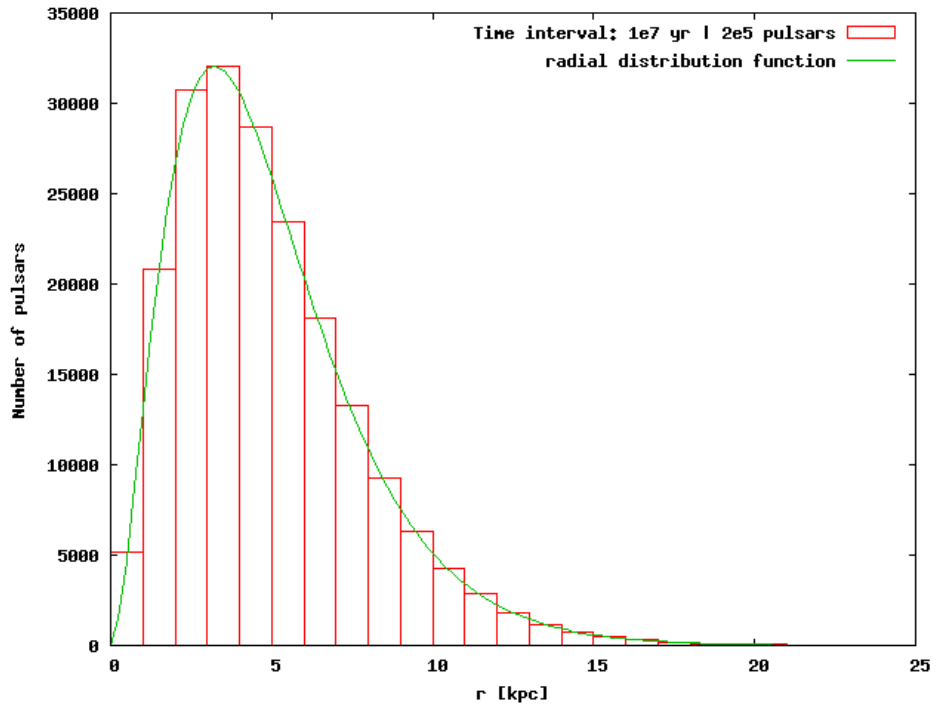
Figure 6.7: Number of pulsars as a function of the radial distance from the galactic center for a time interval of 10^7 yr $(2 \cdot 10^5$ pulsars). The superimposed green line represents the radial distribution function given in eq. (6.8).

61

6.3 Stochastic SNR explosions and e⁻ and p fluxes in the Galaxy

In this chapter I will discuss the results for calculation of the local CR flux, meaning the CR flux at the position of the Earth, for the different injection mechanisms.

I calculated the local CR spectrum using the SNR and pulsar distribution in section (6.2.1) and (6.2.2) respectively. The following assumptions are made:

- Diffusion power-law $D(E) = D_{10} \left(\frac{E}{E_\star} \right)^\delta$ with $\delta = 0.3$ - 0.7

- $D_{10} = 10^{26}$ - 10^{29} cm^2/s and $E_\star = 1$ GeV and $E_\star = 10$ GeV

- The rate of supernova explosions is assumed to be $3 \cdot 10^{-2}$ yr^{-1}

- The birth-rate of pulsars is assumed to be $2 \cdot 10^{-2}$ yr^{-1}

- Proton and electron power-law index for burst-like and continuous injection is $\Gamma_p = \Gamma_e = 2.2$. For protons injected using the SNR model it is only $\Gamma_p = 2$. $\left(\frac{dN}{dE} \propto E^{-\Gamma_{e/p}} \right)$

- Energy that goes into CR acceleration is assumed to be 30% of the total energy output of the SNR and pulsar.

The energy output of the SNR and pulsar is assumed to be the same for every SNR and pulsar and is calculated by considering the following comparison

$$\int_{E_1}^{E_2} E \cdot \sum_i J_{\text{calc,i}}(E, R_i, t_i) dE \overset{!}{=} \int_{E_1}^{E_2} E \cdot J_{\text{meas}}(E) dE \tag{6.9}$$

where $J_{\text{calc,i}}(E, R_i, t_i) = c/(4\pi) \cdot f(E, R_i, t_i)$ is the flux that the i-th SNR contributes to the overall proton flux and the i-th pulsar to the overall electron flux at a distance R_i from the Earth and at a time t_i the event happened. The quantity $J_{\text{meas}}(E)$ is the measured CR flux at the position of the Earth. The energy distribution function $f(E, R, t)$ depends on the injection mechanism and whether it describes protons or electrons. For example for burst-like injection it is given by eq.(5.5) for the protons and by eq. (5.14) for the electrons. By doing this it is assumed that in the energy range $E_1 < E < E_2$ the measured proton or electron flux $J_{\text{meas}}(E)$ is described e.g. by eq. (5.5) and eq. (5.14) respectively. The procedure is then to calculate the proton/electron flux

of CR that all SNR/pulsar produce at the position of the Earth where the quantity N_0 or Q_0 (for example in (5.5) (protons) and in (5.14) (electrons)) is set to unity and then to normalize it by a factor C in the following way:

$$C = \frac{\int_{E_1}^{E_2} E \cdot J_{\mathrm{meas}}(E)dE}{\int_{E_1}^{E_2} E \cdot \sum_i J'_{\mathrm{calc,i}}(E, R_i, t_i)dE} \tag{6.10}$$

with $J'_{\mathrm{calc}}(E) = \sum_i J'_{\mathrm{calc,i}}(E, R_i, t_i)$ being the calculated flux with the quantity N_0 or Q_0 set to unity. The normalized flux is then given by

$$J_{\mathrm{calc,i}}(E) = C \cdot J'_{\mathrm{calc,i}}(E) \tag{6.11}$$

For the following locally calculated CR spectra, it should be noted that it is assumed that in a specified region around the Earth no SNR or pulsar can fall during distribution of both sources. The radius of a sphere in which no SNR can fall is assumed to be the distance to the closest SNR, which is the Vela SNR at a distance of about 250 pc (Alexandra et al. 1999(17)). For the pulsars, PSR J0108-1431 is assumed as the closest pulsar at a distance of about 85 pc (Tauris et al. 1994(58)). This is especially important, for the locally calculated electron spectrum an will be discussed later.

6.3.1 Proton flux spectrum

On the next few pages it will be shown how the different injection mechanisms as well as the parameters of the model alter the obtained local CR flux spectrum. At first this will be illustrated for the proton flux spectrum and then for the electron spectrum. In the following the resulting spectral index will be displayed as the result of a fit in the legend of the figures. It is obtained by fitting a power-law $f(x) = 10^a \cdot x^b$ to the data. This is done to qualitatively show the changes in the spectral index for the different parameters and injection mechanisms of the model. It should be mentioned that the resulting slope of the fit depends on the energy range of the perfomed fit, which in this case was between 10^4 and 10^6 GeV. The three Fig. (6.8), (6.9) and (6.10) illustrate the local CR flux spectrum for the three different injection mechanisms, burst-like, continuous with a constant rate and using the SNR model. It can be seen that for the SNR model the spectral indices are lower by approximately 0.2 than in the case for burst-like injection. This is expected since the proton power-law index for burst-like injection is assumed to be 2.2 instead of 2 for the SNR model.
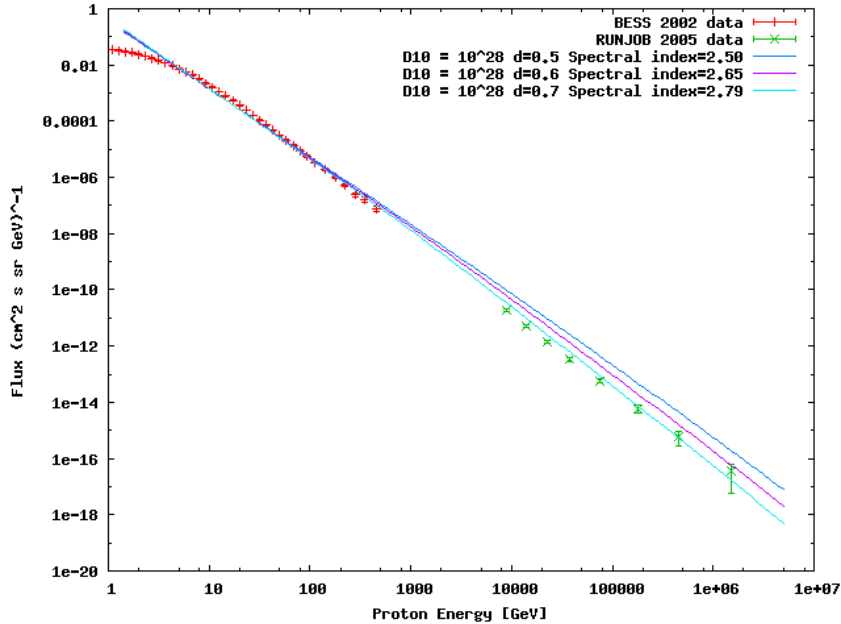
Figure 6.8: Calculated local proton flux spectrum for burst-like injection and 3 different values of the diffusion power-law index $\delta = 0.5$, 0.6 and 0.7. $D_{10} = 10^{28}$ cm^2/s and $E_\star = 1$ GeV
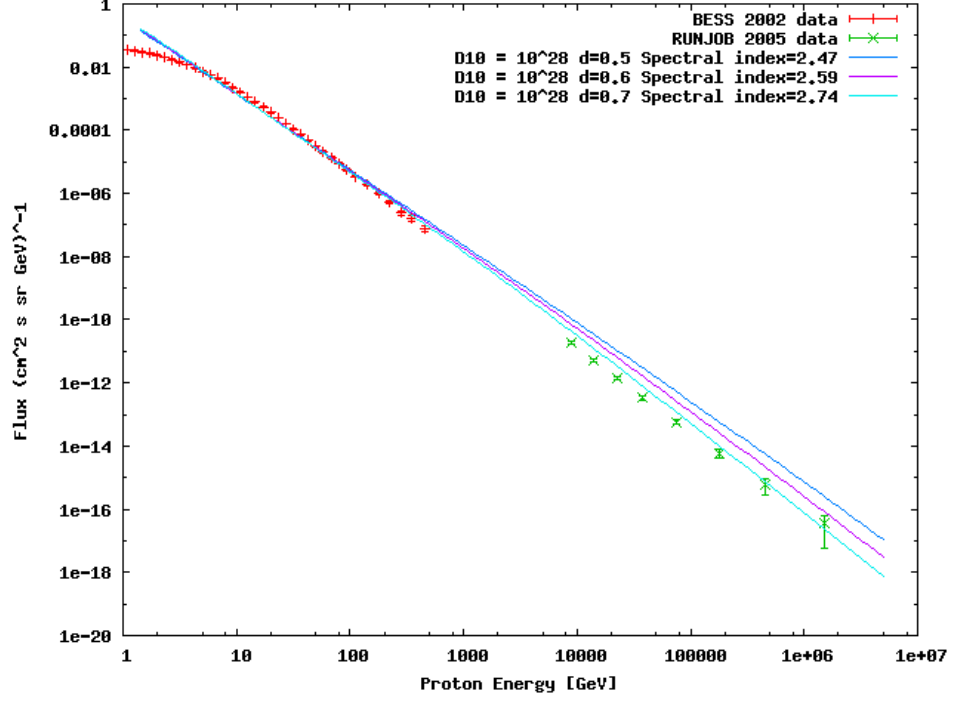
Figure 6.9: Calculated local proton flux spectrum for continuous injection with a constant rate and 3 different values of the diffusion power-law index $\delta = 0.5$, 0.6 and 0.7. $D_{10} = 10^{28}$ cm^2/s and $E_\star = 1$ GeV
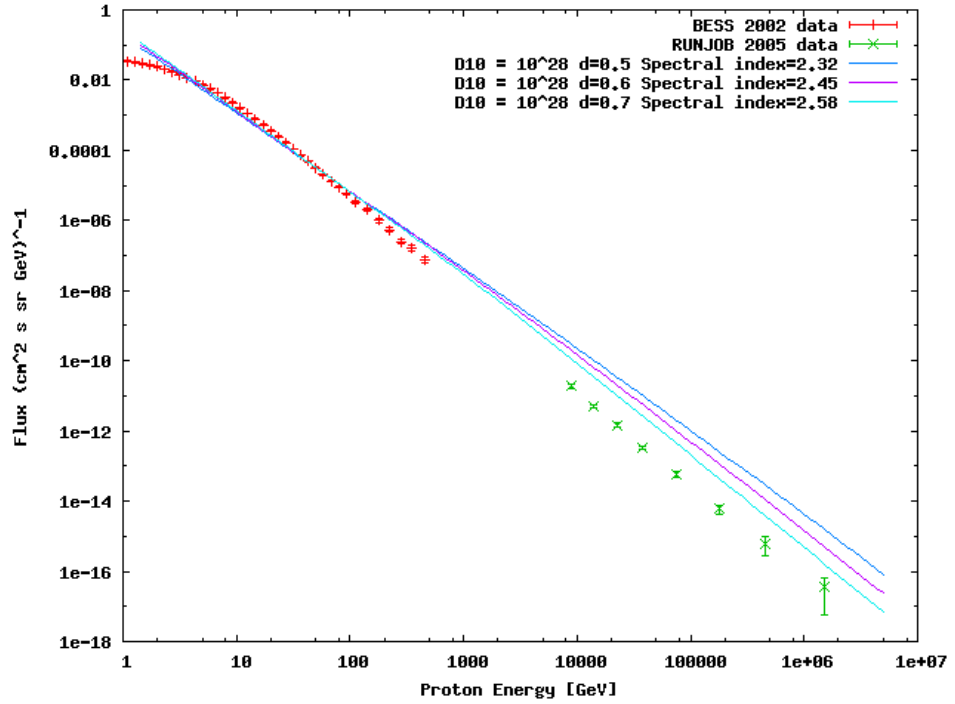
Figure 6.10: Calculated local proton flux using the SNR model and 3 different values of the diffusion power-law index $\delta = 0.5$, 0.6 and 0.7. $D_{10} = 10^{28}$ cm^2/s and $E_\star = 1$ GeV

6. MODEL OF THE DIFFUSE γ-RAY EMISSION

In the case of continuous injection with a constant rate, see Fig. (6.9), the spectral index is only slightly lower compared to the burst-like injection. However, since for a continuous source the spectral index should be smaller by $\delta/2$ than in the case of an impulsive one (see eq. (5.12) and eq. (5.7)) the obtained spectral index is larger than expected. This could be due to the fact that the assumed energy range for the fit has a strong impact on the resulting spectral index. The injection mechanism utilizing the SNR model described in seq. (5.1.2) is the most realistic one of the presented mechanisms. Firstly, compared to the burst-like scenario it takes into account the fact that the maximum energy of particles that can be confined within the SNR decreases with time, which means it takes more time for lower energetic protons to leave the SNRs. Secondly, compared to the continuous case the age of the bulk of SNRs is around 10^6-10^7 years, which is much greater than the typical timeframe of injection (see section 5.1.1). However an initial proton power-law index of 2 does not seem to be favored, when looking at Fig. (6.10), since the spectral index does not come even close to the expected value of about 2.7 (valid only up to the so called knee at about 10^6 GeV). Therefore, the burst-like injection scenario is used whenever the proton flux in the Galaxy is calculated.

In the next few figures the impact of the diffusion coefficient D_{10} on the spectral index will be shown. Fig. (6.11) illustrates that for a smaller diffusion coefficient of $D_{10} = 10^{27}$ cm^2/s a higher power-law diffusion coefficient of $\delta > 0.7$ would be required to model the measured local proton flux spectrum. Furthermore, for a higher diffusion coefficient of $D_{10} = 10^{29}$ cm^2/s one would need a power-law diffusion coefficient below $\delta = 0.6$, see Fig. (6.12), but a diffusion coefficient of $D_{10} = 10^{29}$ cm^2/s might be too high and not justifiable from recent constraints on the diffusion coefficient (Evoli et al. 2010(33)).
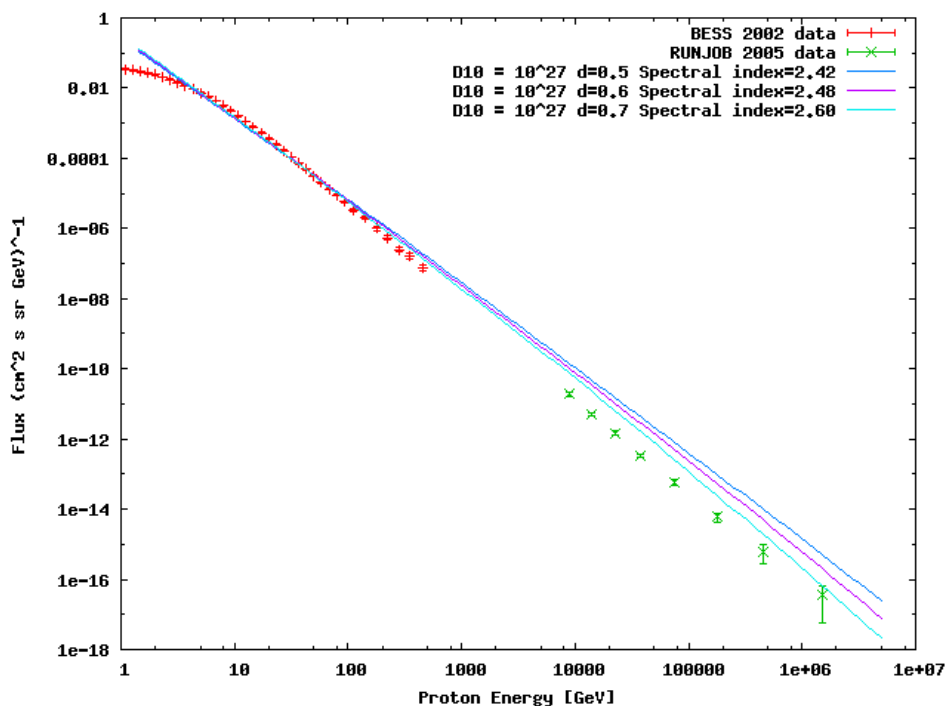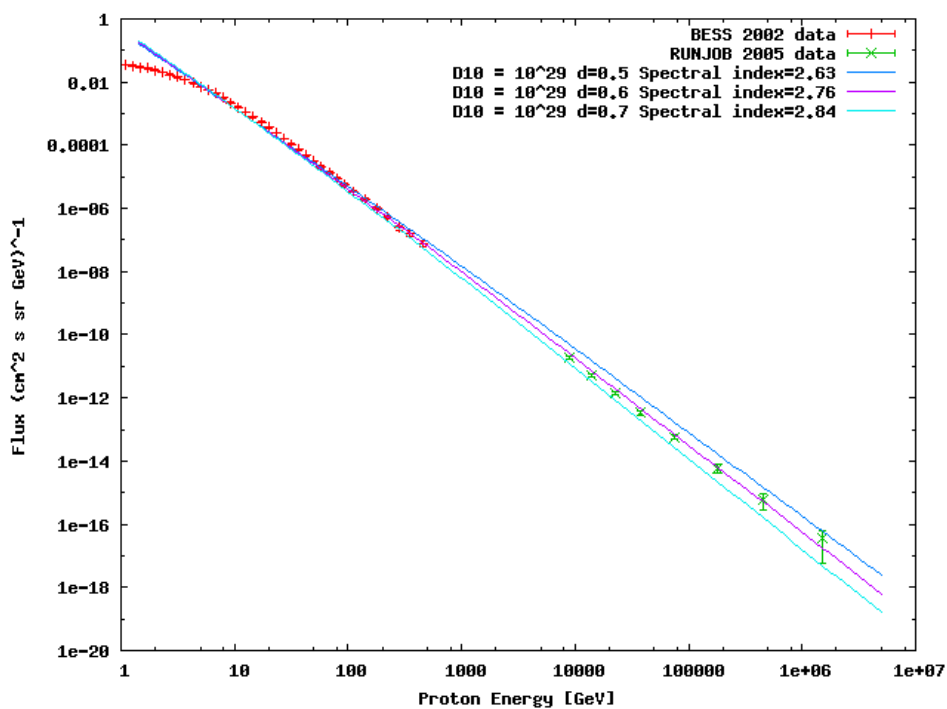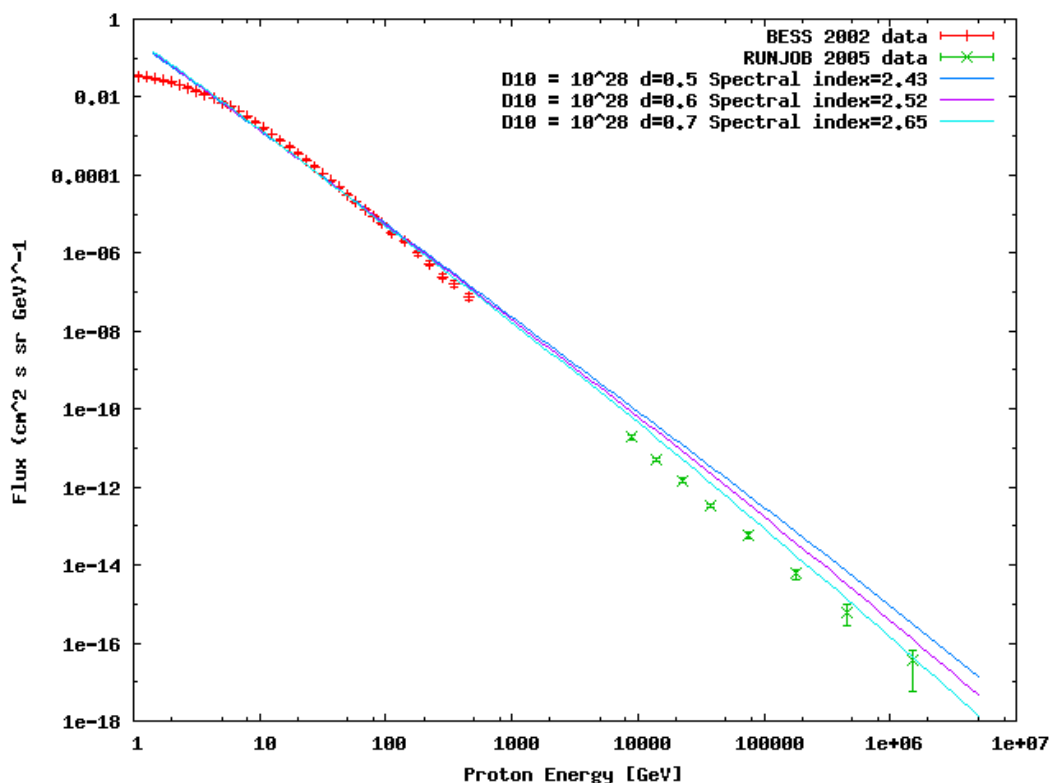
Figure 6.11: Calculated local proton flux spectrum for burst-like injection and 3 different values of the diffusion power-law index $\delta = 0.5$, 0.6 and 0.7. $D_{10} = 10^{27}$ cm^2/s and $E_\star = 1$ GeV

Figure 6.12: Calculated local proton flux spectrum for burst-like injection and 3 different values of the diffusion power-law index $\delta = 0.5$, 0.6 and 0.7. $D_{10} = 10^{29}$ cm^2/s and $E_\star = 1$ GeV

As Fig. (6.8) shows, a diffusion coefficient of $D_{10} = 10^{28}$ cm^2/s and a δ between 0.6-0.7 is needed to be in agreement with the measured spectral index of 2.7 at Earth. Note that the quantiy $E_\star$ was assumed to be equal to 1 GeV, because this value has also influence on the spectral index. This can be observed from Fig. (6.13) where it is assumed that $E_\star = 10$ GeV. The resulting spectra are not as steep as the ones displayed in Fig. (6.8).

Figure 6.13: Calculated local proton flux spectrum for burst-like injection and 3 different values of the diffusion power-law index $\delta = 0.5$, 0.6 and 0.7. $D_{10} = 10^{28}$ cm^2/s and $E_\star = 10$ GeV

In all the previous calculations and plots, the SNRs and pulsars are randomly distributed in space and time. Randomly in the sense that the exact location and time of explosion (in case of a SNR) or birth (in case of a pulsar) is random, but the overall distribution still follows the corresponding distributions mentioned above. In the following i will show how different realisations of the Galaxy with respect to the SNR distribution affect the measured proton flux spectrum at Earth. In Fig. (6.14) one can see that in the case of protons the distribution of SNRs in the Galaxy does not change the spectral index very much, which is plausible since the bulk of SNRs is around 10^6-10^7 years old, so the protons had enough time to isotropize within the Galaxy. Furthermore for the assumed D$_{10} = 10^{28}$ cm^2/s and $\delta = 0.6$ the spectral index can be close to the expected 2.7.
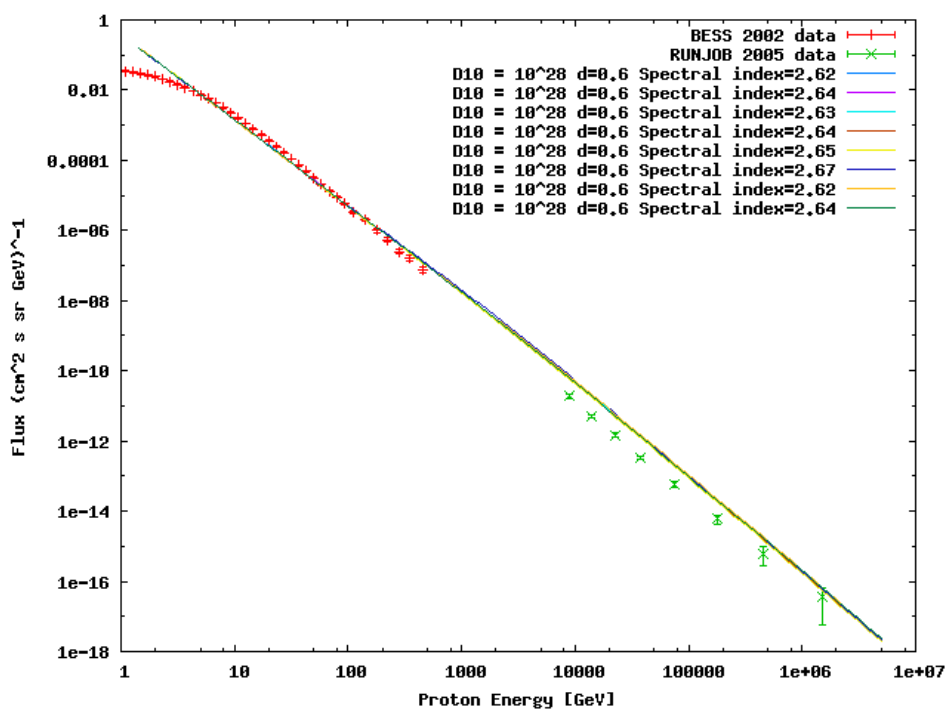
Figure 6.14: Calculated local proton flux spectrum for burst-like injection for a diffusion power-law index $\delta = 0.6$. D$_{10} = 10^{28}$ cm^2/s and E$_\star = 1$ GeV , for 8 different realisations of the Galaxy

6.3.2   Electron flux spectrum

The following Fig. (6.15) shows the relative contributions from different regions of the Galactic Disk to the overall flux of electrons. The electrons are assumed to be continuously injected with a constant rate by pulsars, which are distributed within the Galaxy and located at distances r $\geq$ r$_0$ for different r$_0$. Even at energies of several 10 GeV the total flux of observed electrons is dominated by particles injected from sources at distances r $\leq$ 1 kpc from the Earth. It is clear from Fig. (6.15), that the
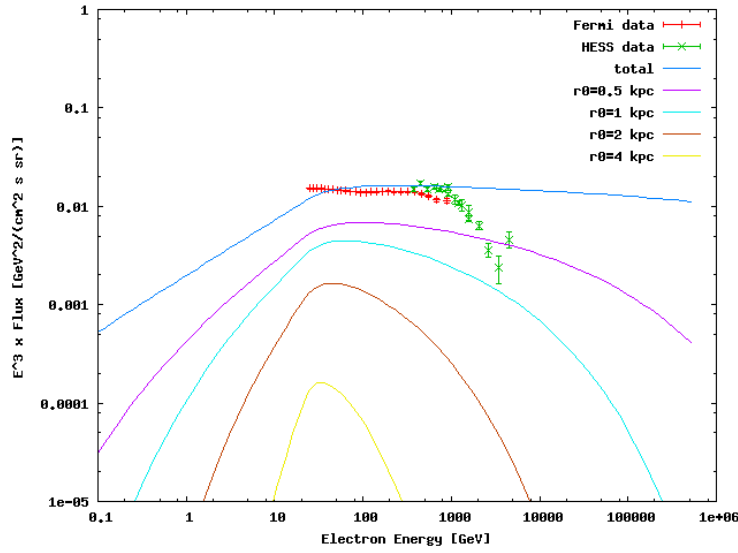
Figure 6.15: Flux of CR electrons continuously injected with a constant rate by pulsars. The overall flux (blue curve) is decomposed in order to show the contributions from the sources located at distances r $\geq$ r$_0$ for different r$_0$.

distribution of sources has a high impact on the overall electron flux at different points in the Galaxy. The following Figures will illustrate how the different parameters and injection mechanisms change the local electron flux spectrum. Additionally the impact of different realisations of the Galaxy on the local electron flux spectrum will also be shown.

The 'spiky' features of the electron flux at higher energies in Fig. (6.16) are due to the fact that for burst-like injection no electrons are additionaly delivered after the first injection. This fact becomes especially important for high energetic electrons since rapidly growing IC losses reduce the lifetime of those electrons and this affects their mean diffusion length.
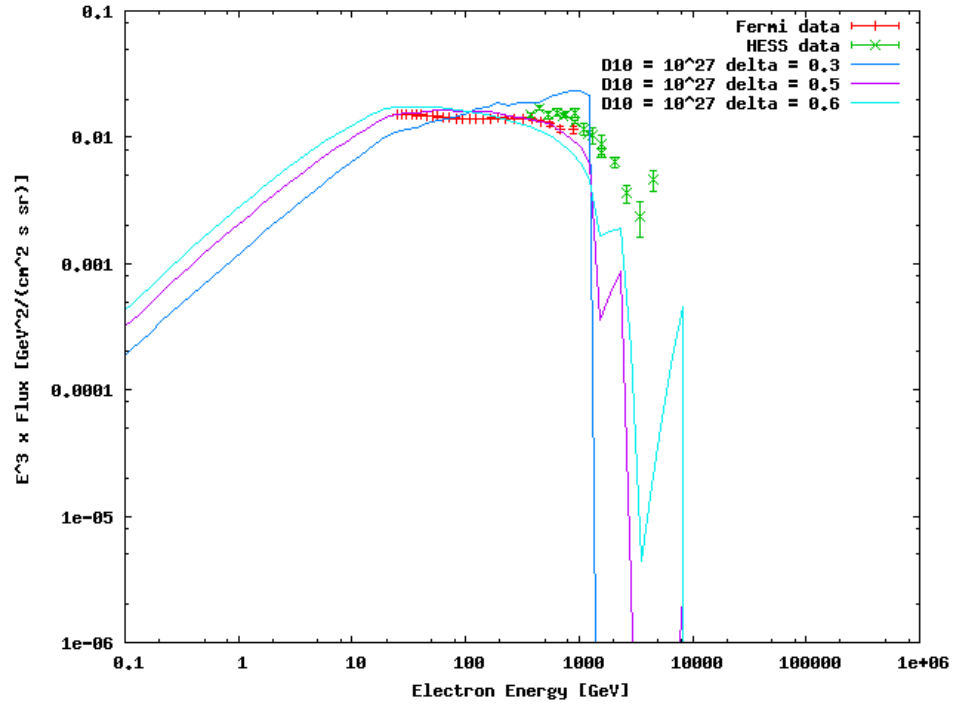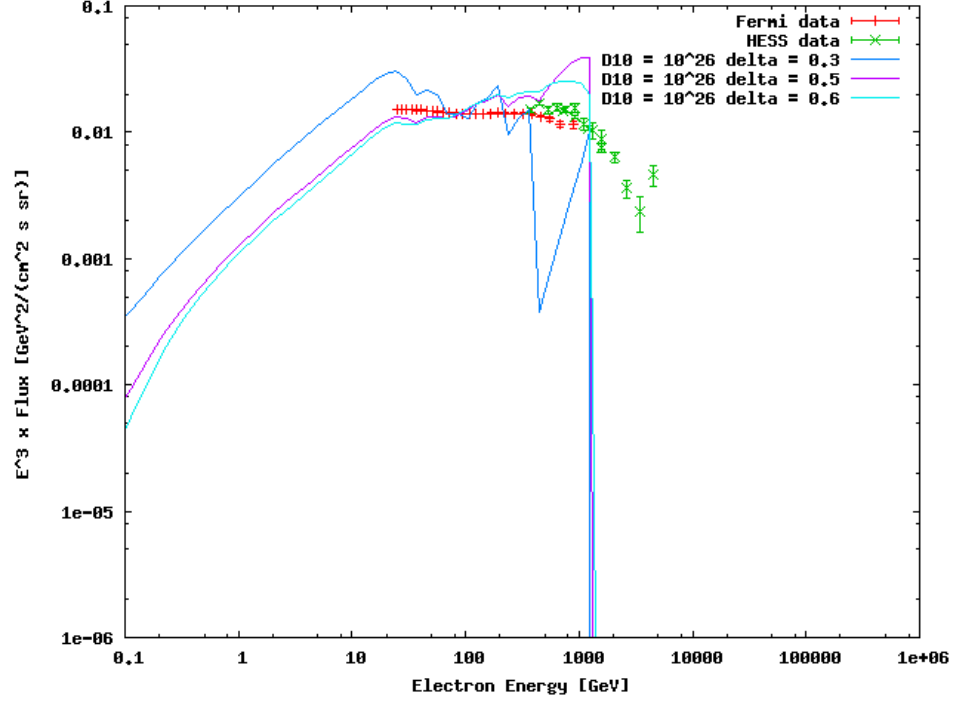

Figure 6.16: Calculated local electron flux spectrum for burst-like injection and 3 different values of the diffusion power-law index $\delta = 0.3$, 0.5 and 0.6. $D_{10} = 10^{27}$ cm^2/s and $E_\star = 1$ GeV

This is not the case for continuous injection with a constant rate as shown in Fig. (6.17), since here additional electrons are delivered and the energy losses at high energies do not abruptly cut-off the spectra at high energies anymore compared with the case of burst-like injection in Fig. (6.16).
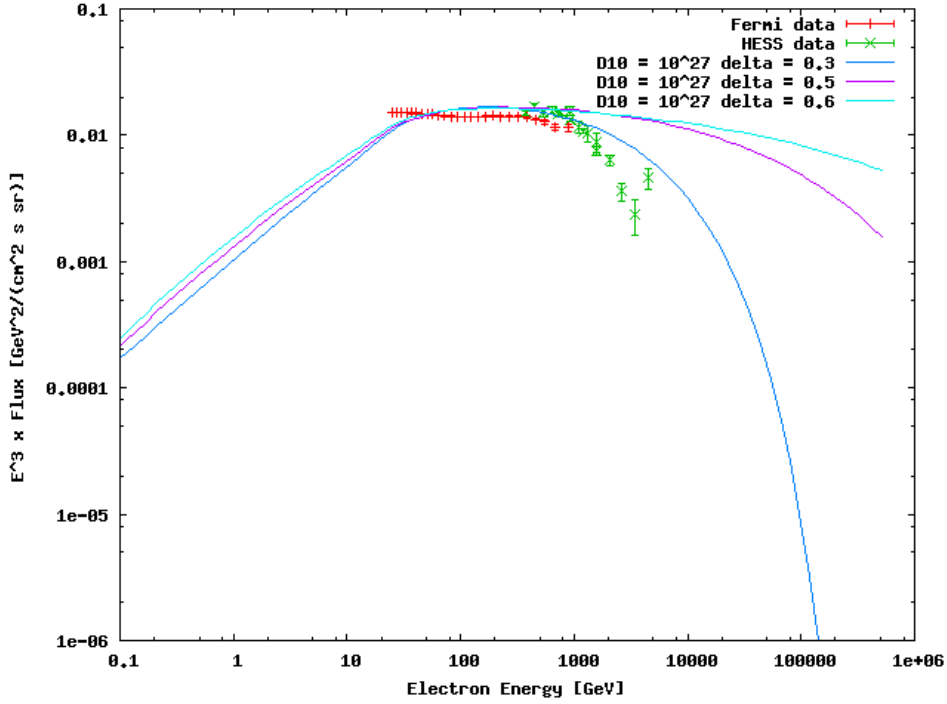
Figure 6.17: Calculated local electron flux spectrum for continuous injection with a constant rate and 3 different values of the diffusion power-law index $\delta = 0.3$, 0.5 and 0.6. $D_{10} = 10^{27}$ cm^2/s and $E_\star = 1$ GeV

The next few figures will illustrate the impact of the diffusion coefficient D_{10} on the shape of the electron spectrum. Fig. (6.18) shows that for a smaller diffusion coefficient of $D_{10} = 10^{26}$ cm^2/s one gets a smaller plateau between roughly 10 GeV and 1 TeV, which is due to the fact that the electrons diffuse more slowly and therefore energy losses take a greater toll on the high energetic electrons. This is due to the fact that the electrons are exposed to energy losses on a larger timeframe, than they would have been if the diffusion coefficient is higher, which can be seen in Fig. (6.19) for $D_{10} = 10^{28}$ cm^2/s. Furthermore, the energy loss rate scales with E^2 in the Thomson regime (see eq. (4.6)) which emphasizes the impact of the diffusion coefficient stronger at higher energies.

Figure 6.18: Calculated local electron flux spectrum for burst-like injection and 3 different values of the diffusion power-law index $\delta = 0.3$, 0.5 and 0.6. $D_{10} = 10^{26}$ cm^2/s and $E_\star = 1$ GeV
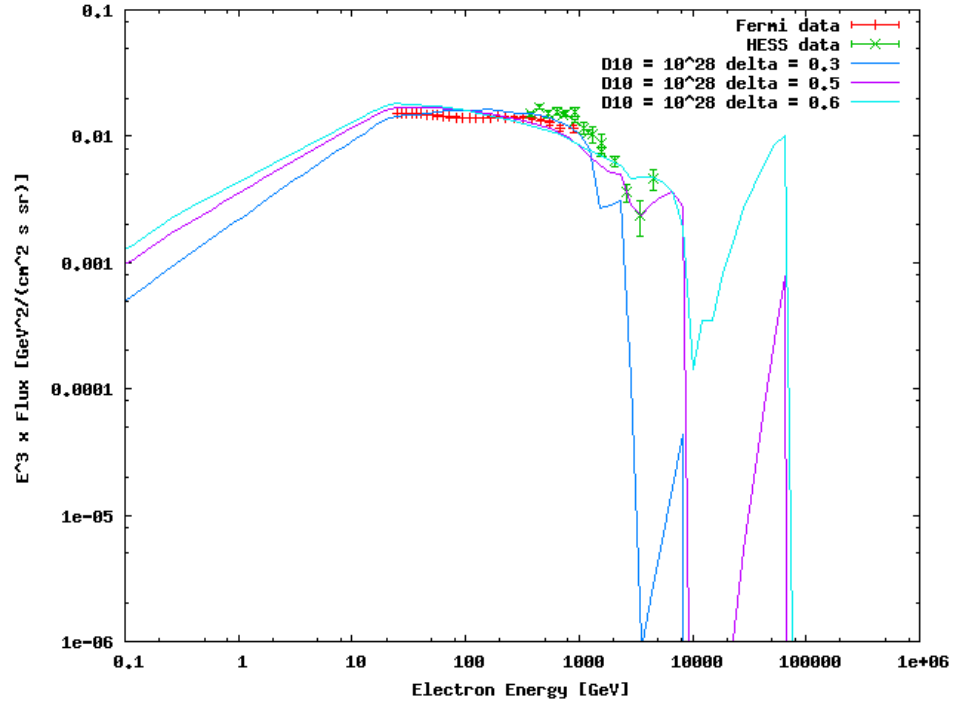

Figure 6.19: Calculated local proton flux spectrum for burst-like injection and 3 different values of the diffusion power-law index $\delta = 0.3$, 0.5 and 0.6. $D_{10} = 10^{28}$ cm^2/s and $E_\star = 1$ GeV

In the case of continuous injection with a constant rate, the same behaviour as in the case for burst-like injection can be observed. It can be seen from Fig. (6.20) that the flux of high energetic electrons strongly declines for a lower diffusion coefficient. This is not the case for a higher diffusion coefficient seen in Fig. (6.21). The reason for this is the same as for the burst-like case and is mentioned above.
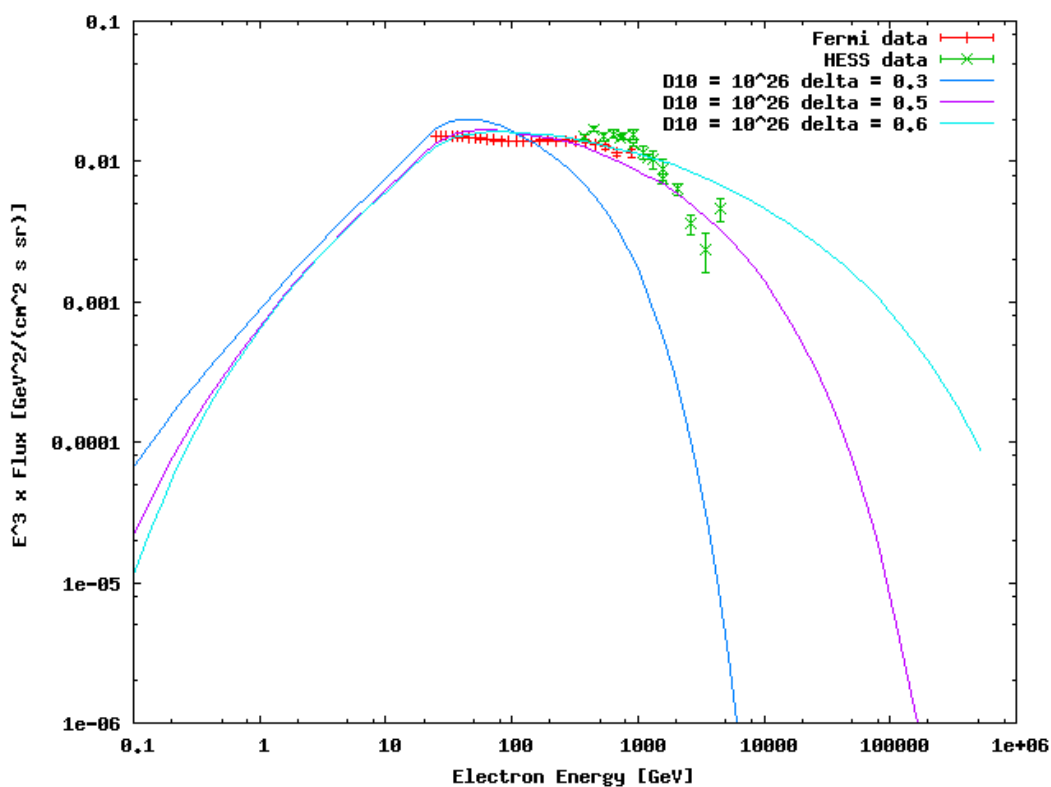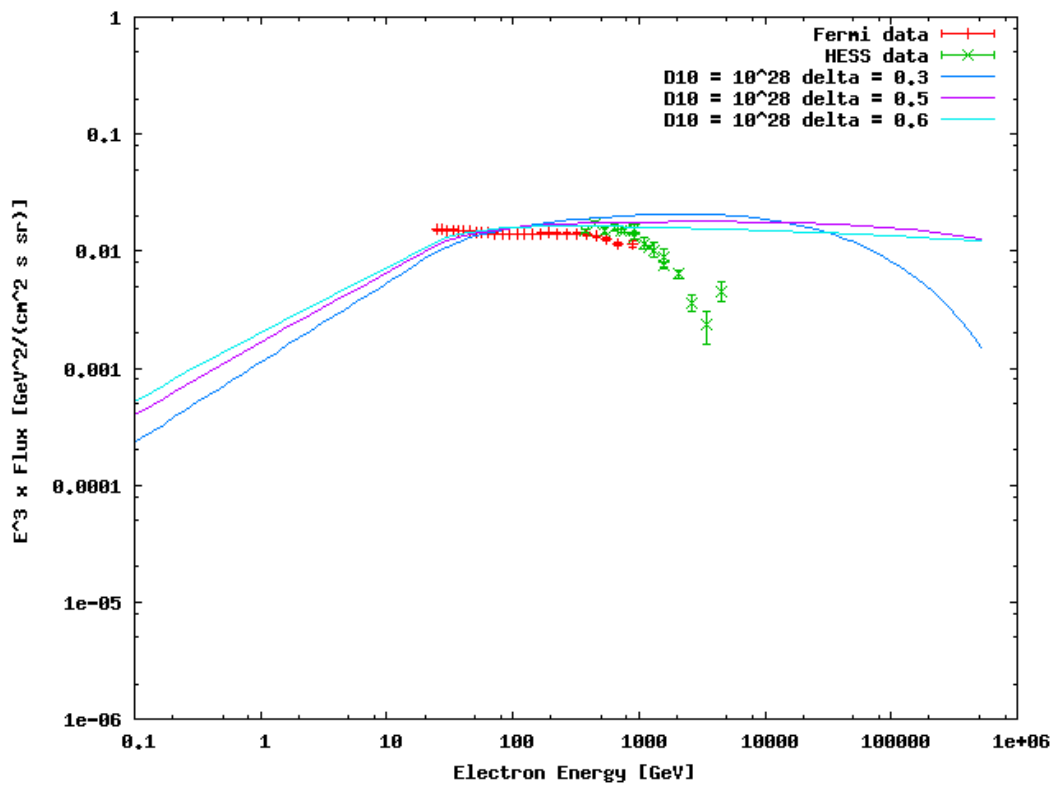

Figure 6.20: Calculated local electron flux spectrum for continuous injection with a constant rate and 3 different values of the diffusion power-law index $\delta = 0.3$, 0.5 and 0.6. $D_{10} = 10^{26}$ cm^2/s and $E_\star = 1$ GeV

Figure 6.21: Calculated local proton flux spectrum for continuous injection with a constant rate and 3 different values of the diffusion power-law index $\delta = 0.3$, 0.5 and 0.6. D_{10} $= 10^{28}$ cm^2/s and $E_\star = 1$ GeV

As in the case for the protons if $E_\star$ is increased to 10 GeV, the following Fig. (6.22) can be shown for burst-like injection and Fig. (6.23) for continuous injection with a constant rate.
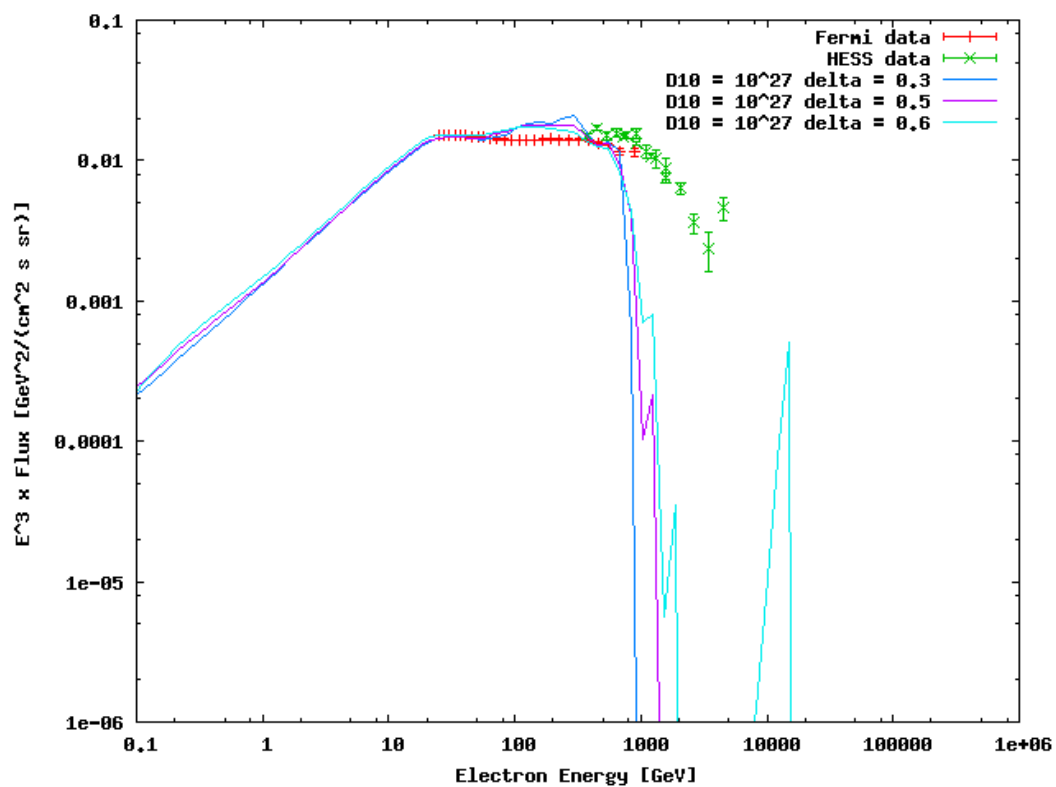

Figure 6.22: Calculated local electron flux spectrum for burst-like injection for 3 different values of the diffusion power-law index $\delta = 0.3$, 0.5 and 0.6. $D_{10} = 10^{27}$ cm^2/s and $E_\star = 10$ GeV
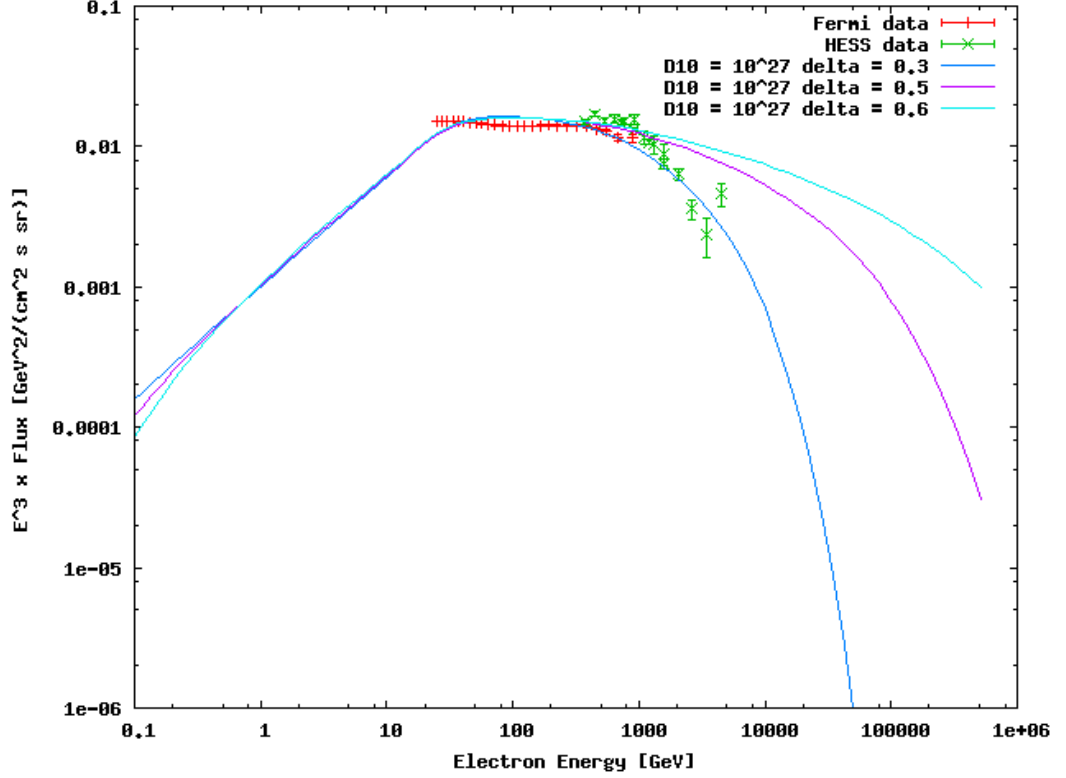
Figure 6.23: Calculated local electron flux spectrum for continuous injection with a constant rate for 3 different values of the diffusion power-law index $\delta = 0.3$, 0.5 and 0.6. $D_{10} = 10^{27}$ cm^2/s and $E_\star = 10$ GeV

As mentioned in the beginning of this subsection the electron flux strongly depends on the distribution of pulsars, which is displayed in Fig. (6.24) for burst-like injection. In contrast for continuous injection with a constant rate Fig. (6.25) the distribution of sources does not play a very important role. This is due to the assumption of continuous injection with a constant rate for the entire age of the pulsar, which for the bulk of them is between 10^6-10^7 years.
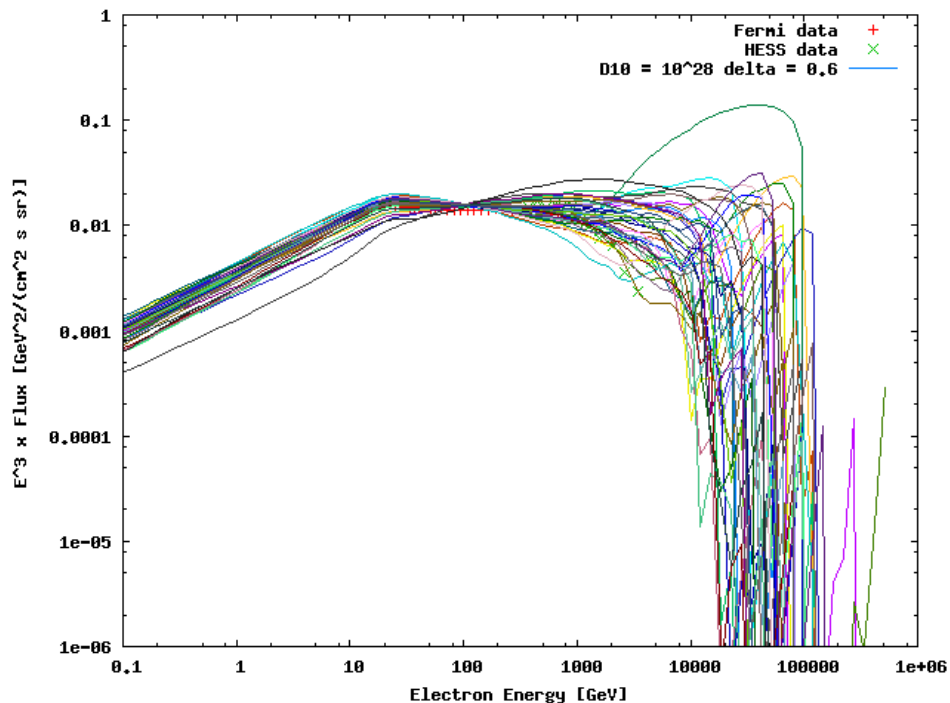
Figure 6.24: Calculated local electron flux spectrum for burst-like injection with a diffusion power-law index of $\delta = 0.6$. $D_{10} = 10^{28}$ cm^2/s and $E_{\star} = 1$ GeV, for 40 different realisations of the Galaxy
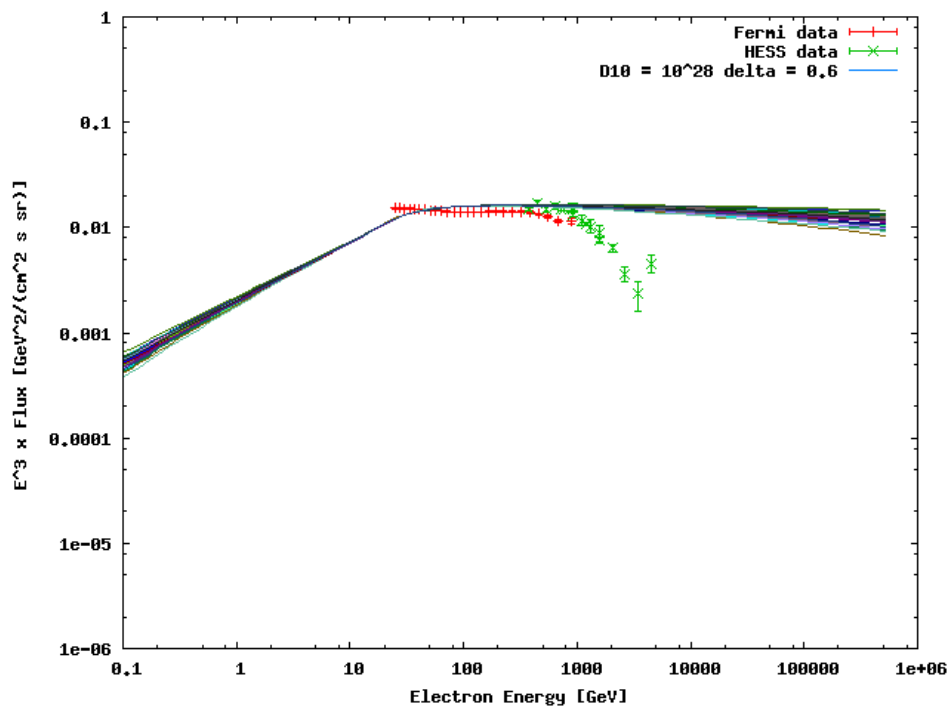

Figure 6.25: Calculated local electron flux spectrum for continuous injection with a diffusion power-law index of $\delta = 0.6$. $D_{10} = 10^{28}$ cm^2/s and $E_{\star} = 1$ GeV, for 40 different realisations of the Galaxy

Finally the resulting energy output of the SNRs and pulsars will be discussed. The injection mechanisms are assumed to be burst-like for the SNRs and the continuous with a constant rate for the pulsars. From Table 6.1 it can be seen that the energy output does not change dramatically for 40 different realisations of the Galaxy.

Table 6.1: Energy output for SNRs and pulsars $D_{10} = 10^{28}$ cm^2/s and $\delta = 0.6$

SNR	pulsar
$\sim$ 6.3-7.5 10^{51} erg	$\sim$ 4.8-5.7 10^{35} erg/s

It can be seen from an constant injection rate of $\sim 10^{35}$ erg/s over a timeframe of 10^7 years one gets a total energy output of $\sim 10^{49}$ erg. This value is in good agreement with the pulsar Geminga for example (Hooper et al. 2009(38)). Looking at the SNR an energy output $\sim 10^{51}$ erg is in agreement with the standard SNR energy output (Chevalier 1977(30)). Note that these values are obtained assuming that 30 % of the total energy output goes into accelerating protons and electrons respectively.

The conlusions from this chapter are:

- The proton flux spectrum at Earth can be qualitatively reproduced, by assuming a diffusion coefficient of $D_{10} = 10^{28}$ cm^2/s, a power-law diffusion coefficient of $\delta = 0.6$, E$_\star = 1$ GeV and a proton injection power-law index $\Gamma_p = 2.2$. The resulting spectral index is close to the measured one and the energy output is in good agreement with the standard total output of SNRs.

- The electron flux spectrum at Earth depends very much on the true distribution of sources and is therefore problematical to reproduce assuming a stochastic distribution of sources. That is why the same parameters for the electrons as for the protons are assumed, namely a diffusion coefficient of $D_{10} = 10^{28}$ cm^2/s, a power-law diffusion coefficient of $\delta = 0.6$, E$_\star = 1$ GeV and and a electron injection power-law index $\Gamma_e = 2.2$. Since the electron sources are assumed to be pulsars, the continuous injection mechanism is used, for which the energy output is also reasonable.

Chapter 7

Diffuse γ-ray emission from regions in the Galaxy

This chapter is dedicated to the diffuse γ-ray emission spectrum in different regions of the sky.

With the model described in chapter 6 it is now possible to calculate the emissivity $q_\gamma(E_\gamma, \vec{r})$ of CRs at any point $\vec{r}$ in the Galaxy. For inverse Compton scattering eq. (5.18), for Bremsstrahlung eq. (5.20) and for π^0 decay eq. (4.14) is used to calculate this emissivity.

The resulting γ-ray flux which is the number of photons per area, per time, per photon energy and per solid angle is then obtained by (see also eq. (4.16))

$$\phi_\gamma(E_\gamma) = \frac{dN_\gamma}{dAdE_\gamma dt d\Omega} = \int_0^{r_{\max}} \frac{q_\gamma(E_\gamma, \vec{r})}{4\pi} dr$$

where r is the line of sight distance which will be from now one referred to as D.

For the subsequent calculations the following parameters are used:

- The diffusion coefficient is chosen to be: $D_{10}=10^{28}$ cm^2/s and δ=0.6

- For SNRs burst-like injection is assumed with a proton injection power-law index $\Gamma_p = 2.2$ and for pulsars continuous injection with a constant rate is assumed with an electron injection power-law index $\Gamma_e = 2.2$

- The line of sight distance integral is performed up to $r_{\max} = 20$ kpc

- The resolution in longitude and latitude is assumed to be 0.5° and in line of sight distance D the resolution is 0.05 kpc.

- The region in the Galaxy is assumed to be $344° \leq l \leq 344.5°$ longitude and $0° \leq b \leq 0.5°$ as well as $4° \leq b \leq 4.5°$ latitude

These regions in the sky are chosen because the H_2 gas data from NANTEN is only available in a small region (see chapter 2) of the Galaxy. In general it is possible to generate the diffuse γ-ray emission spectrum for the whole Galaxy if the corresponding gas data is available, but because of the long computational time for a adequate resolution it is presented for this small section.

On the next few pages the proton and electron flux spectrum calculated for two different distances from the Earth, as well as the impact of different realisations of the Galaxy on the spectrum will be shown. It is interesting to see how the spectrum of protons and electrons changes in distance, depending on the latitude b. This is shown in Fig. (7.1) for the protons and Fig. (7.2) for the electrons. In both figures it can be seen that at $D_1 = 0.1$ kpc, which corresponds to $R_1 = 8.4$ kpc, the spectra overlay and at are at least for the electrons not distinguishable. This is plausible since the latitude angle has not much impact on the height above the Galactic plane for such a short line of sight distance D_1. However, for $D_2 = 8$ kpc the height z above the plane can be as large as ≈ 1.39 kpc and the spectra differ strongly from one another for the electrons and for the protons, at least in the lower energy part.
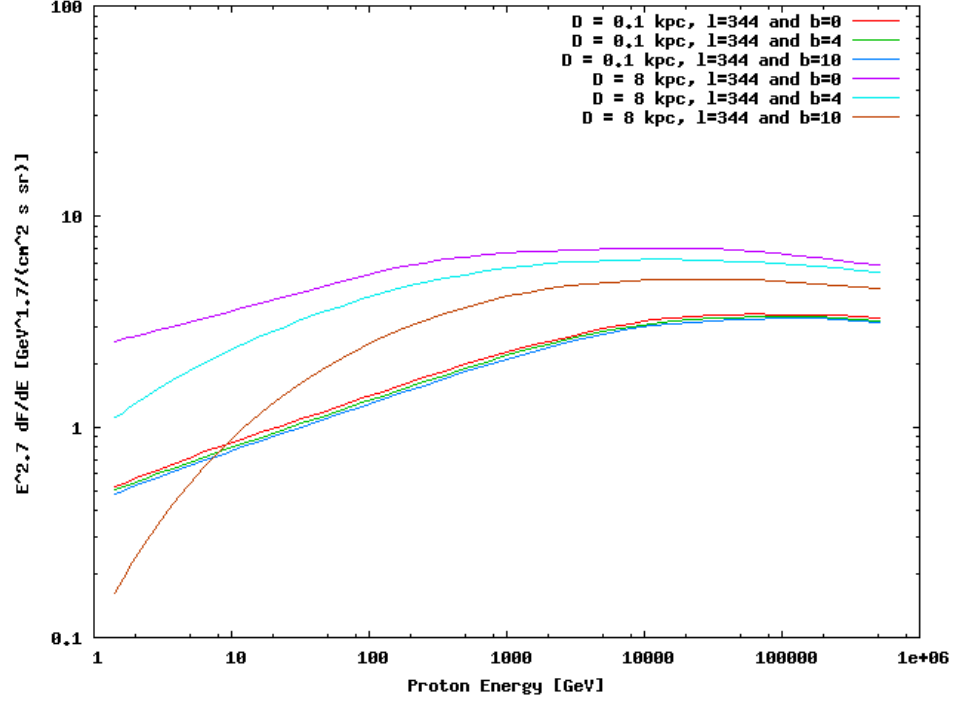
Figure 7.1: Proton spectrum for the region $344° \leq l \leq 344.5°$ in longitude, $0° \leq b \leq 0.5°$, $4° \leq b \leq 4.5°$ and $10° \leq b \leq 10.5°$ in latitude at 2 distances D_i from the Earth.
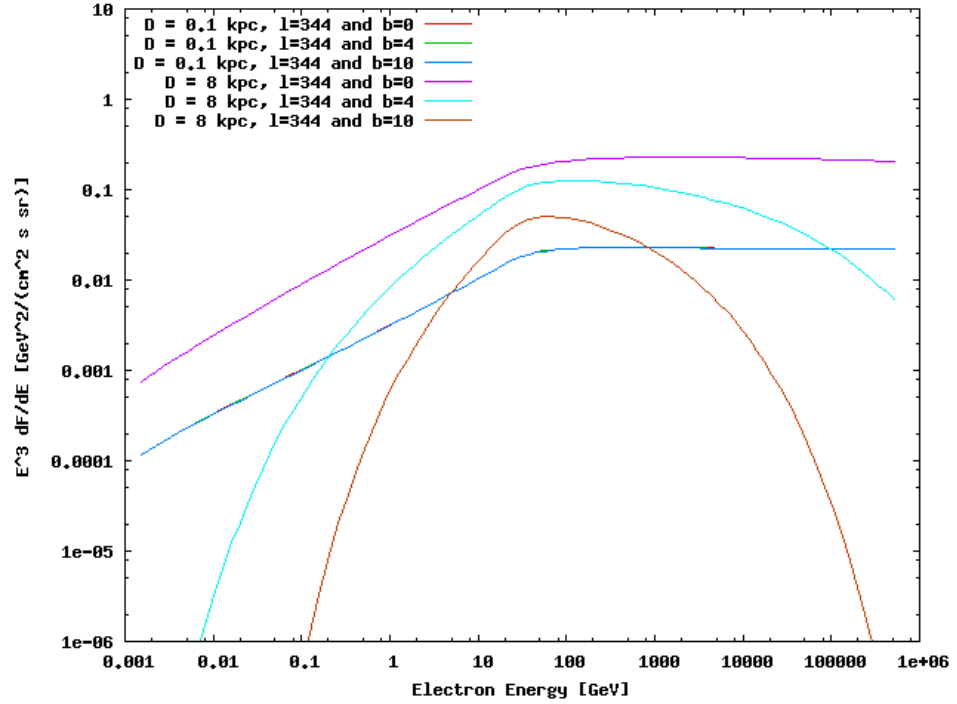

Figure 7.2: Electron spectrum for the region $344° \leq l \leq 344.5°$ longitude, $0° \leq b \leq 0.5°$, $4° \leq b \leq 4.5°$ and $10° \leq b \leq 10.5°$ latitude at 2 distances D_i from the Earth.

7. DIFFUSE γ-RAY EMISSION FROM REGIONS IN THE GALAXY

The next figures show how different realisations of the Galaxy change the electron and proton spectrum at one specific line of sight distance $D_2 = 8$ kpc for 2 different heights z (or latitude b) above the Galactic plane. Fig. (7.3) shows that for $344° \leq$ l $\leq 344.5°$, $0° \leq$ b $\leq 0.5°$ and $D_2 = 8$ kpc there are some slight bulges in the proton spectrum for different realisations of the Galaxy. This means that for those realisations a "younger" SNR was close to this observed point in space.
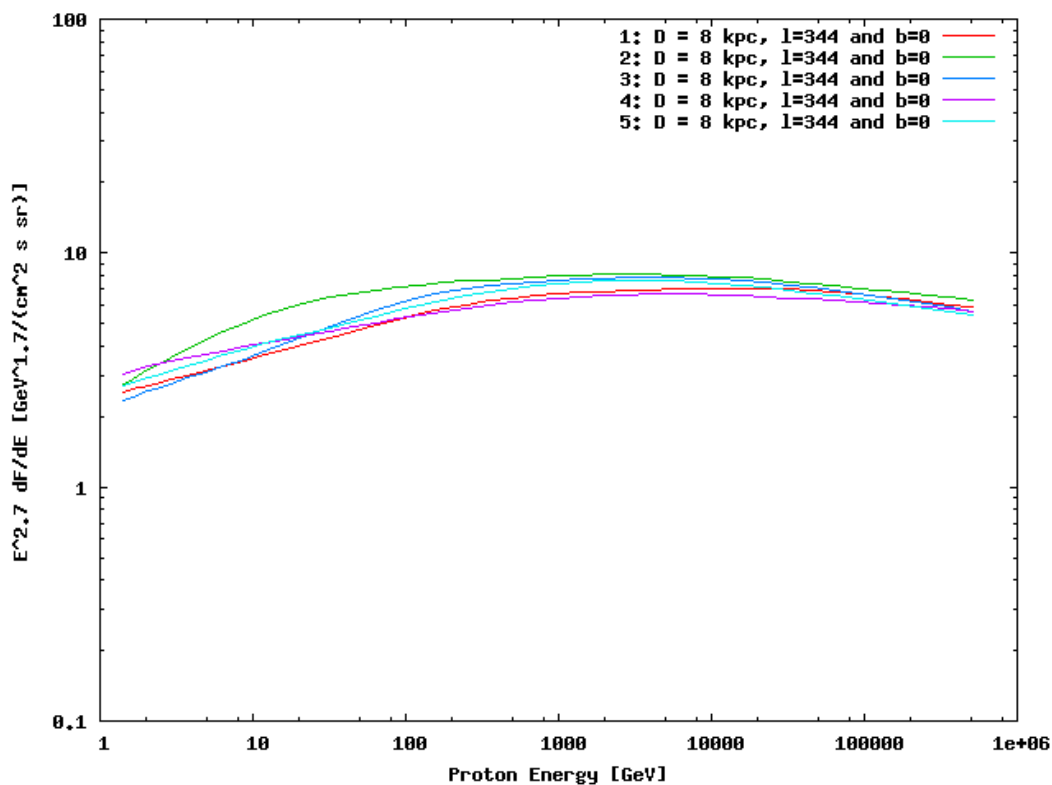

Figure 7.3: Proton spectrum for the region $344° \leq$ l $\leq 344.5°$ in longitude and $0° \leq$ b $\leq 0.5°$ in latitude at a distance $D_2 = 8$ kpc for 5 different realisations of the Galaxy

However, in Fig. (7.4) it can be seen that for $344° \leq l \leq 344.5°$, $10° \leq b \leq 10.5°$ and $D_2 = 8$ kpc the proton spectrum virtually looks the same for the 5 different realisations, which is also understandable since at this height $z_2 \approx 1.39$ kpc above the plane there is no close SNR anymore, since the distribution only goes up to about 0.2 kpc (see section 6.2.1).
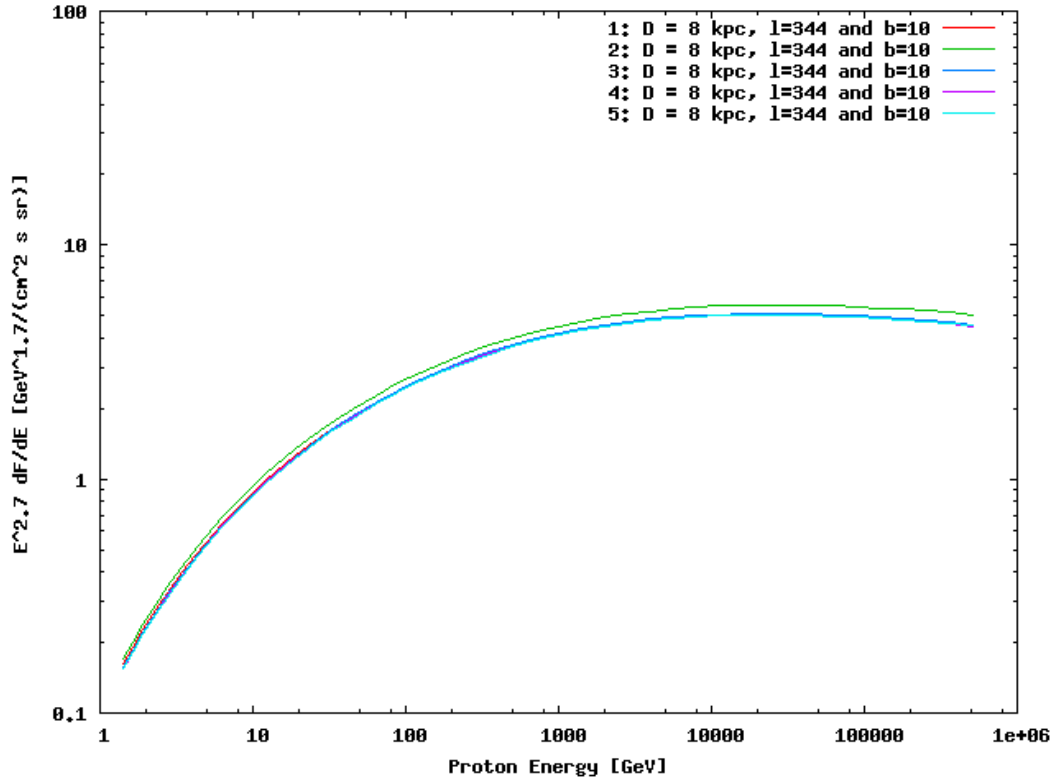

Figure 7.4: Proton spectrum for the region $344° \leq l \leq 344.5°$ in longitude and $10° \leq b \leq 10.5°$ in latitude at a distance $D_2 = 8$ kpc for 5 different realisations of the Galaxy

For the electrons that are continuously injected with a constant rate by pulsars, it can be seen in Fig. (7.5) and Fig. (7.6) that the spectrum hardly changes for the different realisations of the Galaxy, neither for $0° \leq b \leq 0.5°$ nor for $10° \leq b \leq 10.5°$.

Figure 7.5: Electron spectrum for the region $344° \leq l \leq 344.5°$ in longitude and $0° \leq b \leq 0.5°$ in latitude at a distance $D_2 = 8$ kpc for 5 different realisations of the Galaxy
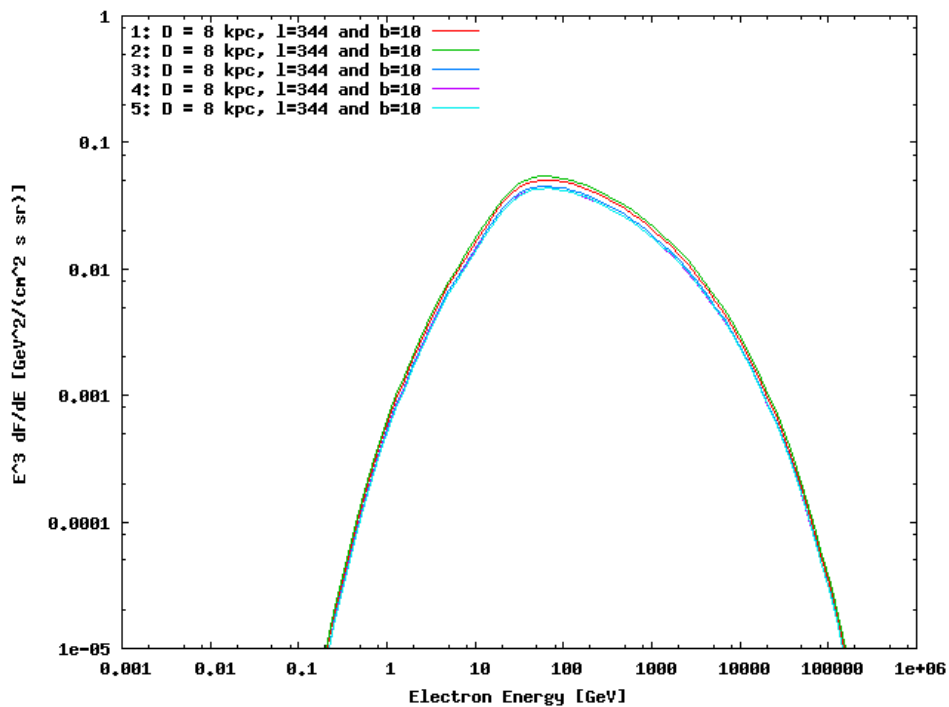
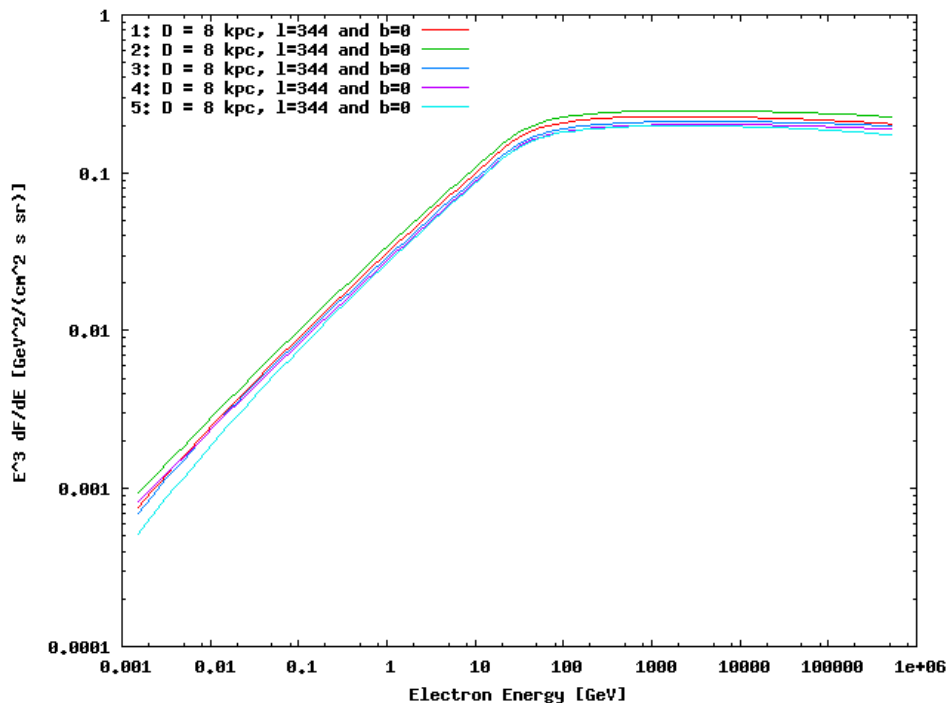**Figure 7.6:** Electron spectrum for the region $344° \leq l \leq 344.5°$ in longitude and $10° \leq b \leq 10.5°$ in latitude at a distance $D_2 = 8$ kpc for 5 different realisations of the Galaxy

The reason for the almost same spectra for 5 different realisations of the Galaxy, is the assumption of continuous injection with a constant rate for the entire age of the pulsar, which for the bulk of them is between 10^6-10^7 years. However, in the next Fig. (7.7) the electron spectrum for burst-like injection is shown for $344° \leq l \leq 344.5°$ in longitude and $0° \leq b \leq 0.5°$ at a distance $D_2 = 8$ kpc for 5 different realisations of the Galaxy. It can be seen that the electron spectrum indeed changes for different realisations of the Galaxy and the electron losses alter the spectrum at high energies, if the timeframe of injection is limited to a short window (δ-functional for burst-like injection). For a more realistic pulsar model one would need to account for the decrease in Spin-Down Luminosity and consequently acceleration power with time.

Figure 7.7: This plot shows the electron spectrum (for burst-like injection) for the region $344° \leq l \leq 344.5°$ in longitude and $0° \leq b \leq 0.5°$ in latitude at a distance $D_2 = 8$ kpc for 5 different realisations of the Galaxy
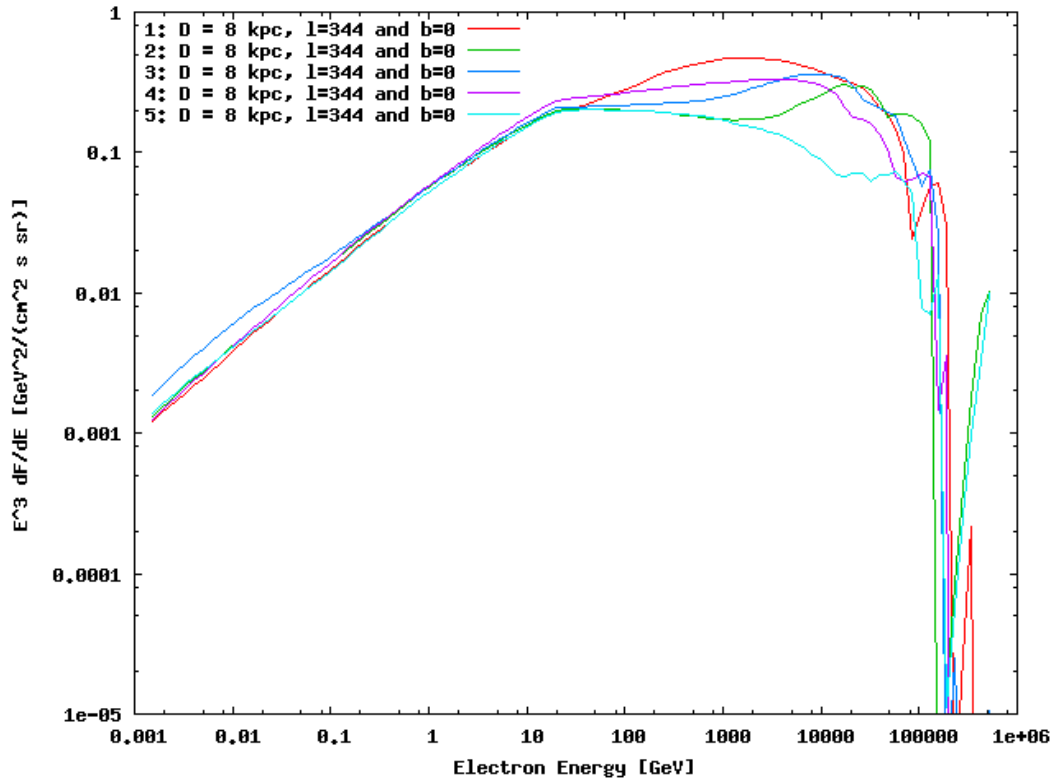
In the following the final result for the diffuse γ-ray emission spectrum for the different sections of the sky is shown and discussed.
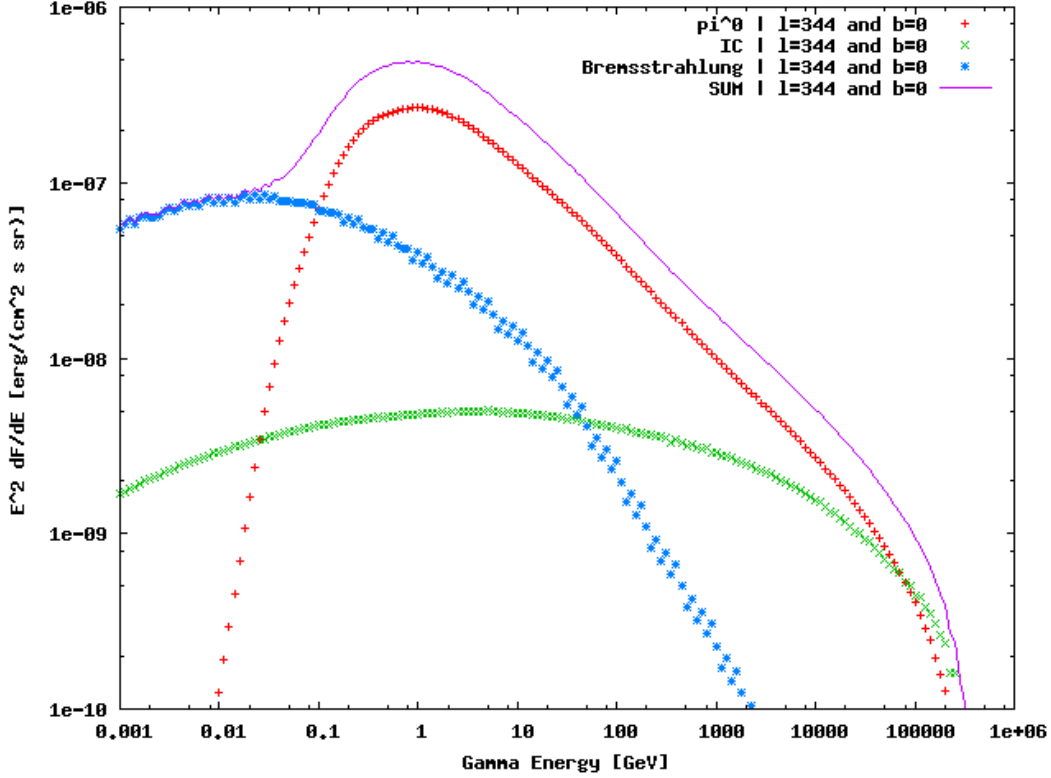
7.1 Region $344° \leq l \leq 344.5°$ and $0° \leq b \leq 0.5°$

Figure 7.8: Diffuse γ-ray emission spectrum for $344° \leq l \leq 344.5°$ and $0° \leq b \leq 0.5°$. Contribution from π^0, IC scattering and Bremsstrahlung is considered.

Fig. (7.8) shows that Bremsstrahlung dominates over IC scattering below about 100 GeV and over π^0 decay below roughly 0.05 GeV. Above roughly 0.1 GeV the entire spectrum is dominated by π^0 decay. However, it should be noted that the assumed radiation fields in section 3.3 are valid only for the vicinity of the solar system. Therefore the IC contribution is underestimated, especially near the Galactic center, where the radiation field energy density is higher by roughly one order of magnitude (see Porter & Strong (52)). For future improvements, a more realistic parameterization of the radiation fields could be used.

7.2 Region $344° \le l \le 344.5°$ and $4° \le b \le 4.5°$
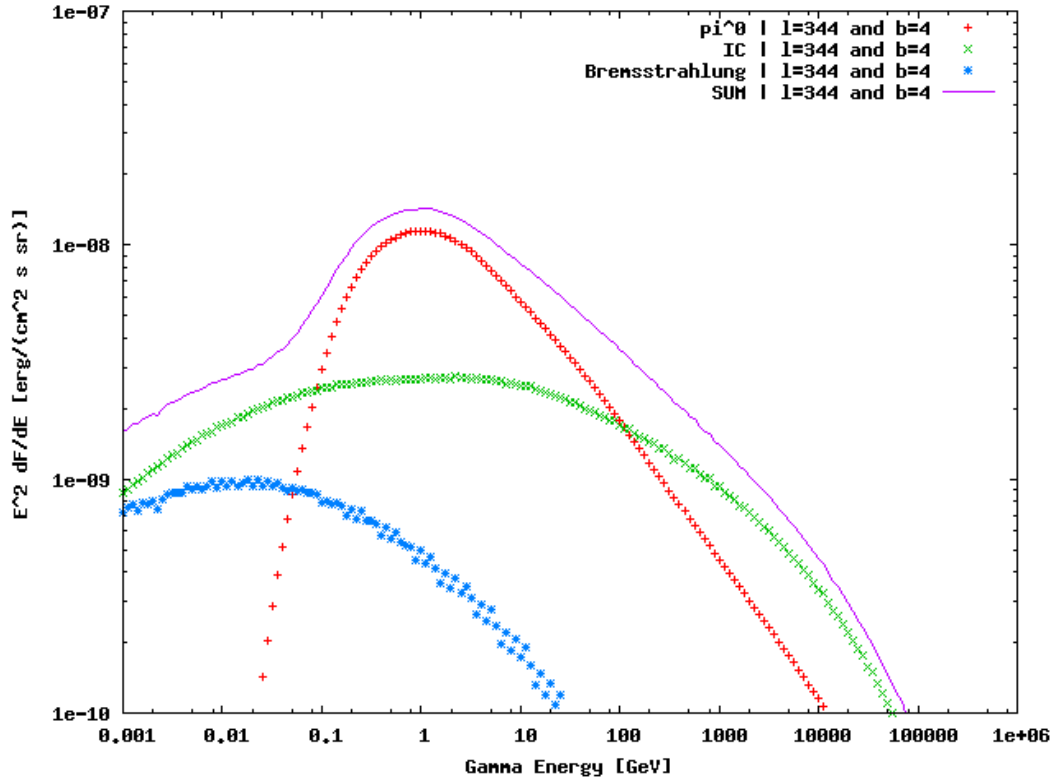
Figure 7.9: This figure shows the diffuse γ-ray emission spectrum for $344° \le l \le 344.5°$ and $4° \le b \le 4.5°$. Contribution from π^0, IC scattering and Bremsstrahlung is considered.

Looking at Fig. (7.9) one can observe that at higher latitudes Bremsstrahlung does not play a significant role in this case, since at these latitudes the gas density is lower than in the galactic plane (see section 3.2.1 Fig. (3.4)). The contribution from IC at above a few hundred GeV dominates over the π^0 contribution, also due to the lower gas density.

Finally it will be shown how the different realisations of the Galaxy change the calculated diffuse γ-ray emission spectrum. Fig. (7.10) illustrates the diffuse γ-ray emission spectrum for $344° \leq l \leq 344.5°$ and $0° \leq b \leq 0.5°$ for 5 different realisations of the Galaxy. There are virtually no differences in the spectrum, which means that the specific distribution might not play a signigicant role. Furthermore, the γ-ray emission spectrum is a line of sight integral over the photon-emissivity due to the three discussed interaction processes, and even if there are slight differences in this emissivity along the line of sight, they average out.

Figure 7.10: Diffuse γ-ray emission spectrum for $344° \leq l \leq 344.5°$ and $0° \leq b \leq 0.5°$ for 5 different realisations of the Galaxy. Contribution from π^0, IC scattering and Bremsstrahlung is considered.

However, assuming that pulsars inject electrons through the burst-like mechanism, the IC part of the diffuse γ-ray emission spectrum does indeed change with different realisations of the Galaxy, as seen in Fig. (7.11):
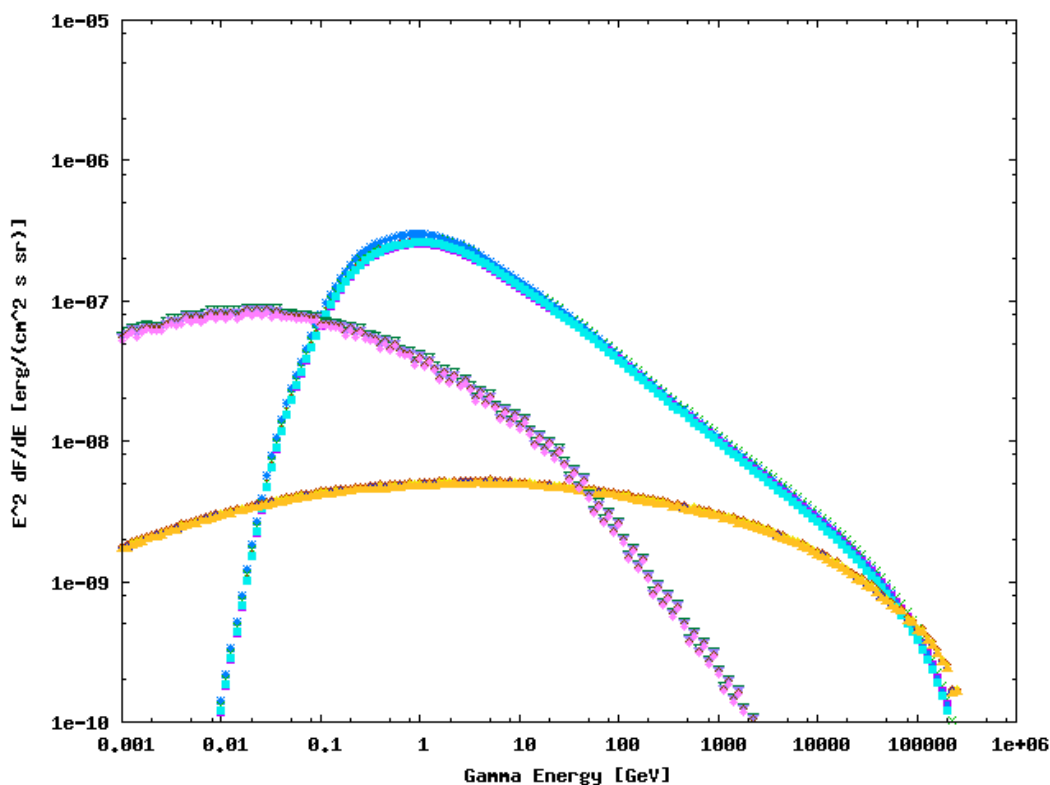

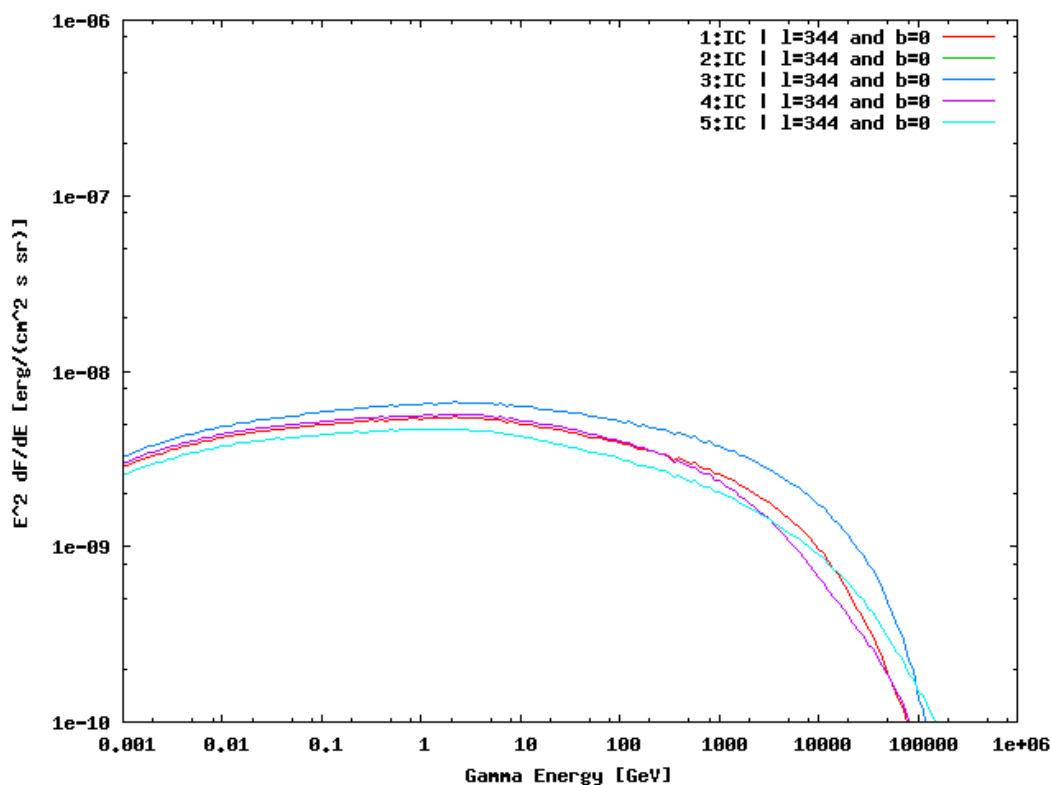**Figure 7.11:** Diffuse γ-ray emission spectrum for $344° \leq l \leq 344.5°$ and $0° \leq b \leq 0.5°$ for 5 different realisations of the Galaxy. Only contribution from IC scattering is considered and burst-like injection for the electrons is assumed.

Chapter 8

Conclusions & Outlook

8.1 Conclusions

With this model it is now possible to calculate the Galactic diffuse γ-ray emission spectrum and give flux estimates for different regions in the sky. The parameters for this model were assumed to be:

- Diffusion coefficient is a power-law in energy $D(E) = D_{10} \left(\frac{E}{E_\star} \right)^\delta$ with $\delta = 0.6$

- $D_{10} = 10^{28}$ cm^2/s and $E_\star = 1$ GeV

- Rate of supernova explosions $3 \cdot 10^{-2}$ yr^{-1}

- Birth-rate of pulsars $2 \cdot 10^{-2}$ yr^{-1}

- Burst-like injection for the SNRs and continuous injection with a constant rate for the pulsars.

- Proton and electron injection power-law index $\Gamma_p = \Gamma_e = 2.2$ ($\frac{dN}{dE} \propto E^{-\Gamma_{e/p}}$)

- Energy that goes into CR acceleration is 30% of the total energy output of SNRs and pulsars.

With these parameters the local proton and electron flux can qualitatively be reproduced, see Fig.(6.10) and Fig. (6.21) in chapter 6, respectively. Although for the high energy part of the electron spectrum, assuming a continuous injection with a constant rate from pulsars, the agreement with the data is not that good. This is because for pulsars continuous injection with a constant rate is assumed, however for a more realistic

pulsar model one would need to account for the decrease in Spin-Down Luminosity and consequently acceleration power with time. The assumption of burst-like injection for pulsars can only be considered reasonable if the pulsar is relatively old compared to the typical timescale of injection. For protons escaping the SNR, the burst-like injection using the SNR model is the more realistic characterization compared with the other two (being burst-like and continuous injection). However, the solution eq. (5.8) for the SNR model obtained by Gabici, Aharonian & Casanova 2009(35) is valid for an proton injection power-law index of 2 and does not seem to be able to reproduce the needed spectral index of about 2.7 at the position of the Earth (see Fig. (6.10)), with reasonable parameters D_{10} and δ for the diffusion. Although the exact injection mechanism for protons might not be as important if there is no nearby source, since on such large timescales $\sim 10^7$ years protons, because of their low energy losses, had enough time to isotropize within the Galaxy. However, this is not the case for continuous injection with a constant rate, since in this scenario always new protons additionally escape the SNR.

The different realisations of the Galaxy only plays a minor role for the protons because of isotropization, at least if there is no SNR close to the observed point. For the electrons as seen in Fig. (6.25) one could argue similarly, but it should be mentioned that for a lower diffusion coefficent D_{10} and lower diffusion power-law index δ the different realisations of the Galaxy have a stronger impact on the lower and higher energy part of the spectrum compared to the case of $\delta = 0.6$. and $D_{10} = 10^{28}$ cm^2/s.

The calculation of the energy output of SNRs and luminosity of pulsars, resulted in $E_{SNR} \approx 10^{51}$ erg for the SNRs and $E_{pulsar} \approx 10^{35}$ erg/s for the pulsars. Both values seem reasonable, the energy output for the SNR is in agreement with the standard energy output (see Gabici, Aharonian & Casanova 2009(35)). Although the typical luminosity of a pulsar is $\sim 10^{37}$ erg/s, the obtained lower value of $\sim 10^{35}$ erg/s can be understood considering the fact that the timeframe of continuous injection is about 10^7 years for the bulk of the pulsars. This yields a total energy output of $\sim 10^{49}$ erg in agreement with the pulsar Geminga for example (Hooper et al. 2009(38)). It should be noted that these values were obtained assuming that 30 % of it goes in to accelerating protons and electrons respectively.

The obtained diffuse γ-ray emission spectra yield predictions for the region $344° \leq l \leq 344.5°$ and $0° \leq b \leq 0.5°$ as well as for the region $344° \leq l \leq 344.5°$ and $4° \leq b \leq 4.5°$. Overall the spectrum for both regions look reasonable when compared with one another. However, further discussions on the validity of the predictions must include the comparison with measurements.

8.2 Outlook

To refine the model and yield more accurate predictions of the spectrum of diffuse gamma-ray emission, future work could include the following:

- Analyze FERMI data of the diffuse γ-ray emission and compare it with the model predictions.

- Model the injection mechanism for pulsars in a more realistic way. This could be achieved by implementing a continuous injection mechanism with a rate that decreases rather than remaining constant with the time since the injection of particles started.

- Obtain an analytical solution for the SNR model that yields an initial proton power-law index of 2.2, if there exists one.

- Use a parameterization of the radiation fields depending on the location in the Galaxy, rather than using the local values in a homogenous approach.

- Implement the spiral arm structure of the Galaxy.

- Solve the diffusion equation numerically so that for instance more energy losses can be considered, which could be especially important in dense regions of the Galaxy. Although the increased computational time could very well get too high, rendering this approach unuseful.

References

[1] Abdo, A. A. et al., 2008. A measurement of the spatial distribution of diffuse tev gamma-ray emission from the galactic plane with milagro. *ApJ Vol. 688, pp. 1078-1083.* 3, 24

[2] Abdo, A. A. et al., 2009. Fermi lat observation of diffuse gamma rays produced through interactions between local interstellar matter and high-energy cosmic rays. *ApJ Vol. 703, pp. 1249-1256.* 23

[3] Abdo, A. A. et al., 2009. Measurement of the cosmic ray e^++e^- spectrum from 20gev to 1tev with the fermi large area telescope. *PhRvL, Vol. 102.* 8

[4] Acero, F. et al., 2010. First detection of vhe γ-rays from sn 1006 by hess. *A&A, Vol. 516.* 9

[5] Adriani, O. et al., 2009. New measurement of the antiproton-to-proton flux ratio up to 100 gev in the cosmic radiation. *Phys. Rev. Lett. 102.* 9

[6] Aharonian, F. and Atoyan, A. M., 1996. On the emissivity of π^0-decay gamma radiation in the vicinity of accelerators of galactic cosmic rays. *A&A, Vol. 309, pp. 917-928.* 35, 38, 51

[7] Aharonian, F. and Atoyan, A. M., 2000. Broad-band diffuse gamma ray emission of the galactic disk. *A&A, Vol. 362, pp. 937-952.* 30

[8] Aharonian, F. et al., 2002. Limits on the tev flux of diffuse gamma rays as measured with the hegra air shower array. *APh, Vol. 17, p. 459-475.* 3

[9] Aharonian, F. et al., 2004. High-energy particle acceleration in the shell of a supernova remnant. *Nature, Vol. 432, pp. 75-77.* 9

REFERENCES

[10] Aharonian, F. et al., 2005. Detection of tev γ-ray emission from the shell-type supernova remnant rx j0852.0-4622 with hess. *A&A, Vol. 437, pp.L7-L10.* 9

[11] Aharonian, F. et al., 2005. A new population of very high energy gamma-ray sources in the milky way. *Science, Vol. 307, pp. 1938-1942.* 3

[12] Aharonian, F. et al., 2006. Observations of the crab nebula with hess. *A&A, Vol. 457, pp.899-915.* 8

[13] Aharonian, F. et al., 2007. Primary particle acceleration above 100 tev in the shell-type supernova remnant rx j1713.7-3946 with deep hess observations. *A&A, Vol. 464, pp.235-243.* 9

[14] Aharonian, F. et al., 2008. Discovery of very high energy gamma-ray emission coincident with molecular clouds in the w 28 (g6.4-0.1) field. *A&A, Vol. 481, pp.401-410.* 24

[15] Aharonian, F. et al., 2009. Probing the atic peak in the cosmic-ray electron spectrum with h.e.s.s. *A&A, Vol. 508, pp. 561-564.* 8

[16] Albert, J. et al., 2008. Vhe γ-ray observation of the crab nebula and its pulsar with the magic telescope. *ApJ, Vol 674, pp. 1037-1055.* 8

[17] Alexandra, N. C. et al., 1999. The distance to the vela supernova remnant. *ApJ., Vol. 515, pp. L25-L28.* 63

[18] Atoyan, A. M. and Aharonian, F., 1995. Electrons and positrons in the galactic cosmic rays. *PhRvD, Vol. 52, pp.3265-3275.* 38, 39, 43

[19] Berezinsky, V. S., 1990. Astrophysics of cosmic rays. *Amsterdam: North-Holland, 1990, edited by Ginzburg, V.L.* 10

[20] Bertsch, D. L. et al., 1993. Diffuse gamma-ray emission in the galactic plane from cosmic-ray, matter, and photon interactions. *ApJ., Vol. 416, p.587.* 23

[21] Bethe, H. A. and Heitler, W., 1934. *Proc. R. Soc. London A146, 83.* 25

[22] Binney, J. and Merrifield, M., 1998. Galactic astronomy. *Princeton, NJ : Princeton University Press.* 12, 13

[23] Blandford, R. and Eichler, D., 1987. Particle acceleration at astrophysical shocks: A theory of cosmic ray origin. *Phys. Rep. 154 (1987)*. 8

[24] Blumenthal, G. and Gould, R., 1970. Bremsstrahlung, synchrotron radiation, and compton scattering of high-energy electrons traversing dilute gases. *RvMP., Vol. 42, pp. 237-271*. 25, 26

[25] Borione, A. et al., 1998. Constraints on gamma-ray emission from the galactic plane at 300 tev. *ApJ., Vol. 493*. 3

[26] Caliandro, G. A. et al., 2010. Fermi large area telescope first source catalog. *ApJ 188*. 60

[27] Casanova, S. and Dingus, B. L., 2008. Constraints on the tev source population and its contribution to the galactic diffuse tev emission. *APh, Vol 29, p. 63-69*. 24

[28] Casanova, S. et al., 2010. Molecular clouds as cosmic-ray barometers. *PASJ, Vol. 62*. 14

[29] Case, G. and Bhattacharya, D., 1998. A new sigma-d relation and its application to the galactic supernova remnant distribution. *ApJ., Vol. 504, p.761*. 56

[30] Chevalier, R. A., 1977. The interaction of supernovae with the interstellar medium. *Annu. Rev. A&A., Vol. 15*. 79

[31] Dame, T., 2001. The milky way in molecular clouds: A new complete co survey. *ApJ, Vol. 547, 792*. 17

[32] Drury, L. O. and Voelk, H., 1994. Cosmic ray hydrodynamics at shock fronts. *A&A vol. 291*. 8

[33] Evoli, C. et al., 2010. Unified interpretation of cosmic-ray nuclei and antiproton recent measurements. *eprint arXiv:0909.4548*. 66

[34] Ferriere, K. M., 2001. The interstellar environment of our galaxy. *RvMP., Vol. 73, pp. 1031-1066*. 56

REFERENCES

[35] Gabici, S. et al., 2009. Broad-band non-thermal emission from molecular clouds illuminated by cosmic rays from nearby supernova remnants. *MNRAS, Vol. 396, pp. 1629-1639.* 40, 52, 94

[36] Ginzburg, L. and Syrovatskii, S., 1964. Origin of cosmic rays. *Pergamon Press, London.* 8

[37] Hofmann, W. et al., 1999. Tev gamma-ray observations of the crab and mkn 501 during moonshine and twilight. *APh, Vol. 12, p. 65-74.* 8

[38] Hooper, D. et al., 2005. Pulsars as the sources of high energy cosmic ray positrons. *JCAP, Issue 01, pp. 025.* 79, 94

[39] Hooper, D. et al., 2008. An excess of cosmic ray electrons at energies of 300-800gev. *Nature, Vol. 456, pp. 362-365.* 8

[40] Kalberla, P., 2005. The leiden/argentine/bonn (lab) survey of galactic hi. *A&A, Vol. 440, 775.* 14, 15, 16

[41] Kamae, T. et al., 2005. Diffractive interaction and scaling violation in pp$\rightarrow \pi^0$ interaction and gev excess in galactic diffuse gamma-ray spectrum of egret. *ApJ., Vol. 620, pp. 244-256.* 31, 33

[42] Kamae, T. et al., 2006. Parameterization of gamma, $e^{+/-}$ and neutrino spectra produced by p-p interaction in astronomical environment. *ApJ., Vol. 647, pp. 692-708.* 31, 32, 34, 35

[43] Karlsson, N. and Kamae, T., 2008. Parameterization of the angular distribution of gamma rays produced by p-p interaction in astronomical environment. *ApJ., Vol. 674, pp. 278-285.* 31

[44] Lorimer, D. et al., 2006. The parkes multibeam pulsar survey - vi. discovery and timing of 142 pulsars and a galactic population analysis. *MNRAS 372.* 60

[45] Moiseev, A. A. et al., 2009. On possible interpretations of the high energy electron-positron spectrum measured by the fermi large area telescope. *APh, Vol 32, p. 140-151.* 7

[46] Nakanishi, H. and Sofue, Y., 2003. Three-dimensional distribution of the ism in the milky way galaxy: I. the h i disk. *PASJ, Vol. 55.* 14

[47] Nakanishi, H. and Sofue, Y., 2006. Three-dimensional distribution of the ism in the milky way galaxy: Ii. the molecular gas disk. *PASJ, Vol. 58.* 14

[48] Pohl, M. et al., 2005. Cosmic-ray propagation properties for an origin in supernova remnants. *AIP Conf. Proc. 801, pp. 86-87.* 56

[49] Protheroe, R. J., 1996. Origin and propagation of the highest energy cosmic rays. *eprint arXiv:astro-ph/9612212.* 42

[50] Ptuskin, V. et al., 2005. On the spectrum of high-energy cosmic rays produced by supernova remnants in the presence of strong cosmic-ray streaming instability and wave dissipation. *A&A, Vol. 429, pp. 755-765.* 40

[51] Schlickeiser, R., 2002. Cosmic ray astrophysics. *Berlin: Springer.* 21, 46

[52] Strong, A. W. and Porter, T., 2005. A new estimate of the galactic interstellar radiation field between 0.1um and 1000um. *Proc. 29th Int. Cosmic Ray Conf., Vol. 4, p.77.* 88

[53] Strong, A. W. et al., 2000. Diffuse continuum gamma rays from the galaxy. *ApJ Vol. 537, Issue 2, pp. 763-784.* 53

[54] Strong, A. W. et al., 2003. Evaluation of models for diffuse continuum gamma rays in egret range. *Proc. 28th Int. Cosmic Ray Conf., p.2687.* 54

[55] Strong, A. W. et al., 2004. Diffuse galactic continuum gamma rays: A model compatible with egret data and cosmic-ray measurements. *ApJ Vol. 613, Issue 2, pp. 962-976.* 23, 24

[56] Strong, A. W. et al., 2007. Cosmic-ray propagation and interactions in the galaxy. *Ann. Rev. Nucl. Part. Sci. 57, 285.* 9

[57] Svensmark, H., 2007. Cosmoclimatology: a new theory emerges. *Astronomy & Geophysics: Volume 48 Issue 1, Pages 1.18 - 1.24.* 5

[58] Tauris, T. M. et al., 1994. Discovery of psr j0108-1431: The closest known neutron star? *ApJ., Vol. 428, p. L53-L55.* 63

Danksagung

An dieser Stelle möchte ich mich bei allen bedanken, die auf unterschiedlichster Art und Weise zum Gelingen dieser Arbeit beigetragen haben. Mein besonderer Dank gilt:

- vor allem Sabrina Casanova, für die viele Zeit die Du dir genommen hast um mich zu betreuen und dass ich jederzeit zu Dir kommen konnte wenn ich Fragen hatte. Ebenso danke ich Dir für die ganze Zeit die Du dir genommen hast um diese Arbeit zu korrigieren.

- Professor Werner Hofmann, für die Möglichkeit eine besonders interessante Diplomarbeit durchführen zu dürfen.

- Professor Karl-Tasso Knöpfle für die Übernahme der Zweitkorrektur.

- Joachim Hahn für das Korrekturlesen der kompletten Arbeit!

- Daniil Nekrassov, Stefan Ohm, Dirk Lennarz und Henning Gast für die hilfreichen Tipps und Kommentare beim Korrekturlesen.

- All den anderen Mitgliedern der H.E.S.S. Gruppe für eine schöne Zeit und eine angenehme Arbeitsatmosphäre.

Schliesslich möchte ich meinen Eltern, Frank und Irmgard sowie meinem Bruder Matthias danken, für die Unterstützung und die Geduld in all meinen Unternehmungen und Lebensphasen. Insbesondere möchte ich mich bei Euch bedanken, dass Ihr mir immer zur Seite standet, denn ohne euch wäre ich bestimmt nicht bis hierher gekommen.

Erklärung

Ich versichere, dass ich diese Arbeit selbständig verfasst und keine anderen als die angegebenen Quellen und Hilfsmittel benutzt habe.

Heidelberg, den _____   _____

(Unterschrift)